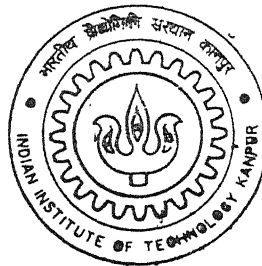


# PHYSICAL AND MATHEMATICAL MODELING OF VELOCITY FIELD DISTRIBUTION IN A SIMULATED HALL-HEROULT CELL

By

**SURYA NARAYAN LENKA**



**DEPARTMENT OF MATERIALS AND METALLURGICAL ENGINEERING**

**Indian Institute of Technology Kanpur**

**APRIL, 2002**

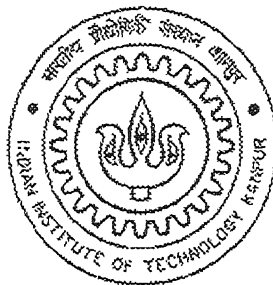
# **PHYSICAL AND MATHEMATICAL MODELING OF VELOCITY FIELD DISTRIBUTION IN A SIMULATED HALL-HEROULT CELL**

*A Thesis work submitted  
in partial fulfillment of the requirements for the degree of*

**MASTER OF TECHNOLOGY**

*By*

**SURYA NARAYAN LENKA**



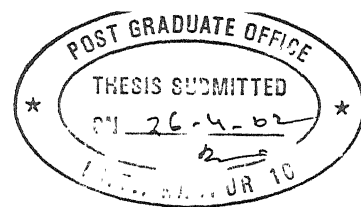
**Department of Materials and Metallurgical Engineering  
INDIAN INSTITUTE OF TECHNOLOGY, KANPUR.**

**April, 2002**

4 FEB 2002 / MME  
पुरुषोत्तम काशीनाथ केनकर पुस्तकालय  
भारतीय प्रौद्योगिकी संस्थान कानपुर  
अवधि क्र० A 141905



A141905



## CERTIFICATE

This is to certify that the present work "Physical and Mathematical Modeling of Velocity field distribution in a Simulated Hall-Heroult cell" has been carried out by Mr. Surya Narayan Lenka (Roll No-Y010650) towards his M.Tech., dissertation under our supervision and that this has not been submitted elsewhere for a degree.

(Dr. S. P. Mehrotra)

Professor

Department of materials and metallurgical engineering  
Indian Institute of Technology, Kanpur.

(Dr. Rajiv Shekhar)

Professor

Department of materials and metallurgical engineering  
Indian Institute of Technology, Kanpur.

Dated: April 2002.



## ACKNOWLEDGEMENTS

I would like to take this opportunity to express my heartfelt gratitude to my advisors, Prof. S P. Mehrotra and Prof. R. Shekhar for their expert guidance and continuous encouragement through out the course of this work. Their guidance, intellectual support and creative criticism lead me to generate my own ideas. I offer my most humble and profound indebtedness to them for their deep concern both in the area of academics and personnel front.

The selfless dedication of a number of individuals made me successful in completing the work. I am thankful to Mr. Sharma for helping out in materializing the design of the calibration set up. I express my heartfelt thanks to Mr. K. Sanjay, who has been made significant contribution in giving ideas in eliminating the various difficulties during designing of the various apparatus. I am thankful to Mr. Mohan for his help in sorting out the problems related to probes and Keithley 182 sensitive digital voltmeter. My special thanks to Mr. G. P. Bajpai, who helped me many times beyond office hours also. I thank Mr. Kartikeyan who helped me out in making the interfacing of the computer ready for data acquisition. Many thanks to my friends vikas, shiba, trailokya, Sunil, Suraj, and Ranjan to name a few who made my life enjoyable at IIT, Kanpur. I thank Preetiprakash for his help during carrying out of experiments. I thank the entire Metallurgy and Materials engineering department for their cooperation. I wish to thank my family members who have been giving their love and affection.

Finally I thank anyone and everyone who has knowingly or unknowingly helped me with this project and in general, life at I I T, Kanpur.

Surya Narayan Lenka

Date: 29<sup>th</sup> April 2002.

# TABLE OF CONTENTS

	PAGE
ABSTRACT	vi
List of Figures	vii
List of Tables	x
List of symbols	xi
<b>CHAPTER 1 INTRODUCTION</b>	
1.1 Introduction	1
1.2 Process performance of Hall-Heroult cell	2
1.3 Role of magnetohydrodynamics in Hall-Heroult cell	5
<b>CHAPTER 2 LITERATURE SURVEY</b>	
2.1 Brief review of the previous investigation	7
2.2 Factors affecting hydrodynamics in hall cell	13
2.3 Scope/objective of the present investigation	19
<b>CHAPTER 3 EXPERIMENTAL STUDIES</b>	
3.1 Experimental Set-up	22
3.1.1 Components of the Experimental Assembly.	22
3.1.2 Accessories to the cell	25
3.2 Calibration of velocity probe	28
3.2.1 Principle of velocity probe	28
3.2.2 Design of velocity probe	28
3.2.3 Design of calibration set up	28
3.2.4 Calibration of velocity probe	30
3.3 Experimental procedure	34
3.3.1 Start up	34
3.3.2 Measures for stable reading	37
3.3.3 Reproducibility experiments	37
3.3.4 Velocity measurements	40
<b>CHAPTER 4 RESULTS AND DISCUSSION</b>	
4.1 Measured velocity distribution within the cell	42

4.1.1 Base Case	42
4.1.1.1 Effect of depth of measurement	50
4.1.2 Effect of total input current	50
4.1.3 Effect of Anode Cathode Distance (ACD)	54
4.1.4 Effect of ledge	54
4.2 Sensitivity Experiments	58
<b>CHAPTER 5 MATHEMATICAL MODELING</b>	
5.1 Formulation of mathematical model	60
5.2 The algorithm.	63
5.3 Prediction of velocity field distribution and comparison with experimental results	64
5.3.1 Effect of total input current	65
5.3.2 Effect of anode cathode distance	65
5.3.3 Effect of ledge	75
5.4 Sensitivity study	75
<b>CHAPTER 6 SUMMARY AND CONCLUDING REMARKS</b>	78
<b>CHAPTER 7 SUGGESTIONS FOR FUTURE WORK</b>	80
<b>APPENDIX</b>	81
<b>REFERENCES</b>	89

## ABSTRACT

Hall-Heroult (Hall) cell is the only process commercially practiced for extraction of Aluminum. The principle involved here is the electrolytic decomposition of alumina to aluminum. Large magnetic fields are produced due to the large current flowing through the cell, bus bars as well as in the neighbouring cells. This magnetic field on interacting with the current gives rise to large electromagnetic forces and torques which are the origin of magnetohydrodynamics phenomena. This provides motion to the conducting melt especially aluminium pad present at the bottom. This fluid motion leads to the formation of waves at the metal-electrolyte interface. Waves developed in the aluminium pad, which apart from resulting the momentary short-circuiting to the anode, produce erosion of the carbon lining of the cell. Short-circuiting phenomena significantly reduce energy efficiency of the cell.

Worldwide the research on aluminium is focused on the design of Hall cells with reduced energy consumption. This investigation is a continuation of the ongoing research in our laboratory on measurement of magnetohydrodynamics in simulated Hall cell sponsored by Department of Science and Technology. Previous investigations in project have dealt with mathematical modeling and experimental measurements of current distribution and magnetic field. Hence, this study essentially focuses on velocity distribution.

Mathematical modeling has played a significant role in design and development of modern cells. But before these models can reliably be used to predict the process performance of an industrial cell, they need to be tuned. Keeping the difficulty of conducting measurements of magnetic field and liquid velocity in industrial Hall cells a simulated Hall-Heroult cell has been set up which contains one layer of molten Wood's metal at the top of the solidified aluminium layer. In this cell Wood's metal simulates the electrolyte while the aluminium layer represents the aluminium pad in the Hall cells. A mathematical model has been formulated to predict the velocity distribution within the cell. Model equations have been solved using commercially available software package 'PHOENICS'. The model has been validated by comparing the model predictions with those experimentally obtained using the simulated cell.

Consequently Wood's metal (melting point  $\sim 75^{\circ}\text{C}$ ) based laboratory cells have been used to: (a) generate velocity distribution data for validating the mathematical models, and (b) study the effect of operating parameters such as current density, anode-cathode distance (ACD) etc on velocity field. It was realized that there were a few shortcomings in our earlier measurements. Hence, an attempt has been made to make the measurements more reliable by taking the measurements through Data Acquisition Systems. The velocity measurements have been made first time in a double-layered simulated Hall- Heroult cell.

# LIST OF FIGURES

		Page No.
Figure 1.1	Cross sectional view of typical industrial Hall-Heroult cell	3
Figure 1.2	Current efficiency Vs anode cathode distance (ACD).	4
Fig. 2.1	Current densities with in a half section of the cell for a quarter riser design	8
Fig. 2.2	Current distributions within the cell containing aluminium pad at the cell bottom with end riser design.	9
Fig. 2.3	Measured velocity vectors on Physical model with its fourteen anode configuration with end riser design.	11
Fig. 2.4	Measured velocity field distribution in a single layered simulated cell with end riser design.	11
Fig. 2.5	Calculated and measured velocities within the molten aluminium of the 185 kA cell.	12
Fig. 2.6(a)	Flow pattern in a cell at different ages.	14
Fig. 2.6(b)	Freeze profiles (i) <150 days, and (ii) >900 days.	15
Fig. 2.7	Schematic diagram of (i) End riser, (ii) Quarter riser, and (iii) Novel riser design.	16
Fig. 2.8	The velocity profiles corresponding quarter riser design.	17
Fig. 3.1	Schematic diagram of low temperature simulated Hall cell	23
Fig. 3.2	Schematic diagram of current distribution in the end riser design of simulated cell.	24
Fig. 3.3	Heating arrangements of the simulated low temperature cell.	26
Fig.3.4	Schematic diagram of the Velocity probe used.	29
Fig. 3.5	Rack and Pinion arrangement for calibration of velocity probe.	31
Fig. 3.6	Calibration set up for calibration of the probe.	32
Fig. 3.7(a)	Calibration plot of 0 <sup>th</sup> channel (R-S pair) of the velocity probe.	35
Fig. 3.7(b)	Calibration plot of 1 <sup>st</sup> channel (P-Q pair) of the velocity probe.	36
Fig. 3.8	Variation of temperature in the simulated cell.	38
Fig. 3.9	Current Interruption Technique using the Data Acquisition System.	39
Fig. 3.10	The program window of Data Acquisition showing the nanovoltmeter reading of the two channels.	41

Fig. 4.1	Flow of current, basic busbar and collector bar connections, and the points where velocity were measured.	43
Fig. 4.2	Measured velocity distribution for “base” case in X-Z plane (Y=1.6 cm).	44
Fig. 4.3	Measured magnetic field distribution when input current is 528 A [7].	45
Fig. 4.4	Schematic drawing of the direction of Electromagnetic force at desired points derived from the measured magnetic field distribution and current density distribution.	47
Fig. 4.5 (a)	Measured velocity field at a depth of 1.5 cm of Wood’s metal (Y= 3.5 cm).	48
Fig. 4.5 (b)	Measured velocity field at a depth of 2.75 cm of Wood’s metal (Y= 2.25 cm).	49
Fig. 4.6	The relationship between velocity and square of current input at various locations.	51
Fig. 4.7 (a)	Measured velocity field for current density $0.75 \text{ A/cm}^2$ .	52
Fig. 4.7 (b)	Measured velocity fields for current density $0.50 \text{ A/cm}^2$ .	53
Fig. 4.8 (a)	Measured velocity distribution with anode cathode distance of 2.0 cm.	55
Fig. 4.8 (b)	Measured velocity fields with anode cathode distance of 1.5 cm.	56
Fig. 4.9	Measured velocity field with non conducting strips at the sidewalls.	57
Fig. 4.10	Measured velocity fields near points ‘3’, ‘4’, and ‘12’ as a test of sensitivity of measurements.	59
Fig. 5.1	Control volume for model formulation.	60
Fig. 5.2	The algorithm for computation of velocity field distribution.	63
Fig. 5.3 (a)	Comparison of predicted velocity and experimentally measured velocity at location point 1.	66
Fig. 5.3 (b)	Comparison of predicted velocity and experimentally measured velocity at location point 2.	67

Fig. 5.3 (c)	Comparison of predicted velocity and experimentally measured velocity at location point 4.	68
Fig. 5.4 (a)	Predicted velocity distribution in the cell with current density $0.5 \text{ A/cm}^2$ .	69
Fig. 5.4 (b)	Predicted velocity distribution in the cell with current density $0.75 \text{ A/cm}^2$ .	70
Fig. 5.4 (c)	Predicted velocity distribution in the cell with current density $1.0 \text{ A/cm}^2$ .	71
Fig. 5.5	Predicted magnetic field distribution when input current is 528 A [7].	72
Fig. 5.6 (a)	Predicted velocity distribution with ACD 2.0 cm.	73
Fig. 5.6 (b)	Predicted velocity field distributions with ACD 1.5 cm.	74
Fig. 5.7	Predicted velocity distribution with nonconducting strips put on the walls.	76
Fig. 5.8	Sensitivity test for model predictions at some points.	77
Fig. A.1	Schematic diagram of the simulated laboratory Hall-Heroult cell viewed from above.	84
Fig. A.2	Schematic diagram showing axis and coordinate of conductor AB.	86

## LIST OF TABLES

	Page No
Table 1	Analogy between the real life cell and the laboratory scale simulated cell. 22
Table 2	Reproducibility of velocity measurement in four different locations in three different days. 37
Table 3	Process variables and their ranges investigated. 42
Table A.1	The voltage distribution in an industrial Hall cell. 81
Table A.2	The physical property of Wood's metal. 81
Table A.3	Physical properties of aluminium, cryolite and Wood's metal. 82
Table A.4	Ratios of electrical conductivities. 82
Table A.5	Scale factor for different lengths. 82
Table A.6	Comparison of the kinematic viscosity and the Magnetic Reynolds number for aluminium, cryolite and woods metal zone. 83



## LIST OF SYMBOLS

$\vec{B}$	Magnetic field ( gauss)
$l$	Separation between the two tips of the probe.
$\vec{J}$	Current density (A/cm <sup>2</sup> )
$\sigma$	Electrical conductivity (Ohm <sup>-1</sup> cm <sup>-1</sup> )
$\rho$	Density of the liquid (gm cm <sup>-3</sup> )
$e$	Induced emf due to velocity
$J_{xz}$	Horizontal current (amp)
$J_y$	Vertical current (amp)
$B_y$	Vertical magnetic field (gauss)
$B_{xz}$	Horizontal magnetic field (gauss)
$\bar{U}$	Depth averaged velocity in X direction
$\bar{V}$	Depth averaged velocity in Y direction
$\mu_l, \mu_t, \mu_{eff}$	Laminar, Turbulent, and Effective viscosity
$\tau_{bx}, \tau_{by}$	Bottom shear stresses in x and y directions
$k$	Turbulent kinetic energy
$\varepsilon$	Turbulent kinetic energy dissipation rate

# CHAPTER 1

## INTRODUCTION

### 1.1 INTRODUCTION:

The Hall-Heroult cell is the universal commercial process for production of aluminium. The process is based on electrolytic decomposition of alumina dissolved in cryolite. The purified alumina dissolved in molten cryolite is decomposed at temperature of around  $960^{\circ}\text{C}$ . Figure 1.1 [1] is a schematic cross sectional view of a typical aluminium reduction cell.

A typical electrolytic cell consists of carbon anodes suspended from the top. The lower surfaces of the anodes are immersed in the molten electrolyte (alumina dissolved in cryolite, together with minor constituents). The electrolytically deposited molten aluminium is collected underneath the electrolyte also act as the cathode. A part of the pool is siphoned off the cell at regular intervals of time. An anode bus structure above the top of the cell distributes current to the anodes. Thus current enters the riser bus, goes to anode bus from where it is distributed to each anode. Then it flows in parallel through the anodes into the electrolyte, into the metal pool, into the carbon cell lining and out of the cell by means of steel collector bars inserted into the carbon cell lining. A cathode bar collects current from all the collector bars to the riser bar on the adjacent cell. A typical modern cell usually of 3 meters by 8 meters in its horizontal dimensions carries 100-200,000 amps current, and containing ten to twenty anodes, and operates at  $960^{\circ}\text{C}$ . Cells are connected in series to form pot-lines consisting of 100-200 cells. A several tens of cells connected in series and are arranged in lines known as potlines and an aluminium plant might contain several potlines.

The large currents within a cell, surrounding conductors and adjacent cells generates strong electromagnetic field within the two liquids contained in the cell. Electric current flowing through molten aluminium and the electrolyte interacts with the electromagnetic field, present in this fluid, to generate Lorenz forces, which are the origin of the magnetohydrodynamics phenomena. This is primarily responsible for: (a) imparting velocities to both molten Al and cryolite and, (b) oscillation of aluminium-cryolite interface. The main concerns of these oscillation is that if it grows and reaches a

value as high as the thickness of cryolite layer, they will lead to an electrical contact between the molten aluminium and the bottom of the anode, creating a short circuit in the cell. This hurts the production process by process held ups and makes the process less energy efficient. A huge amount of energy is consumed in the production of aluminum from its ores. Out of the total energy consumed in the process of aluminium extraction the 76% i.e. a major part of it is consumed during the smelting process in Hall-Heroult Cell only. So there is sufficient interest in making the process energy efficient. Since the energy consumption is dependent on magnetohydrodynamics phenomena occurring in the cell, there is presently considerable interest in better understanding this phenomenon. Thus, the proper control of electromagnetics in Hall cells is the key to development of higher amperage cells and making the existing cell more energy efficient.

## **1.2 PROCESS PERFORMANCE OF HALL-HEROULT CELLS:**

Smooth functioning of a Hall cell requires a close control of operating parameters like bath chemistry, bath temperature, current density, and designs of anode, busbar, and collector bars. The common problems associated with the operation of the cell are anode effect, change in bath chemistry, instability of the metal pad, melting of the protective ledge and the lower energy efficiency.

During the process of electrolysis gradual depletion of alumina in the bath occurs, when it goes down to 0.5-2.2 % [2]. It promotes the dewetting characteristics of the anode surface results in accumulation of gases formed (like  $\text{CF}_4$ ,  $\text{C}_2\text{F}_4$ , and  $\text{CO}$ ) under the anode by forming an insulating gas film. As a result, the cell voltage rises from the normal voltage of 4.5-5 V to 20-40 V. This phenomenon is termed as Anode effect. This causes overheating of the cell, resulting in melting of the protective ledge. This breaks down the thermal balance of the cell due to extra energy consumption, the refractory consumption increases which in turn lead to an increase in replacing frequency of the cell. The process economy gets adversely affected due to increased consumption of refractory and reduced production per cell due to increased production held ups

On the other hand when the alumina concentration in the cryolite goes beyond the dissolution limit, the undissolved alumina tends to accumulate on the bottom of the cell, forming the sludge. This is undesirable too since it disrupts the flow of current in the cell,

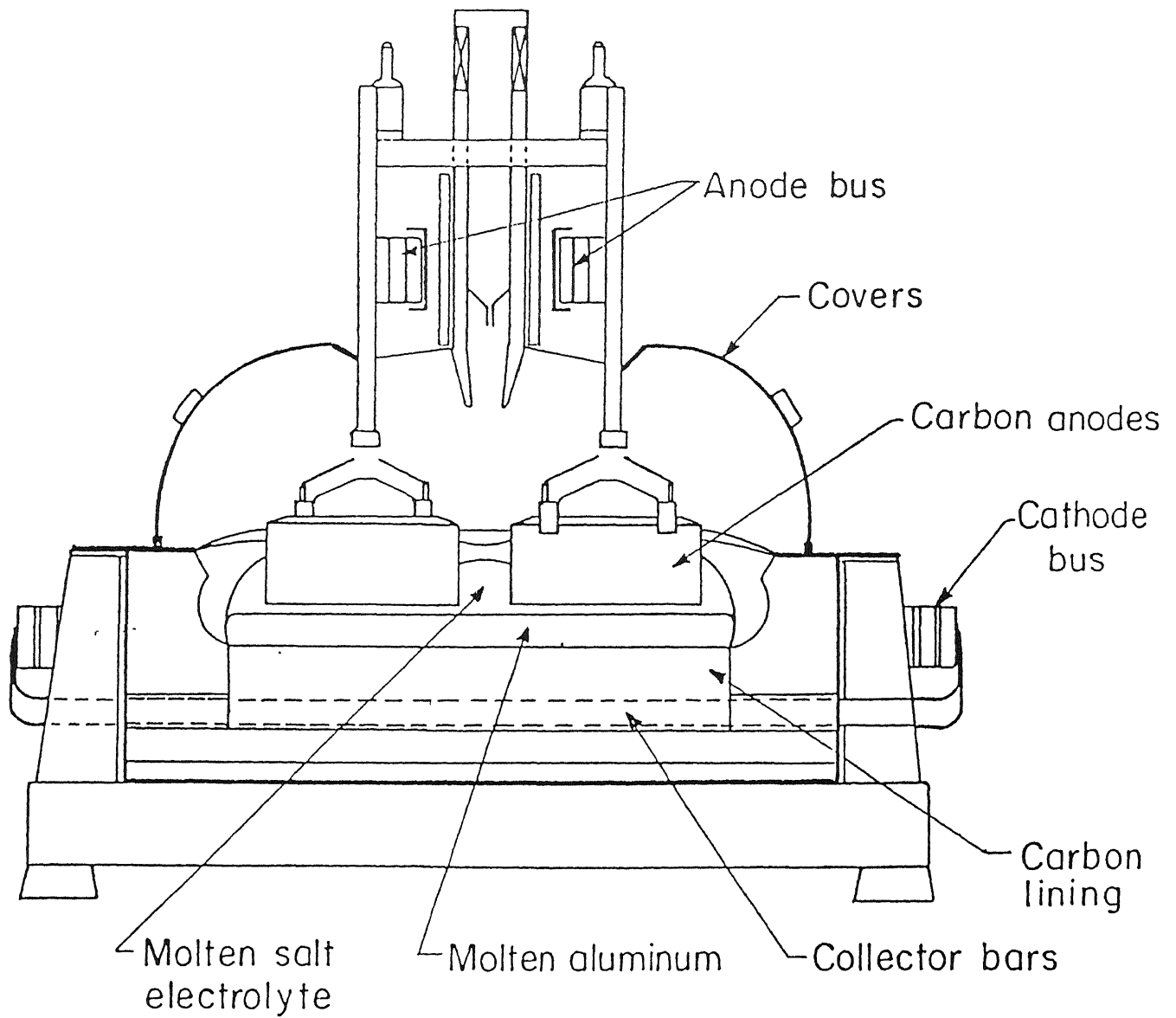


Fig. 1.1 Cross sectional view of typical industrial Hall-Heroult cell [1].

giving rise to unstable cell operation. So bath chemistry also plays a crucial role in smooth operation of the cell.

Due to the electromagnetic stirring, and evolution of gases like CO and CO<sub>2</sub> the metal pad becomes unstable, often leading to short circuiting of the aluminium pad and anode. As a result, overheating takes place due to excessive current densities and to passage of current through the cell without the usual electrochemical reduction of alumina to aluminium. This localized high temperature may melt the protective ledge causing higher consumption of refractory.

Current efficiency and specific energy consumption characterizes the process performance. The Current efficiency is defined as the ratio of mass transport rate of aluminum to cathode to the theoretical aluminum production rate as expected from Faraday's law. The Current efficiency has been increased up to 95% in most commercial

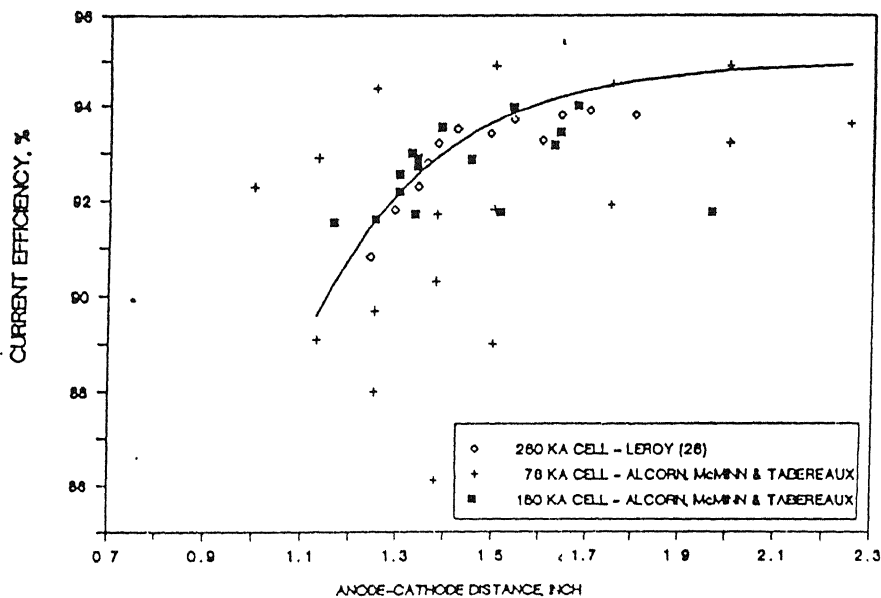


Fig. 1.2 Current efficiency Vs anode cathode distance (ACD) [3].

cells. The parameters that affect the current efficiency are anode cathode distance (ACD), temperature, current density, and bath ratio ( $\text{NaF}/\text{AlF}_3$ ) etc. The relationship between the current efficiency and ACD is shown in the Fig. 1.2[3].

The Specific energy consumption of good cells remains as high as 12.9 kWh/kg against theoretical value of 6.2 kWh/kg [4], i.e. energy efficiency is only close to 48 %. The reason for this low energy efficiency is directly linked with voltage drops across different components of the electrolytic cell like the anode stem, studs, carbon lining and electrolytic bath, apart from electrochemical decomposition potential of aluminium. About 40 % of the total voltage is dropped only in the electrolytic bath contained between the anode and the cathode, which could be further lowered. Minimization of voltage drop in the bath will be a meaningful effort in the direction of making the process energy efficient. The voltage drop across the bath is directly related to the ACD. Though decreasing ACD results in a gain in specific energy consumption, but at the same time if it goes below an ACD of 3.5 cm the current efficiency is drastically reduced (Fig. 1.2) because the probability of short circuiting between the aluminium pad and anode surface gets increased. To keep the current efficiency high if we go for higher ACD the specific energy consumption increases. Hence, the proper ACD should be maintained so as to obtain optimum current efficiency and specific energy consumption. The adverse effect of lowering ACD can be taken care of by improving the cell insulation and improved cell design to achieve a thermal balance even at a lower ACD. The better control over the oscillation of the interface between aluminium and electrolyte can be obtained by controlling the magnetohydrodynamics of the cell.

### **1.3 ROLE OF MAGNETOHYDRODYNAMICS:**

Magnetohydrodynamics (MHD) is the interaction of conducting fluids with an electromagnetic field. Large current in the order of 150-300 kamps flows through the Hall cell, which in turn generates strong magnetic field both due to the current flow through the cell, termed as internal current and the external current carrying conductors. This magnetic field on interacting with the current flowing through the cell gives rise to large electromagnetic forces, which provides motion to the melt, and the aluminium pad present at the bottom [5] and makes the interface unstable giving rise to formation of

waves similar to the waves at the surface of lakes and seas. The main concern about these waves is that, if their amplitude grows and reaches a value as high as the height of ACD, it provides to an electrical contact between the molten aluminium and the anode, creating a short circuit in the cell. This MHD phenomenon, which apart from resulting in momentary short circuiting to the anode, produces erosion of the carbon lining of the cell. So Avoidance of the MHD instability is one of the key factors in successful pot operation. The MHD instability gets suppressed when the ACD is increased, but then the energy efficiency goes down. On the other hand the lower ACD results in lower current efficiency, disturbed heat balance and MHD instability. So the efforts of the technology experts are aimed at maintaining the quietened metal bath interface by reducing the electromagnetic torque by altering the design of the cell for smooth operation of cells with low energy consumption. The present investigation is continuation of an ongoing research work in our Laboratory, funded by department of science and technology. The magnetohydrodynamics in the Hall-Heroult cell is being studied both through experimental and mathematical modeling concurrently. In the experimental part we go for measurement of current density distribution, magnetic field distribution, and velocity field distribution. Simultaneous to this current density, magnetic field, and velocity distribution are modeled to put altogether to solve this problem. Because of the difficulty in measurements on actual cell, measurement of magnetohydrodynamics is done on simulated Hall cell. Validations of the mathematical model predictions are done by using experimental data generated on the simulated cell.

## **CHAPTER 2**

### **LITERATURE SURVEY**

#### **2.1 BRIEF REVIEW OF PREVIOUS INVESTIGATION**

Occurrence of magnetohydrodynamics phenomena in aluminium electrolysis has been known ever since the invention of the process. However, the importance of it was realized only much later when the concerted efforts were made to substantially improve cell capacity in 1950s. It then became evident that the magnetic field was one of the bottlenecks in designing higher capacity cells. The magnetohydrodynamics phenomena occurring in Hall cells have a detrimental effect on cell performance in terms of lower current and energy efficiencies. Various investigators have attempted to study magnetohydrodynamics prevailing in a cell through direct measurements of current, magnetic, and velocity fields, and/or through mathematical model that could predict these fields. Since the focus in this investigation is on velocity field distribution, the emphasis in this section is given to the review of literature pertaining to this topic. However, for sake of completion a brief discussion of literature on current density and magnetic field distribution has also been included and it precedes discussion on velocity field distribution.

**2.1.1 CURRENT DENSITY DISTRIBUTION:** The current density distribution in the cell was modeled by Lympany et al. [8]. Validation of the mathematical models was done by using experimental data generated by Lee et al [6] by carrying out measurements on a physical model satisfying the similarity condition of a real life industrial cell. The current density distribution as predicted by Lympany et al. [8] is depicted in Fig. 2.1. The large horizontal current in the cell should be noted which affects the magnetohydrodynamics of the cell. This gave an insight to the current density distribution in real cells. Three-dimensional current distribution in a simulated cell was concurrently modeled and experimentally validated by Bhunia [7]. Figure 2.2 shows the current distribution through the simulated cell [7]. An electromagnetic probe was used for measuring current density in the simulated cell. Effects of different parameters like input current, solidified ledge,



etc on current density distribution were studied. Insulating plastic sheets, simulating the ledge were placed on the sidewall of the cell and current density measured. Comparison of current densities with and without the plastic sheets led to the conclusion that reasonable amount of current flows through the cell walls when these are not covered by the plastic sheets. The details of current density distribution in three dimensions are presented elsewhere [7]

**2.1.2 MAGNETIC FIELD DISTRIBUTION:** The magnetic flux density in the Hall cell was measured in ALCOA laboratories by Ziegler and his co-workers [1]. They carried out a large number of measurements on several cells, and their measurements showed a large

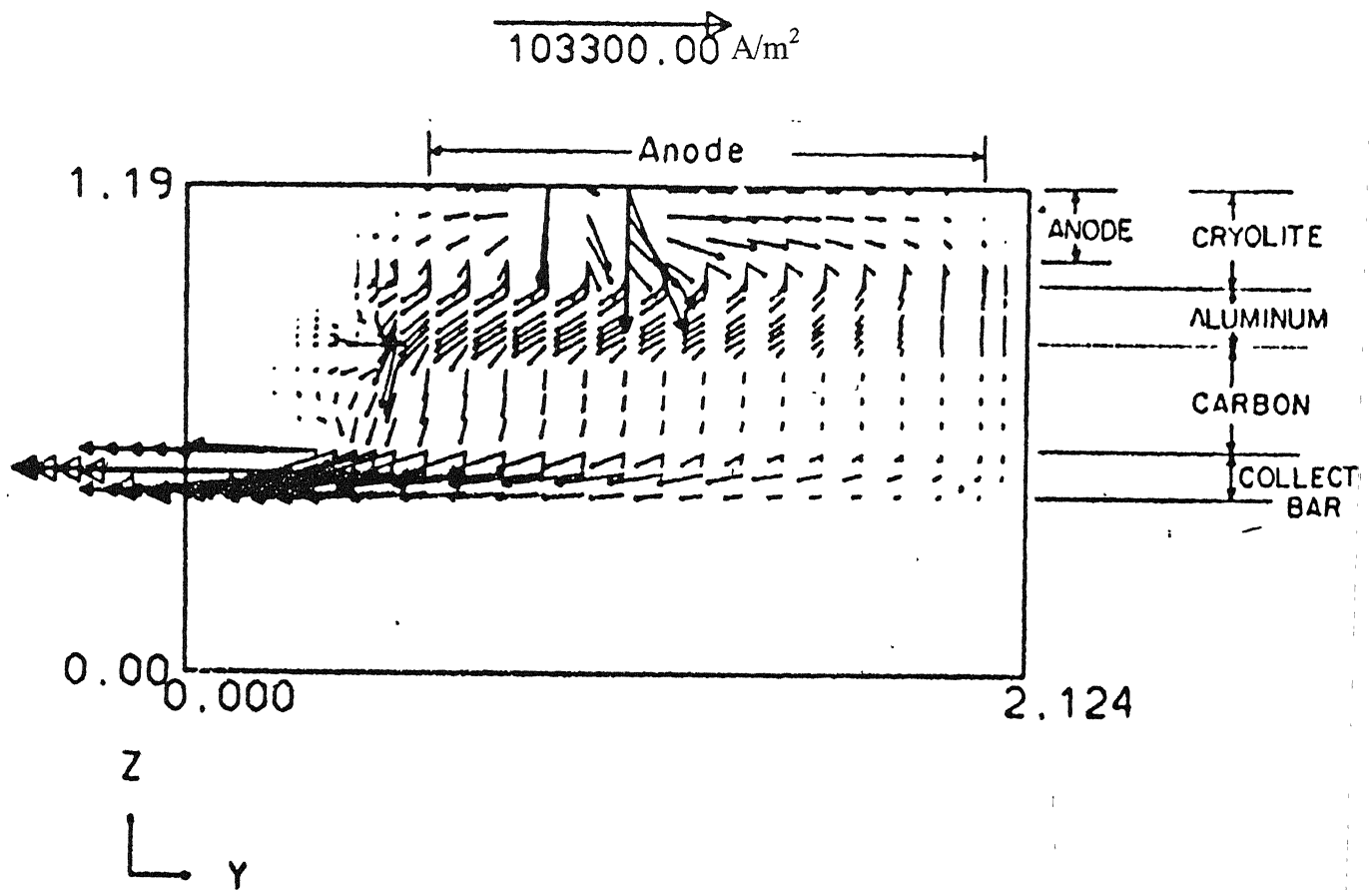


Fig. 2.1 Current densities within a half section of the cell for a quarter riser design [8].

Supplied current = 264 A

ACD = 2.5 cm

$2 \text{ A/cm}^2$

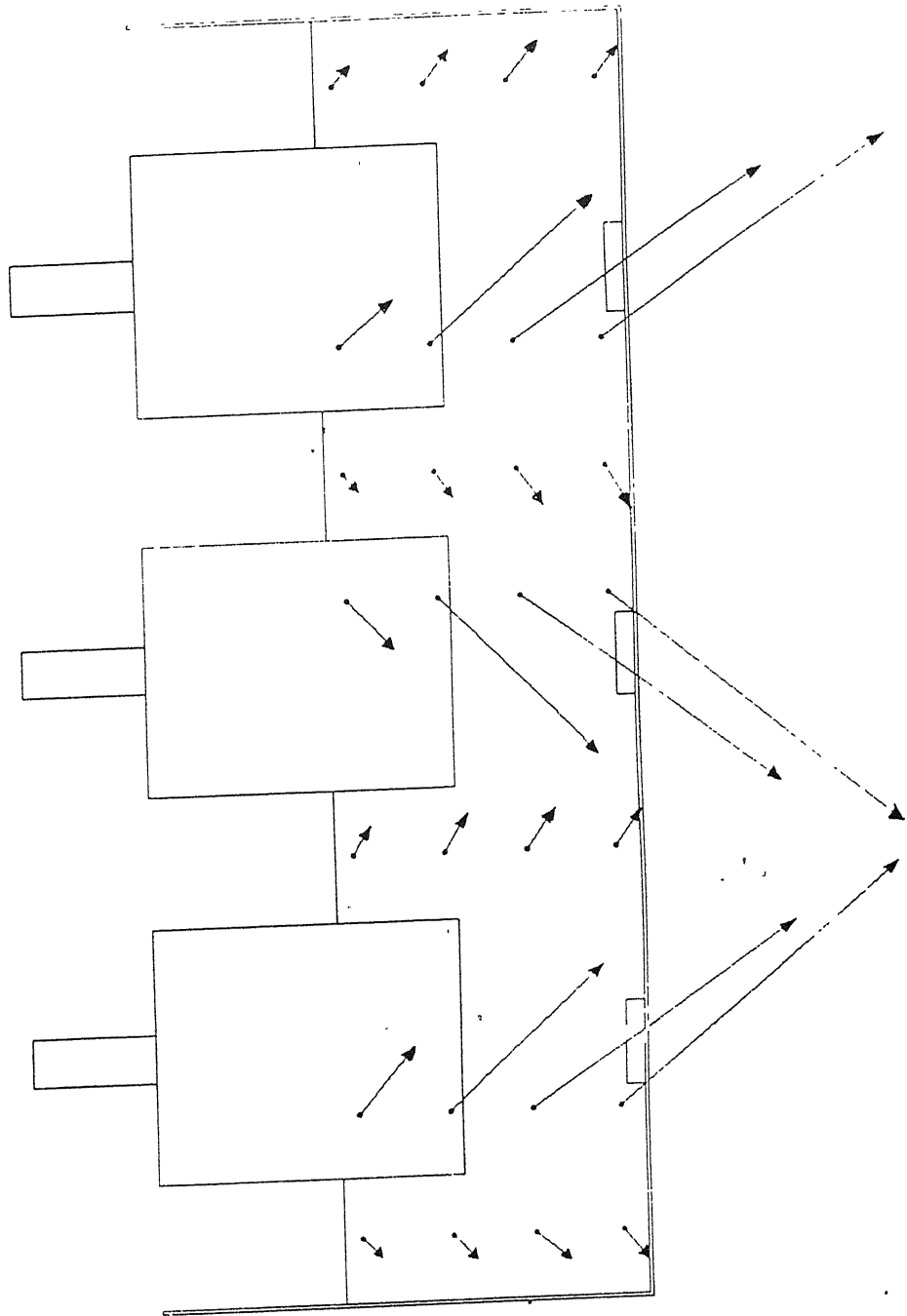


Fig. 2.2 Current distributions within the cell containing aluminium pad at the cell bottom with end riser design [7].

cell to cell variability. Hence, they concluded that a good agreement between the magnetics models and the experimental results in industrial cells would be achieved only by considering average value of number of these measurements. Segatz and his co-workers [9] studied the effect of steel parts on magnetic field in the Hall cell and established that the geometric modeling of steel parts and the shell affected the magnetic field within the cell. This study provided a methodology for more accurate calculations of magnetic field distribution within a cell. Evans and his coworkers [10] also studied through mathematical models the effect of the bus bar design and spacing between the neighboring cells on magnetic field, melt velocity, melt topography and current efficiency. Thus there has been a growing interest in considering the various components like anode rod, bus bars, and the presence of neighboring cells while calculating the magnetohydrodynamic field in the metal bath to have a better understanding of the magnetic field within the cell. The magnetic field has also been modeled by Bhunia [7]. The details of the magnetic field distribution are presented elsewhere [11].

**2.1.3 VELOCITY DISTRIBUTION:** Physical modeling of Hall-Heroult cell was done by Lee and et al. [6] wherein a cell was employed with a single layer of molten Wood's metal as melt, and fourteen suspended stainless steel blocks as anodes. They carried out the velocity measurements using the physical model, shown in Fig. 2.3[6]. The observed circulation pattern was not uniform owing to the non uniform distribution of current through the anodes. Velocity measurements for the similar model were also carried out by Banerjee et al. [12]. Their results are shown in Fig. 2.4. But their velocity patterns did not match with those previously obtained results by Lee et al [6]. Their approach was simultaneous measurement of velocity along with the magnetic field. The understanding was based on an examination of torque exerted by the electromagnetic forces. They concluded that the motion of the melt is responsive to variation in electromagnetic forces. They examined various cell designs and studied their effect on the magnetic field, which in turn affected the flow within the melt Evans et al. [10] also formulated mathematical

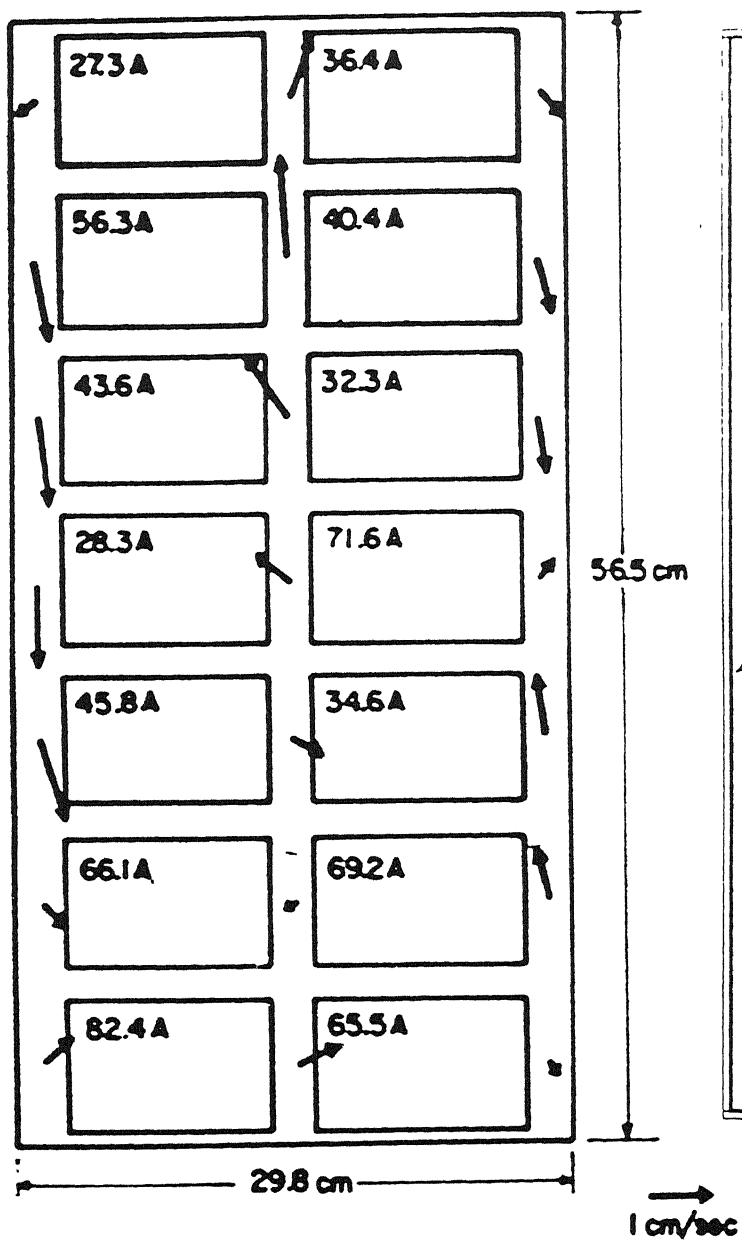


Fig. 2.3 Measured velocity vectors on Physical model with its fourteen anode configuration with end riser design [6].

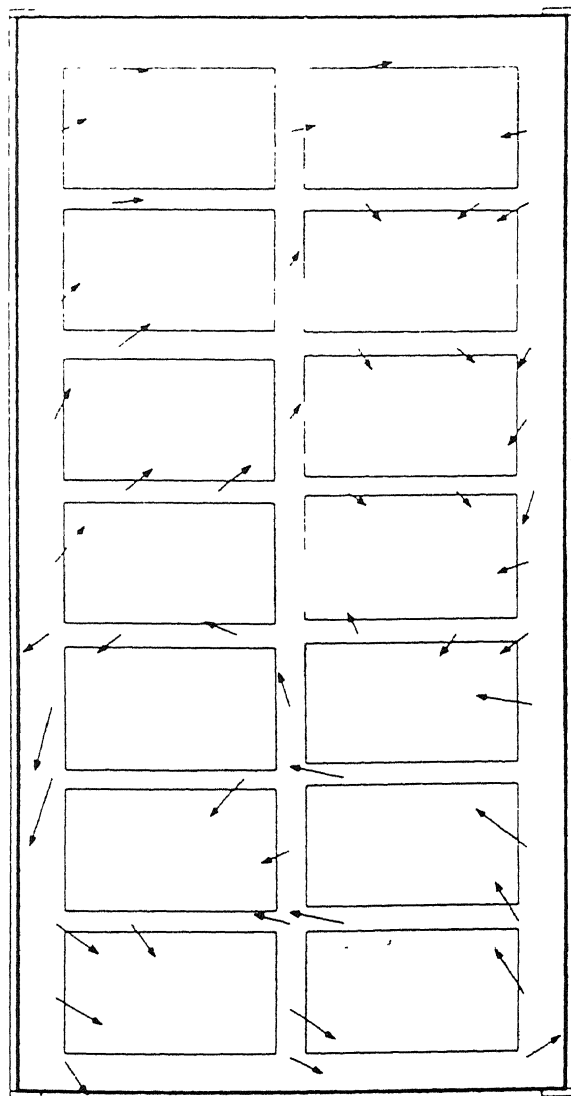


Fig. 2.4 Measured velocity field distribution in a single layered simulated cell with end riser design [12].

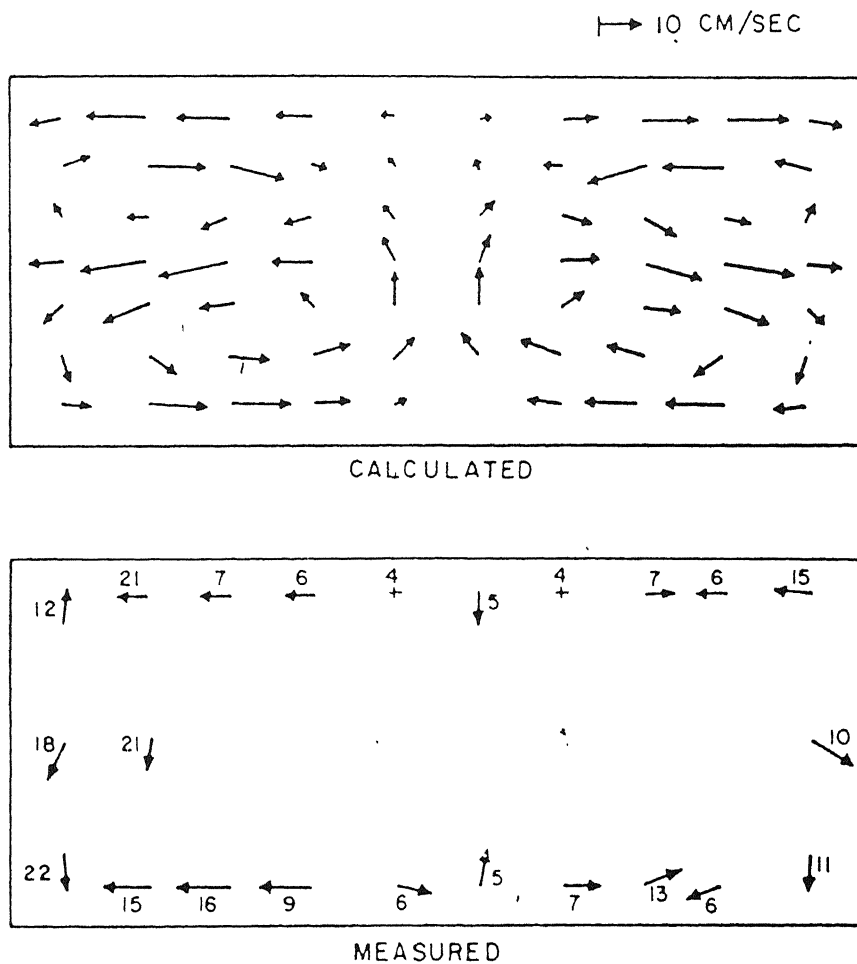


Fig. 2.5 Calculated and measured velocities within the molten aluminium of the 185 kA cell [10].

models to predict the currents, magnetic fields, and melt velocity. The predicted velocity was compared with the experimentally measured velocity within the molten aluminium as shown in the Fig. 2.5 [10]. It was noted that the computed velocity showed a poor agreement with the measured velocity particularly in terms of directions. Segatz and Droste [5] attempted to correlate the instability of electrolyte-metal interface in Hall cells

with the prevailing magnetohydrodynamic conditions. They could establish that the instability at the interface depends both on the fluid flow pattern as the magnitude of the melt velocity.

## **2.2 FACTORS AFFECTING HYDRODYNAMICS IN HALL CELL:**

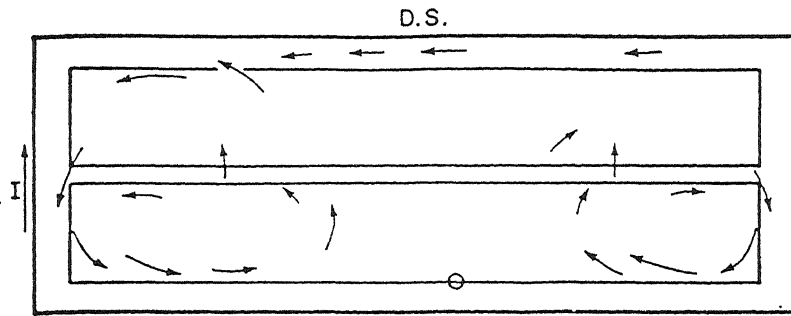
The factors that affect the hydrodynamics in Hall cells are studied by various investigators and are summarized below

**2.2.1 AGE OF THE CELL:** Johnson developed a technique for velocity (flow) measurement in the electrolyte layer [13]. In this technique the dissolution of an iron rod, dipped in the electrolyte, was monitored. Under the convective flow conditions, which prevail in the cell, the rate of dissolution of the rod could be directly correlated with flow intensity. The melt flow was measured over a period of two years. For the same operating conditions the velocity pattern in young and older cells were found to be distinctly different. This variation was attributed to the freeze profile that changed with the age of the cell. The velocity patterns and corresponding freeze profiles are shown in Fig. 2.6 [17].

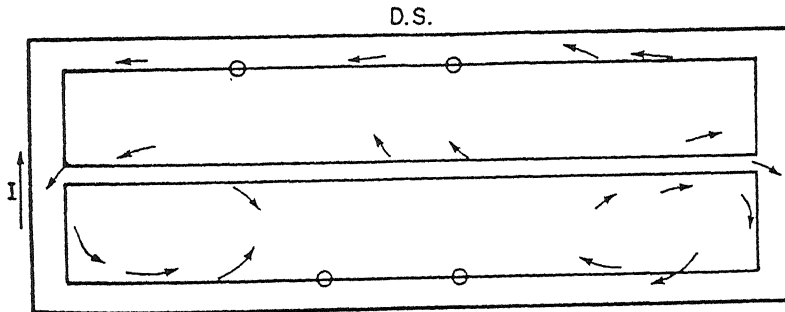
**2.2.2 LEDGE SHAPE:** The effect of the ledge in the cell is two fold. The main advantage of having the ledge is that it ensures that the permanent side lining does not come in contact with the bath directly thereby reducing the erosion rate resulting in improved lining life. It has also been established that a good ledge profile stabilizes the metal pad-electrolyte interface from cell disturbances. However, it has been observed that if the ledge profile extends horizontally towards the center of the cell beyond an optimum value it makes the interface unstable [14] As the ledge grows, it reduces the effective cathode area increasing the horizontal component of the current flowing in the melt. This directly affects hydrodynamics in the cell.

**2.2.3 BUS BAR SYSTEM:** The bus bar arrangement has great role in deciding the magnetohydrodynamics of Hall cells. In general, there are three busbar designs: (i) end riser, (ii) quarter riser design, and (iii) Novel riser design, as shown in the Fig.2.7 [8].

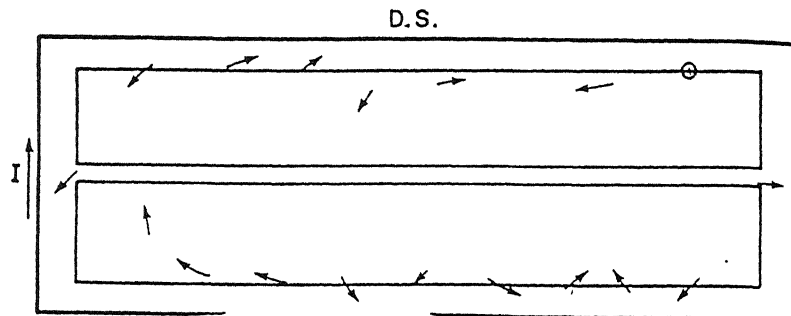
METAL FLOW IN CELLS <150 DAYS OLD



METAL FLOW IN CELLS 150-400 DAYS OLD



METAL FLOW IN CELLS 400-900 DAYS OLD



METAL FLOW IN CELLS >900 DAYS OLD

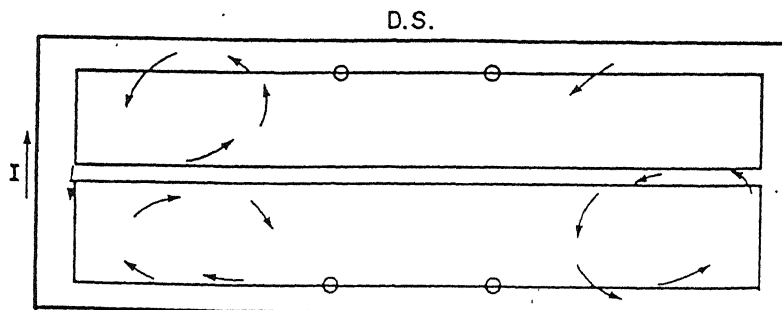


Fig. 2.6(a) Flow pattern in a cell at different ages [17].

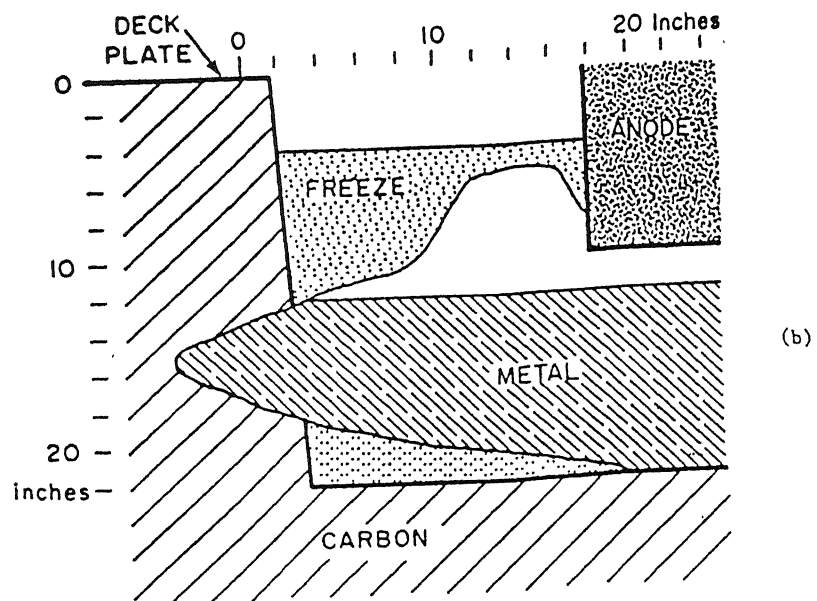
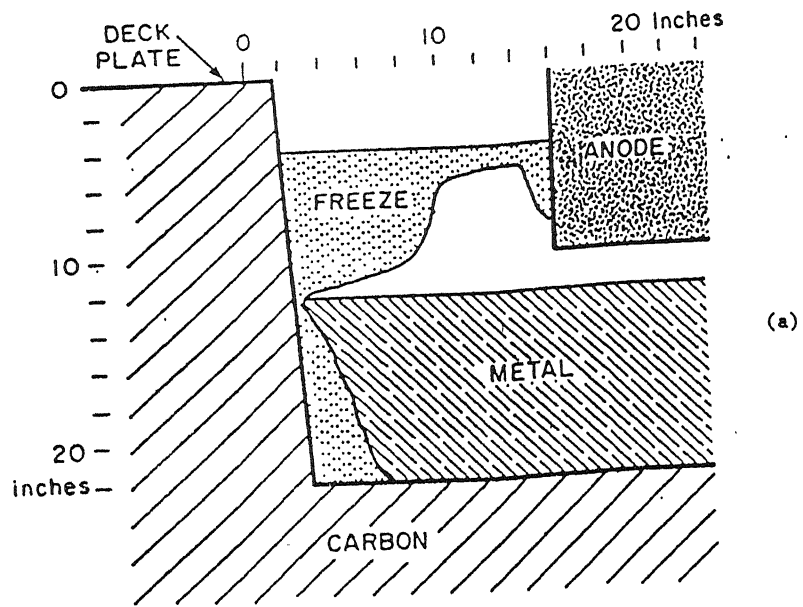
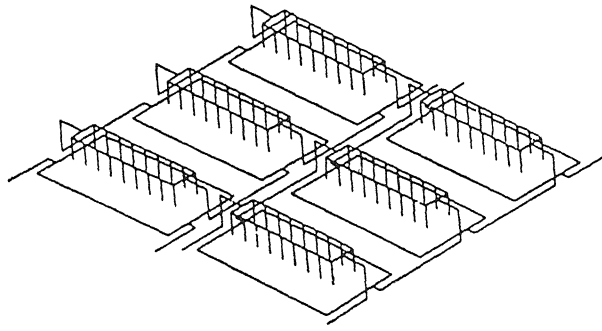
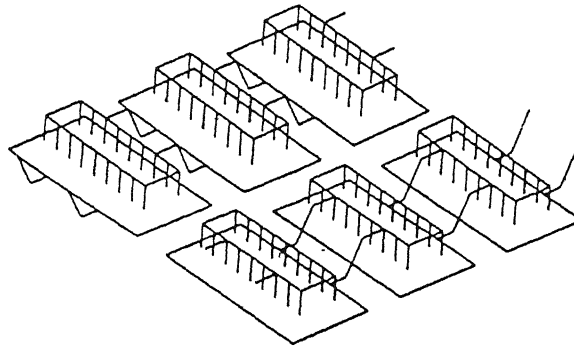


Fig. 2.6(b) Freeze profiles (i) <150 days, and (ii) >900 days [17]

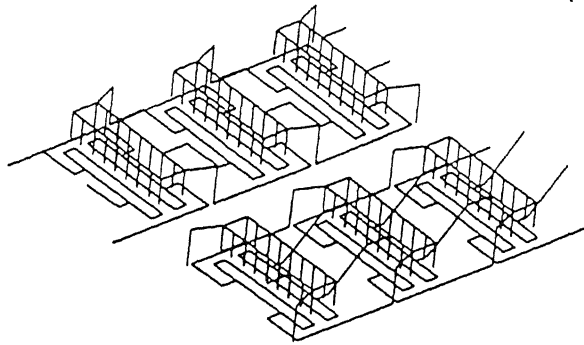




(i)



(ii)



(iii)

Fig. 2.7 Schematic diagram of (i) End riser, (ii) Quarter riser, and (iii) Novel riser design [8].

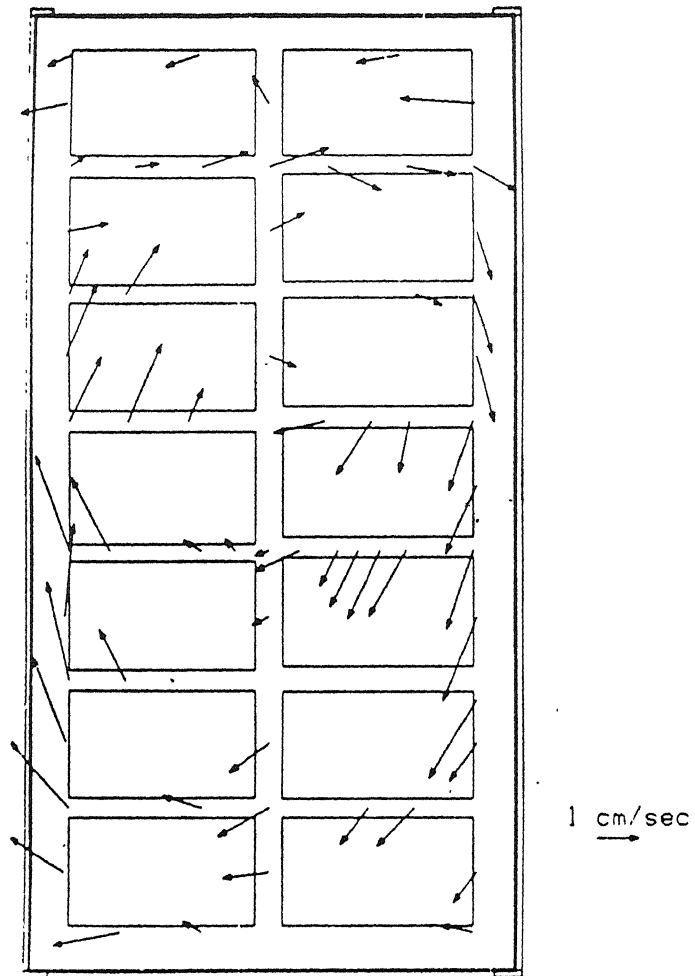


Fig. 2.8 The velocity profiles corresponding quarter riser design [12].

Lymphany et al. [8] studied the effect of riser designs on the current efficiency of the cell. Banerjee and et al. [12] made the measurements on magnetic fields in electromagnetically driven melt flows by changing the busbar design and observed the variation in the flow profile. The velocity profiles corresponding to quarter riser design as against the end riser design (Fig. 2.4) are shown in Fig. 2.8. There is a change in the velocity pattern with a more rapid clockwise circulation. This is attributed to a substantial increase in the clockwise torque due to the magnetic field distribution in the cell in case of the quarter riser design.

**2.2.4 ANODE GEOMETRY:** Anode geometry affects the energy efficiency of the Hall cells. Shekhar et al. [15] studied the effect of anode geometry on current and energy efficiencies. They concluded that submerged grooved anodes are best for achieving higher energy efficiency, as they would provide a channel for the escape of gas bubbles generated during the process. Furthermore, the grooves would result in increased surface area for the anodic reaction, compared to the flat anode. Anode dimensions determine the channel that is formed in between anodes, and anode and sidewalls. The anode tilt affects the flow pattern as it changes the interpolar resistance as studied by Shekhar et al. [15]. Though it results in a non-uniform flow pattern, it drives the gas bubbles easily making the process energy efficient.

**2.2.5 ANODE CATHODE DISTANCE:** The largest voltage drop (about 40%) in a typical Hall cell occurs in the bath in Anode cathode gap [Table A.1]. The effect of ACD has been investigated in a full-scale simulated physical model developed by Fortien et al [16]. Velocity decreases as ACD is reduced. Large ACD causes strong damping of the oscillation of the metal pad. For unstable cells generally the ACD is increased to reduce the periodic oscillation of the cell voltage. In order to decrease the ACD to make the cell energy efficient, the idea of using inert anode has been a focus for research for quite some time.

**2.2.6 COLD ANODE:** Anodes used in Hall cells are consumable carbon anodes. Hence, these need to be replaced as and when these are almost consumed. Typically one anode is

replaced everyday in a multi anode Hall cell. When a new anode is introduced into the cell, it is usual that the cold anode will carry only a little amount of current as the electrolyte gets frozen as soon it comes in contact with it. It takes a while before the frozen electrolyte is remelted. This maldistribution of the current in the anodes disturbs the cell performance. This upset was simulated by Banerjee et al. [12] by putting insulating coatings on one of the anodes. A significant change in the velocities around the anode was observed.

## **2.3 SCOPE/OBJECTIVE OF THE PRESENT INVESTIGATION:**

Several studies based on mathematical modeling of thermal behavior in Hall cells are available in literature. As compared to these, studies on MHD are much fewer. More than the models formulation, the major problem that one encounters is in validation of these models. In principle it should be possible to get all the data needed for validation on commercially operated Hall cells. In reality, however, it is not so-the data often are not readily available, and even if these are available they are not reliable. To carry out a separate campaign to generate data on plant scale cells is exceedingly expensive and difficult. Attempts to generate required experimental data on a laboratory scale model of multi anode Hall cell have also not been successful. At least in published literature, there is no such investigation reported. The main problem in running a laboratory scale arises due to very large heat losses because of large surface area to volume ratio in small cells. Any external heating of the cell to compensate for these heat losses prevents the formation of electrolyte ledge which is absolutely essential to protect the carbon lining on cell walls from highly corrosive attack of the hot electrolyte. As a result, the carbon lining is consumed in just a few hours making the continuous cell operation impossible. A few investigators have attempted to mathematically model MHD in electrically driven melts in cells containing one or more anodes suspended from the top. Some of them have also attempted experimental measurements of current, magnetic, and velocity fields in the cell. The velocity distribution in a simulated cell has been predicted by Evans et al. [10]. It, however, shows a large discrepancy in velocity profile when compared with the experimental values on the similar cells. Due to the paucity of experimental data even on the simulated cells, rigorous validation of MHD models has so far not been possible.

The present investigation is a part of the major project entitled ‘Studies on MHD in electrically driven flows’, which is being carried out in our laboratory. Realizing the fact that the meaningful experimental measurements would be possible only on a simulated Hall cell, the overall project was divided into the following parts:

- (i) Setting up of a laboratory scale simulated Hall cell.
- (ii) Measurements of current, magnetic, and velocity fields for various operating conditions.
- (iii) To develop mathematical models to predict current, magnetic field, and velocity fields, and make predictions for the simulated cell.
- (iv) To validate these mathematical models using experimental data on these cells.

Hence, a laboratory scale physical model (approximately  $1/10^{\text{th}}$  scale and operated at about 600 amperes current) was constructed to simulate the electromagnetically driven flow occurring in an industrial Hall cell. Wood’s metal which melts at about  $\sim 70^\circ\text{C}$  simulates the electrolyte. Similar physical models have also been used by Evans et al. [6]. It should, however, be realized that the cells involving single melts represent only a poor simulation of actual Hall cells which have two conductive liquids- the electrolyte and the metal pad. To the best of our knowledge, no investigation on MHD measurements has been carried out employing a simulated cell containing two distinct layers. Present investigation is an attempt in this direction. While Wood’s metal simulates the electrolyte, the second conductive layer is simulated by a solidified aluminium layer in between carbon lining and Wood’s metal.

Results of extensive mathematical modeling and experimental measurements on current density and magnetic field distribution have been presented in two earlier M.Tech. theses from our laboratory. The primary objective of this research, presented in this thesis, is towards studying the velocity distribution both through mathematical modeling and experimental measurements in the simulated cell. An end riser design of the busbar system has been used throughout this investigation. The effect of process parameters like total input current, current density, anode-cathode distance, depth of measurement, and ledge profile on velocity field has been studied. Velocity measurements have been carried out using an in-house fabricated velocity probe. The

experimental data have been used to validate the mathematical model. Commercially available software 'PHOENICS' has been used to solve these model equations. Whenever mathematical model and experimental data on current and magnetic fields are required to discuss the results of these investigations, they have been taken from the previous investigations carried out in our laboratory.

## **CHAPTER 3**

### **EXPERIMENTAL STUDIES**

#### **3.1 EXPERIMENTAL SET UP**

The objective behind this investigation was to investigate magnetohydrodynamics concurrently using the approaches of experimental measurements and mathematical modeling. The experimental data needed to validate the mathematical model, were generated using simulated low temperature Hall cell, which employs molten Wood's metal simulating the electrolytic bath. The physical model constructed in this study satisfied the geometrical, dynamic, and thermal similarity criteria. The limitation of the simulated cell however, was that it did not satisfy the chemical similarity condition and there were no neighbouring cell unlike the real life potlines where the behavior of each cell affects the functioning of the adjacent cells in the same pot-lines with respect to the electromagnetic field interfering with each others. The simulated low temperature model was also imperfect in the sense that it contained only one conducting melt (Wood's metal) moving under the influence of electromagnetic forces without any gas bubble generation at the anodes. However, the following analogies could be drawn on physical model with respect to the real life Hall cell.

Table1. Analogy between the real life cell and the laboratory scale simulated cell.

	<b>Industrial cell</b>	<b>Simulated cell</b>
Electrolyte	Cryolite	Wood's metal
Anode material	Carbon	Stainless steel
Cathode	Molten Al pool	Solid Al layer (new cell)
Collector bar	Steel bar	Copper collector bar
Cell Lining	Carbon lining	Stainless steel

**3.1.1 COMPONENTS OF THE EXPERIMENTAL ASSEMBLY:** The simulated laboratory scale Hall cell has the basic components as shown schematically in Fig.3.1.

**(i) Stainless Steel Rectangular Tank:** The rectangular stainless steel tank which can hold up to 50 kg of simulating liquid (wood's metal) simulates the cavity of the Hall cell.

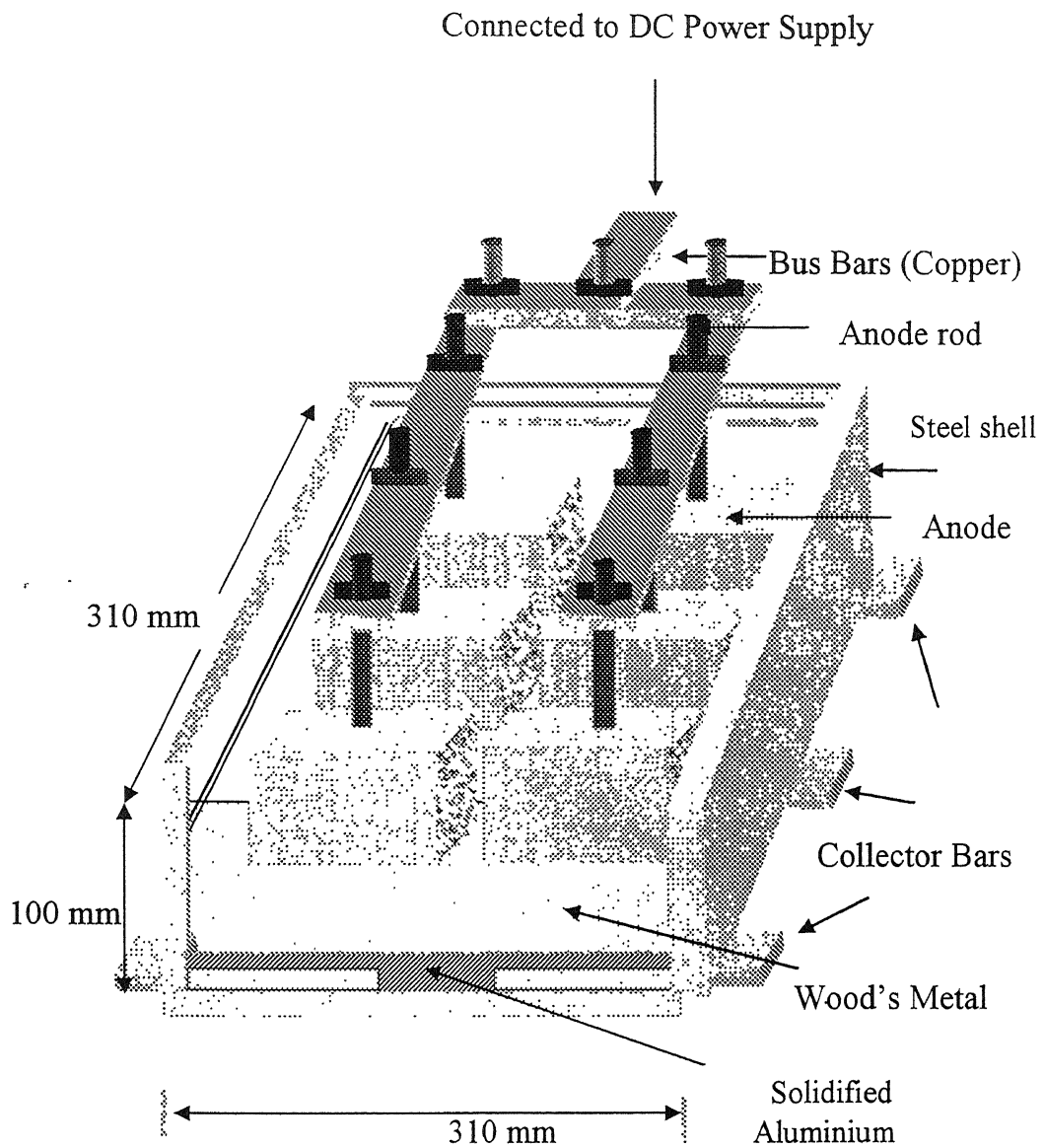


Fig. 3.1 Schematic diagram of low temperature simulated Hall cell



The tank ( $31 \times 31 \times 10 \text{ cm}^3$ ) is made of 0.15 cm thick stainless steel sheets. The tank is basically welded and made leak proof by high temperature sealant capable of withstanding up to  $250^\circ\text{C}$  without failing. The collector bars are inserted through the slots cut on the opposite sides of the tank and are welded to the base sheet of the tank.

**(ii) Anode Assembly and Bus Bars:** Rectangular stainless steel blocks ( $12 \times 8 \times 6 \text{ cm}^3$ ) representing anodes are suspended from copper bus bars running across the top of the model with the help of anode rods made of copper. Figure 3.1 shows schematically the details of anode assembly. The connection of power supply to the busbar is by end riser design. The direction of flow and the distribution of current are shown in Fig. 3.2 schematically.

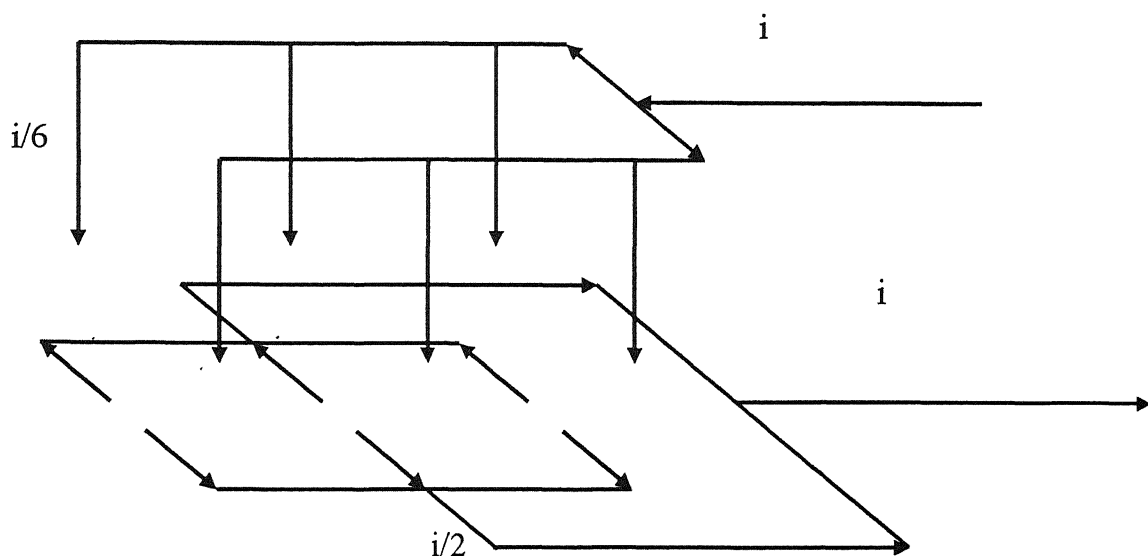


Fig. 3.2 Schematic diagram of current distribution in the end riser design of simulated cell.

**(iii) Cathode collector bars:** Copper strips of thickness 0.5 cm are used as cathode collector bars. Three copper strips each on both the sides of the tank coming out of the slots are employed to collect the current.

**3.1.2 ACCESSORIES TO THE CELL:** The accessories to the laboratory scale low temperature simulated cell are described below.

**(i) Material used in the simulated cell:** The material used in the laboratory cell is Wood's metal, which was selected as the model fluid because of its high electrical conductivity and low melting point; the latter makes the measurement of velocity feasible even at low temperatures. An alternative to Wood's metal could have been mercury but due to its toxicity, it was not used. Various physical properties of Wood's metal are given in the appendix.

**(ii) Heating arrangements of wood's metal melting:** In a previous study involving a simulated cell, reported in literature [6] a hot water bath filled with a thermo-stated heater was used. In the present investigation it was decided to replace the hot water bath by a chamber in which the hot air is circulated. This arrangement was found to be more efficient. The heating element used to heat up air is a silicon carbide element. An air circulation system is employed to ensure fast and uniform heating of the Wood's metal. This heating arrangement system is schematically shown in Fig. 3.3.

**(iii) Power supply and Current measuring instrument:** A DC power supply [Model #6681A (0-8V/0-580A) of Hewlett Packard] is used as the source of current. Current flowing through various conductors is measured using a True RMS Clamp meter (#DM DCM 39(0-1000A)).

**(iv) Temperature control and measurement:** Controlled voltage input through a variac to the SiC rods essentially controls bath temperature, which is measured using an alumel-chromel thermocouple (TC). To protect the thermocouple tip from being corroded, it is kept in a stainless steel tube.

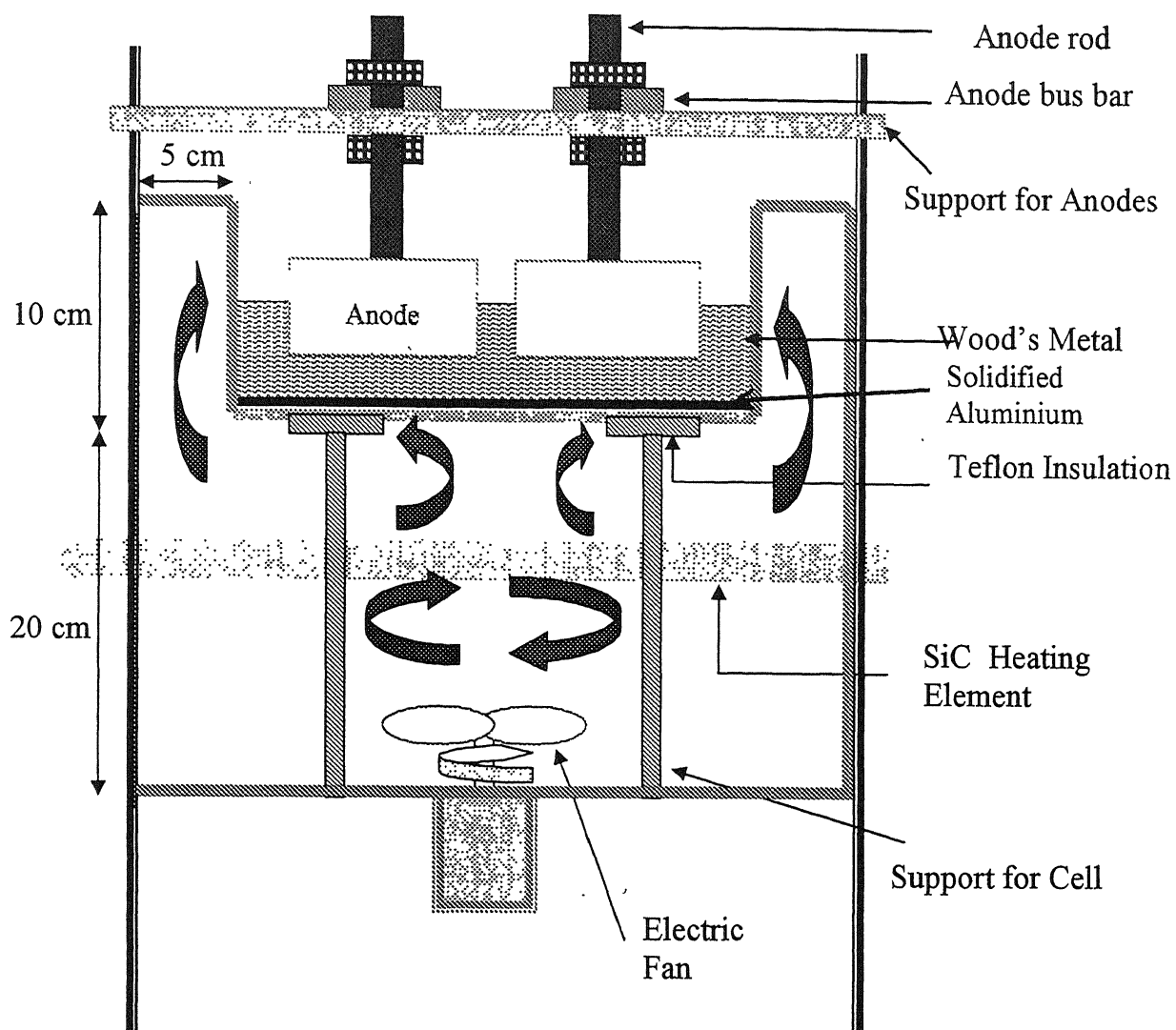
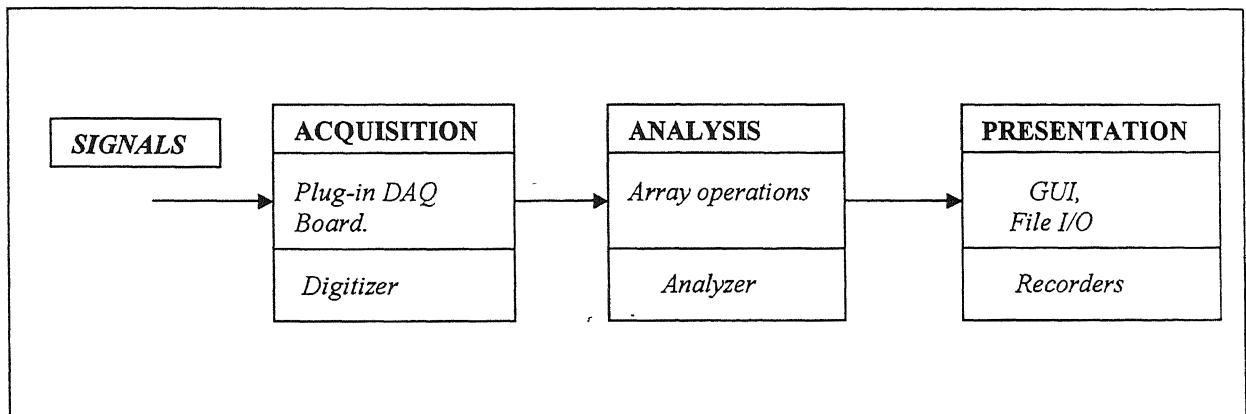


Fig. 3.3 Heating arrangements of the simulated low temperature cell.

**(v) Data Acquisition System:** The principal task of the DAQ system is to capture the physical signals from the measuring instrument and to convert these into conditioned electrical signals. These electrical signals are fed to the data acquisition board which digitizes the signal. The software controls the DAQ system by acquiring the raw data, analyzing it, presenting and storing the data.

**Flow diagram of the Data Acquisition System:**



**Specifications of the DAQ system:** The emf developed in the two pairs of the probe is measured using two Keithley 182 sensitive digital voltmeters of Keithley Instruments Incorporation, Ohio, USA.

**DAQ board and accessories:** The DAQ board used for interfacing is National instruments pci-6024E, which is a multifunction device having 16 channels (eight differential) of analog input, two channels of analog output, a 68 pin connector, and 8 lines of digital I/O. It is a resolution of 12 bits and a maximum sampling rate of 200 kHz. A 68-pin cable and a connector block CB68lp for pci 6024e is used for connecting the instrument to the DAQ board.

**Software:** National instruments labVIEW 6i is the software used. LabVIEW (Laboratory Virtual Instrument Engineering Workbench) is a development environment based on graphical programming, having user friendly GUI and powerful analysis VIs. This software was used to write the VI (virtual instrument) for acquiring the data.

## 3.2 CALIBRATION OF VELOCITY PROBE

**3.2.1 PRINCIPLE OF VELOCITY PROBE:** The principle behind the velocity probe is that a conductor moving within a magnetic field generates an electric field, i.e. a voltage gradient. According to the faradays law of electromagnetic induction, the induced emf is equal to the rate of change of magnetic flux:

$e = \int E \cdot dl$  where  $E$  is induced electric field and the emf induced by a conductor moving the induced magnetic field is given  $e_m = (B \cdot l) \times V$  where  $V$  is the velocity,  $B$  is the magnetic field produced by the permanent magnet in the probe, and  $l$  is the separation between the two tips of the probe.

**3.2.2 DESIGN OF VELOCITY PROBE:** The probe is in-house fabricated and is based on the principle of velocity probe used by Ricou and Vives successfully. A permanent magnet of 3 mm diameter is used for the source of magnetic field. Four single strand wires of diameter 1.5mm were placed around the equatorial plane of the permanent magnet for sensing the voltage gradient. A teflon cylinder was used to keep the four wires along with the permanent magnet firmly in place. To give the probe sufficient mechanical strength and for better maneuvering of the probe during experiments it was surrounded by a copper tube. It also prevents the interception of the external magnetic field created by various electrical appliances viz. variac. The two pairs of wires used to measure two velocity components respectively make the probe two dimensional. After several modifications in the Ricou and Vives probe the final design of the velocity probe was arrived at. A schematic diagram of the velocity probe is shown in Fig.3.4.

**3.2.3 DESIGN OF CALIBRATION SET UP:** Initially it was planned to use rack and pinion mechanism for calibration of velocity probe. The principle involved was to linearly move the velocity probe in molten pool of simulated cell. The rack and pinion arrangement is shown in Fig 3.5. Though, it was able to move the probe uniformly but

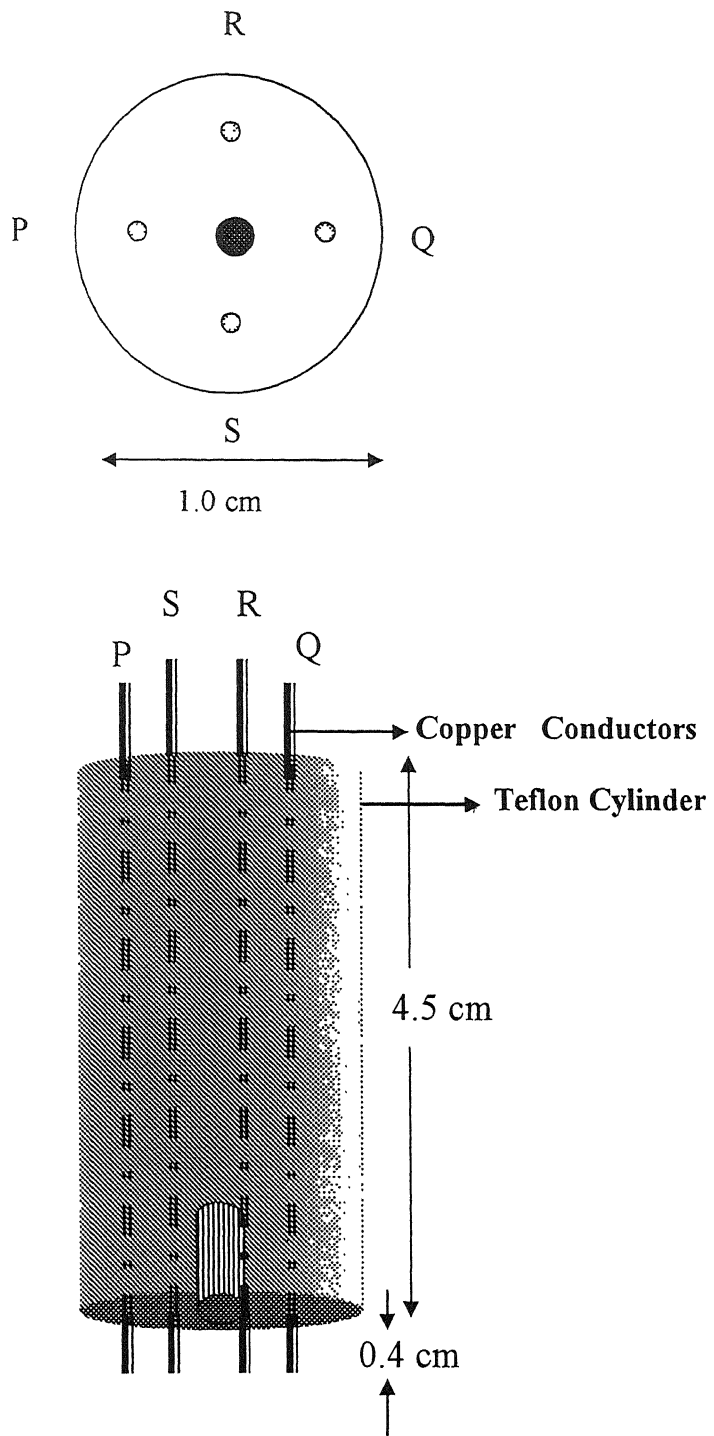


Fig 3.4 Schematic diagram of the Velocity probe used.

the nanovoltmeter reading could not be stabilized as prolonged movement of probe was required which our set up could not provide. So it was planned to go for another calibration setup which is based on the principle of continuous rotation of a turntable pot containing a pool of Wood's metal surrounded by a water jacket mounted on a platform driven by an electric motor. The purpose of keeping the water jacket was to continuously heat the Wood's metal uniformly through out by putting immersion water heaters placed in the water jacket. The power supply to the motor was regulated using a variac to achieve lower revolutions of the pot. The rpm could readily be measured by stopwatch or eye. It was difficult to rotate the calibration pot at lower rpms by mean of simple variac controlled motor. So later it was decided to step down the high rpm of the motor by employing gear and pulley arrangement. The details of the various components of the calibration setup along the gears and pulley arrangement are shown in Fig.3.6. The various gears those were used in the set up to decrease down the rotation speed of the pot generated a lot of frictional disturbances due to the mechanical contact of the gears. The problem was sorted out when some of the experiments were performed under this condition, and it was impossible to obtain a stable nanovoltmeter reading. The transmission gear connected to the motor shaft for transmitting the rotation of the shaft to the reduction gears was found to be the major source of vibration and was finally replaced by a belt drive arrangement. The still left out vibrations were minimized by putting padding under all the components of the set up.

### 3.2.4 CALIBRATION OF VELOCITY PROBE:

**Principle:** A current carrying conductor moving in a magnetic field is given by an equation  $\vec{J} = \sigma(\vec{E} + \vec{V} \times \vec{B})$

where  $\vec{J}$  is current density,  $\sigma$  is conductivity of the conductor,  $\vec{E}$  is emf,  $\vec{V}$  is velocity of the conductor, and  $\vec{B}$  is magnetic field. Here the conductor is Wood's metal, which is moving with velocity  $\vec{V}$  in the constant magnetic field of permanent magnet  $\vec{B}$ . So the emf induced is directly proportional to the velocity with which the conductor is moving. Apart from the emf developed due to motion of the melt the probe senses some more emfs. The emf sensed may be partly also due instrument geometry termed as instrument

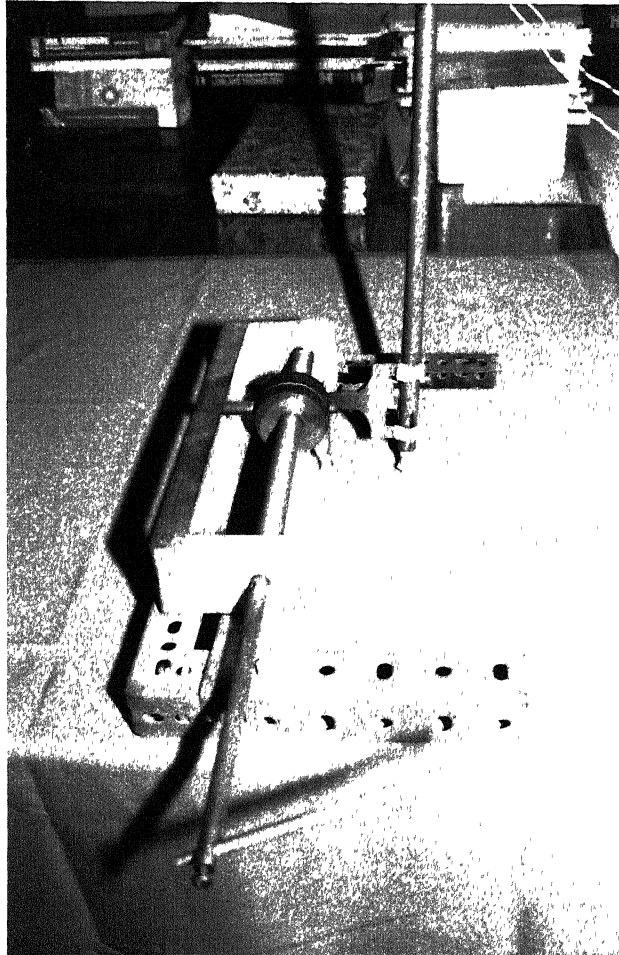


Fig. 3.5 Rack and Pinion arrangement for calibration of velocity probe.



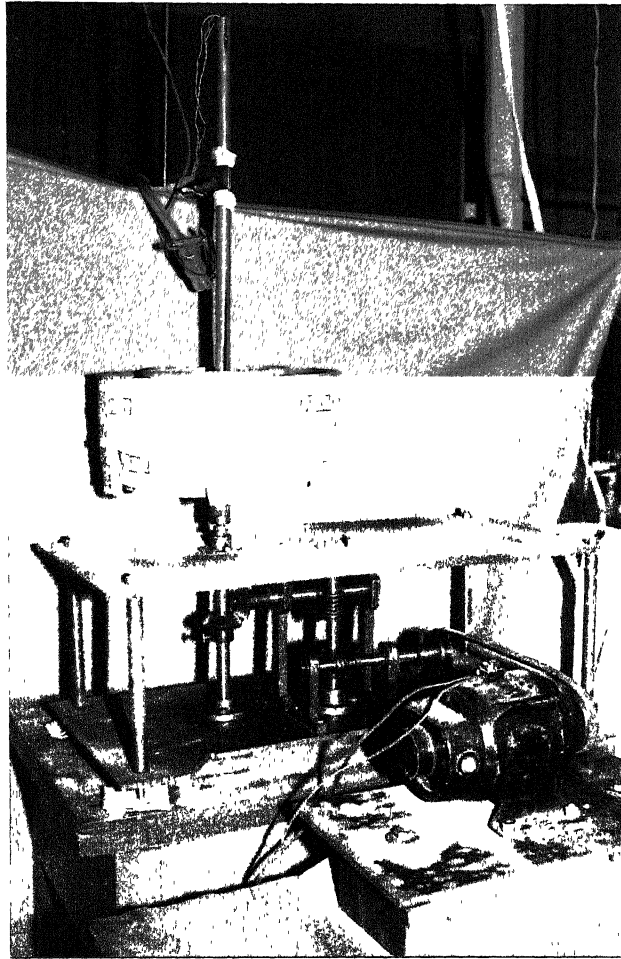


Fig. 3.6 Calibration set up for calibration of the probe.

constant, temperature gradient in the melt, and thermal convection effect. Thus the net emf between the tips is a sum of all the emfs

$e_{net} = e_{actual} + e_{thermal} + e_{convection} + e_{instruments}$  where  $e_{actual}$  is the induced emf due to velocity  $e_{thermal}$  is the emf due to thermal gradient in the melt,  $e_{convection}$  is the emf due to convection, and  $e_{instruments}$  is the emf due to instrument constant. Care was taken to circumvent the effect of emf components due to temperature gradient, instrument constant on our reading during calibration. It is assumed that the flow due to convection is negligible.

#### **Procedure:**

The calibration device was heated by means of heaters placed symmetrically. The probe having 3 mm permanent magnet was mounted in a fixed position so that it is immersed in Wood's metal at a measured distance from the axis of the turntable. On placing the probe in a moving conductive fluid, the motion of the liquid through the field of the permanent magnet induces an electric field, which was sensed by two digital nanovoltmeters connected to four cables. The motor was given regulated power supply by means of variac. The rotation of the turntable was maintained with a very low rpm of 1-2, which was readily measurable by eye. Since the probe is considered to exert negligible drag on Wood's metal, the tangential velocity of the melt just beneath the probe tip, sensed by the probe tips can be obtained by  $2\pi$  multiplied by the distance from the probe to turntable axis multiplied by the rotation speed.

$$\text{Velocity just beneath the probe tips} = 2\pi r \left( \frac{N}{60} \right) \text{ cm/sec.}$$

where  $r$  is the distance from the center of rotation axis to the probe position, and  $N$  is the speed of the turntable in rpm. Emf induced was measured with the help of Keithley 182 sensitive digital voltmeter. The respective channel signals were acquired by means of interfacing the digital nanovoltmeter along with a personal computer with the help of labVIEW software. During the calibration of velocity probe the water level in the calibration pot was maintained constant so as to ensure a constant rotational speed by means of regulated water tap. Temperature of the calibration pot was maintained at a constant value by running it for several hours with a constant water input to the pot. The nanovoltmeter reading was acquired both when the pot was in a still condition and while

it was rotating. The emf sensed during the process included the emf contribution from the cell constant. This contribution of instrument constant was taken care by deducting the emf at still condition from the emf sensed while the pot was moving. The two pairs of the velocity probe were calibrated separately putting them so as to pass the molten Wood's metal moving at a particular speed perpendicular to the sensing wire tips. The tangential velocity under the probe tip was regulated by either varying the position of the probe radially inward and outward for a particular rpm or by controlling the rpm of the pot keeping the probe at a fixed point. The experiments were first done in varying the radial positions of the velocity probe for a particular rpm. Then rpm was varied and to check the repeatability of the calibration experiment the probe was placed in positions calculated from the relation below

$2\pi N_1 r_1 = 2\pi N_2 r_2$  where  $N_1$  and  $N_2$  are the number of revolutions corresponding to the radial positions of the probe at  $r_1$  and  $r_2$  respectively. The corresponding emf sensed was acquired. Then the repeatability of the calibration of the two channels was done for four rpms. The calibration plot was plotted the velocity versus the nanovoltmeter reading. The calibration plots of the two pairs (two channels) of probe tip are shown in Fig. 3.7(a) and 3.7(b). These calibration plots were used to measure the velocity in laboratory scale simulated cell.

### 3.3 EXPERIMENTAL PROCEDURE

**3.3.1 START UP:** Before starting the experiment the heating was done with regulated power supply to the heating element. Simultaneously the nanovoltmeter was switched on. It takes about 4-5 hours for Wood's metal to melt. The temperature of the cell was closely maintained with the help of a thermocouple. Current was passed into the cell. The velocity Probe was placed in the cell at a desired location and sufficient time was provided for the nanovoltmeter reading to stabilize. Initially nanovoltmeter reading was observed to be fluctuating. The few shortcomings were sorted out and there were measures taken to make it stable.

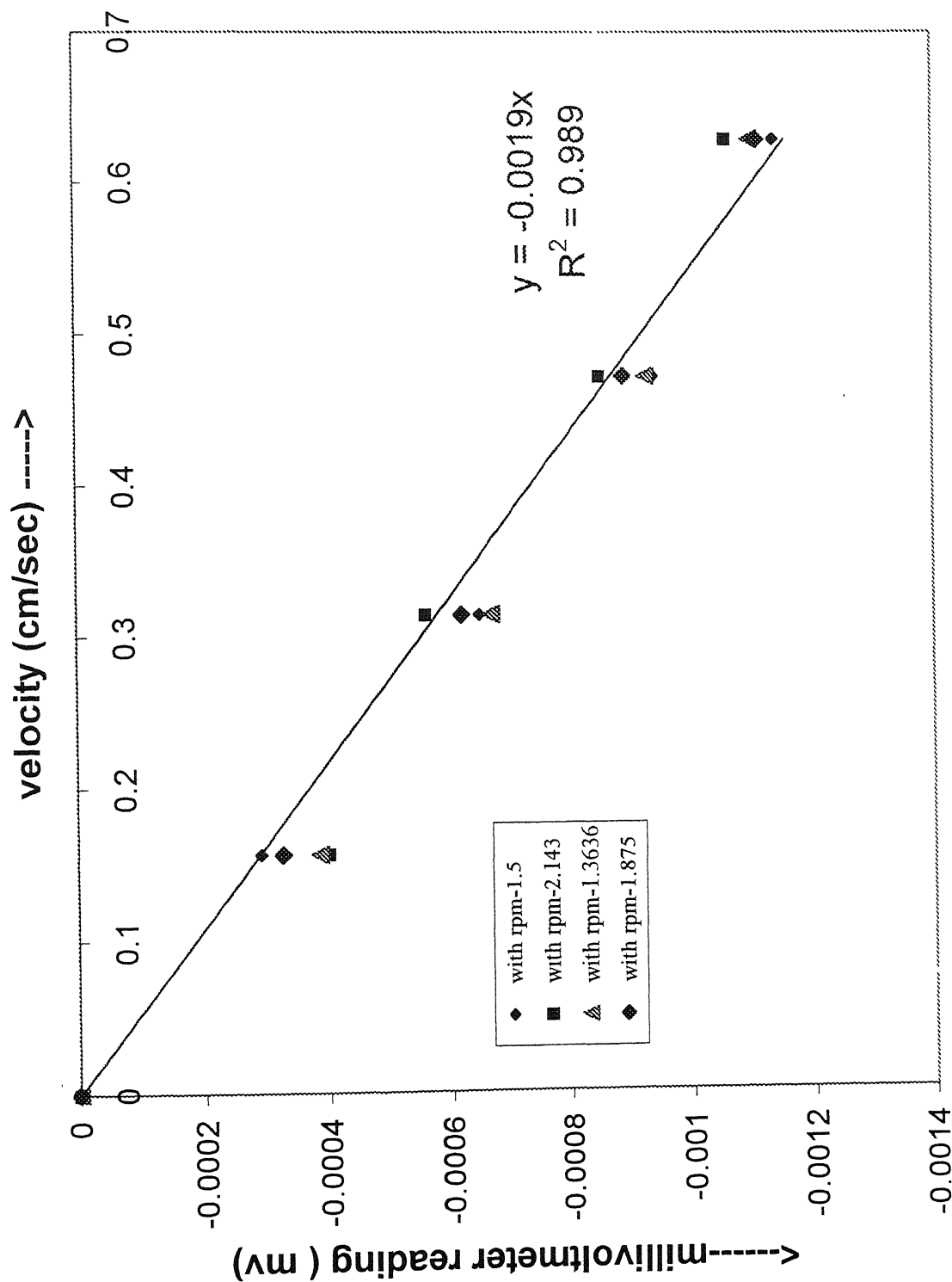


Fig. 3.7(a) Calibration plot of 0<sup>th</sup> channel (R-S pair) of the velocity probe.

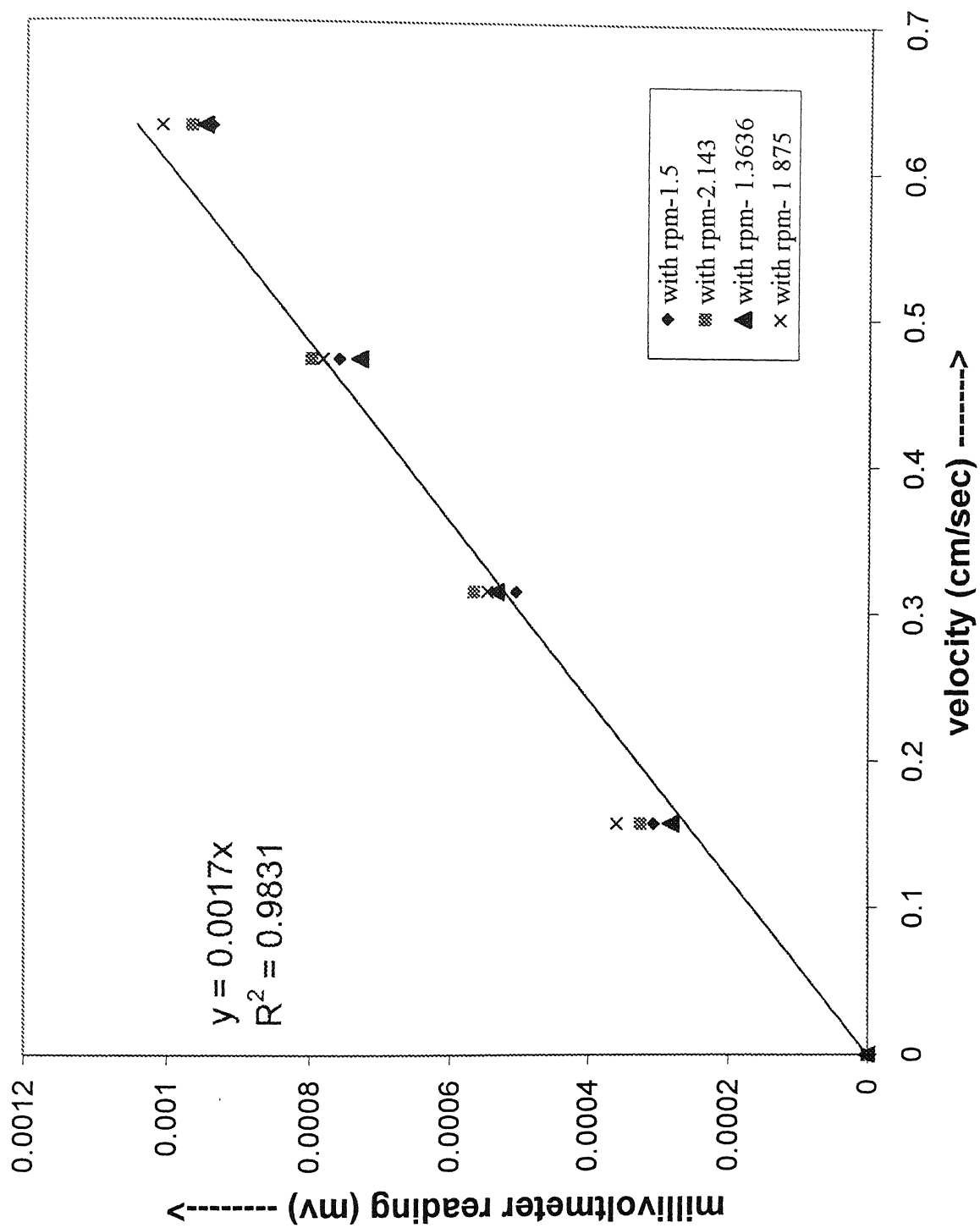


Fig. 3.7(b) Calibration plot of 1<sup>st</sup> channel (P-Q pair) of the velocity probe

**3.3.2 MEASURES FOR STABLE READING:** The following steps were taken to make the nanovoltmeter reading stable.

(i) Initially the probe was fabricated with single strand wires of diameter 1.5mm. These wires were having very high resistance loss as compared to the emf of nano volt range sensed during experiments. So it was decided to replace these wires by single strand hook up cables of diameter 0.15 mm, which has a very low resistance loss.

(ii) The wire coming from probe was connected to the nanovoltmeter connector by means of mate contact. There was a lot of fluctuation due to interception of the external magnetic field. This problem was sorted out and then the mate contact was replaced by direct soldering between the connector and the hook up cables. This made the reading stable.

(iii) The earth's magnetic meridian affects the stability of the reading. So the nanovoltmeter had to be placed properly to have a better stability of the signals. Oscilloscope was placed and the reading was made stable by making adjustment with respect to magnetic meridian. Then the oscilloscope was replaced with the nanovoltmeter.

**3.3.3 REPRODUCIBILITY EXPERIMENTS:** The table below shows the reproducibility of velocity measurement experiments. The nanovoltmeter readings were taken at four different locations for three different days under similar conditions. The results were found to be consistent within 20% of deviations.

Table 2. Reproducibility of velocity measurement in four different locations in three different days.

DVM Reading (m.volt)	Location 1		Location 2		Location 3		Location 4	
	P-Q	R-S	P-Q	R-S	P-Q	R-S	P-Q	R-S
Day 1	-0.00025	4.02E-5	-0.00037	-0.00019	0.000231	0.000439	6.34E-5	-0.00047
Day 2	-0.00029	4.34E-5	-0.00035	-0.00023	0.000257	0.000483	6.97E-5	-0.00044
Day 3	-0.000278	3.95E-5	-0.000395	-0.000242	0.000191	0.000403	7.42E-5	-0.00039

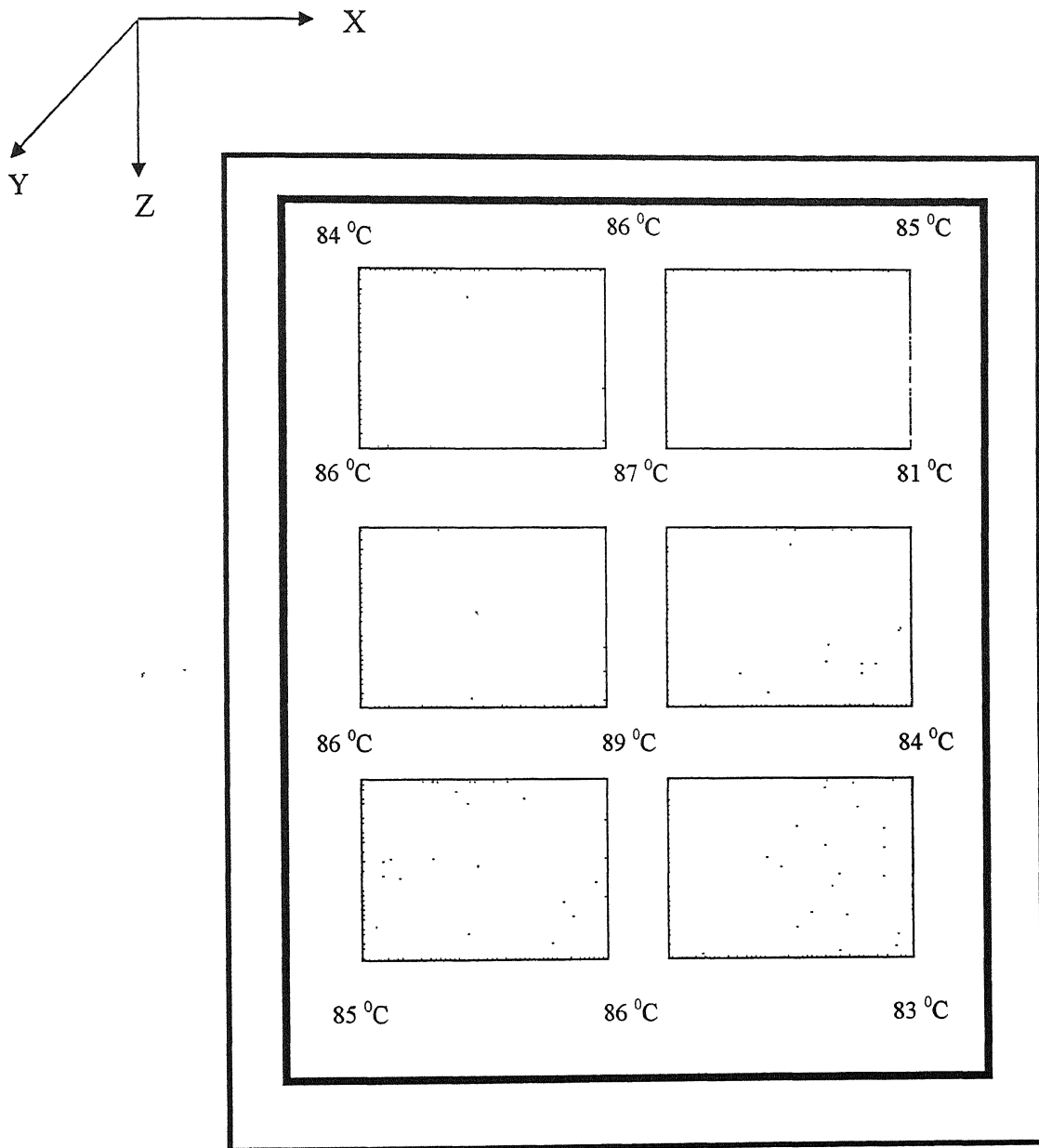


Fig. 3.8 Variation of temperature in the simulated cell.

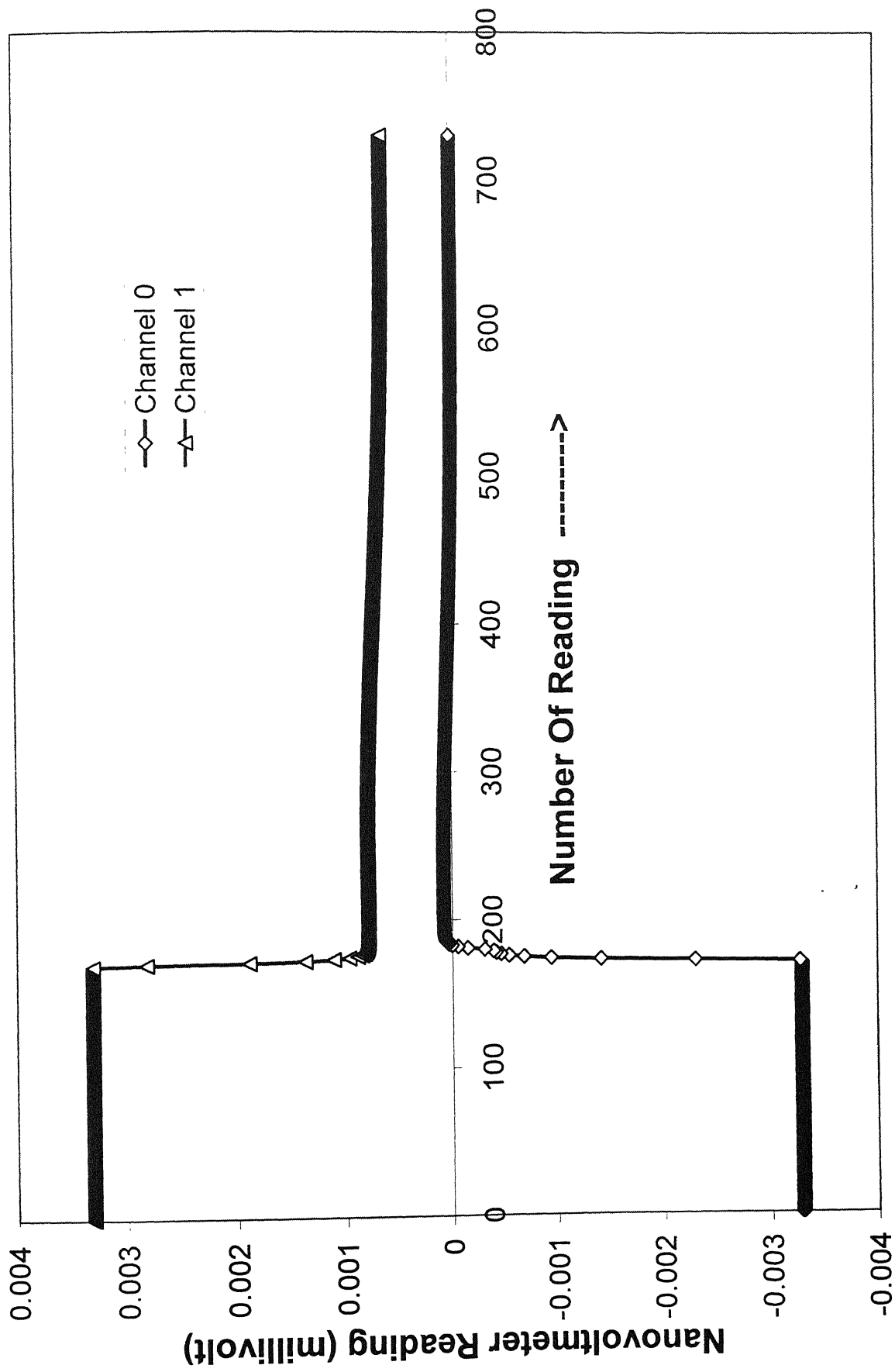


Fig. 3.9 Current Interruption Technique using the Data Acquisition System



**3.3.4 VELOCITY MEASUREMENTS:** The current from the DC supply passes into the cell. The uniform distribution of the current among the Busbars, anodes, and collector bars were ensured by measuring the current by the help of True RMS Clamp meter. Although the temperature was tried to maintain constant maintained constant at 85 °C throughout but there was a variation of temperature in a range of  $\pm 5$  °C. A typical temperature variation in the cell is shown in Fig. 3.8. After the nanovoltmeter reading gets stabilized, the probe was put at desired locations. The probe suffers from the disadvantage that it senses the electric field imposed on the model by the power supply as well as that induced due to flow in the Wood's melt. The former field is much larger than the latter. The problem of the emf sensed due to direct passage of electric current through the melt was circumvented by following current interruption technique. The Data Acquisition Card used in the set up enabled us to go for the process of current interruption technique. It also ensured acquiring reasonably accurate data sets. In the current interruption technique it is assumed once the external current is switched off the emf sensed by the probe is essentially the emf generated due to fluid flow in the vicinity of the probe tip. Hence, it is directly related to the melt velocity. It is evident from Fig. 3.9 that as soon as the current was made off, the component of emf due to the passage of current vanished within a fraction of seconds. Preliminary experiments were performed with varying time intervals so as to have an idea about the time it takes for the melt to achieve a steady state velocity. For a particular probe position, sufficient time was allowed for the nanovoltmeter reading to get stabilized. Such measurements were made at various probe positions. Periodic checks were made to verify the uniformity of the current distribution of the in the simulated cell components. It was very difficult to achieve a uniformity of current distribution, but utmost care was taken to make it as uniform as possible.

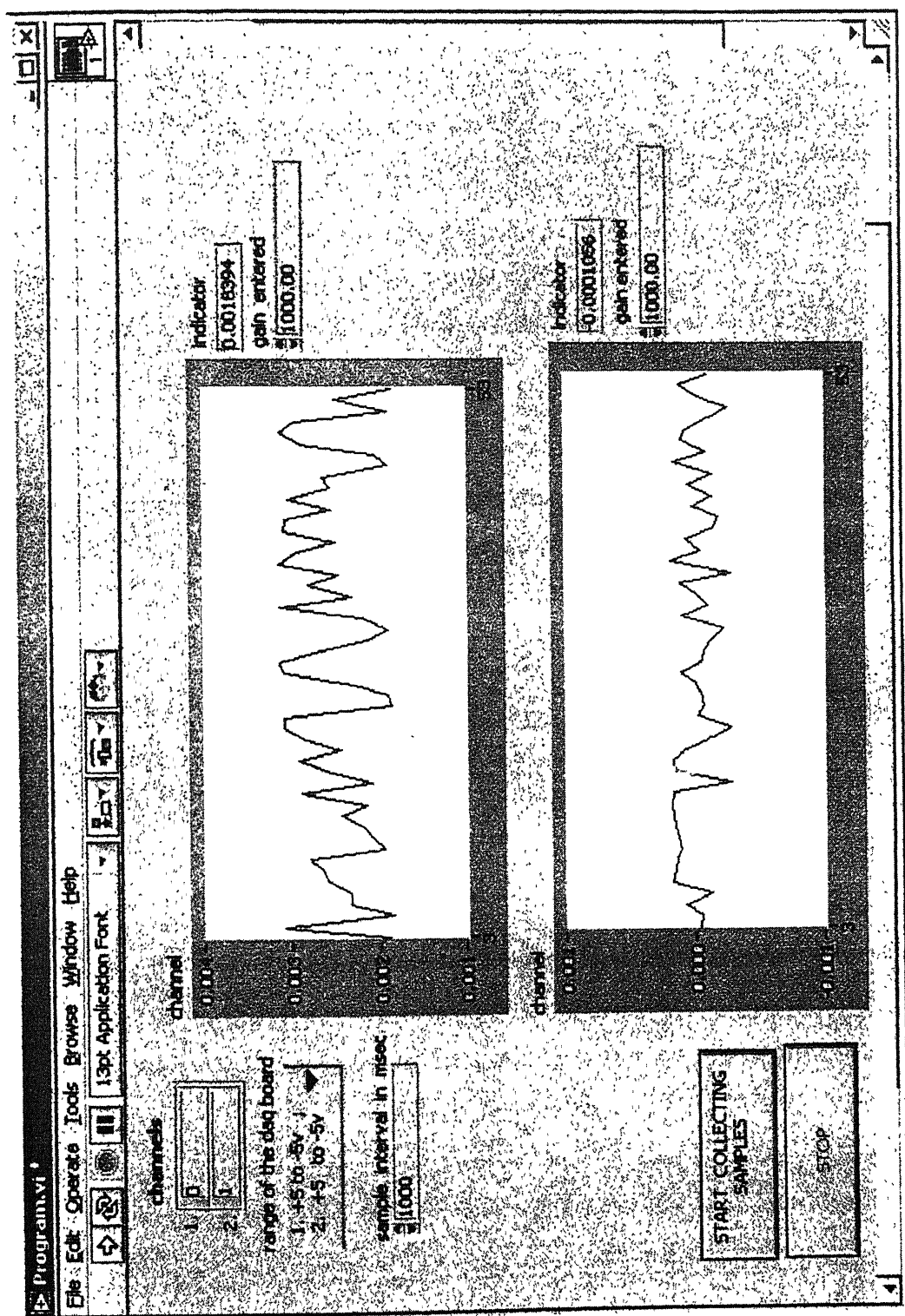


Fig. 3.10 The program window of Data Acquisition showing the nanovoltmeter reading of the two channels.

## CHAPTER 4

### RESULT AND DISCUSSION

#### 4.1 MEASURED VELOCITY DISTRIBUTION

Measurements of velocity were done keeping the following parameters constant:

- (i) The anodes were kept at a fixed distance from the walls i. e. 2 cm from the facing wall and 3 cm from the side walls (refer Fig.3.1).
- (ii) Total depth of Wood's metal was maintained constant at 4.0 cm.
- (iii) End riser design was employed for all the experiments.
- (iv) The temperature was maintained constant at  $85 \pm 5$  °C.

Process variables and their ranges investigated during various experiments are summarized below.

Table 3. Process variables and their ranges investigated.

Sr. No.	Variables	Ranges/ Type
1.	Total current input	0-500 Amps in steps of 100 amps.
2.	Current density	0.5, 0.75, and 1.0 amp/cm <sup>2</sup> .
3.	Depth of measurement	0.6 cm, 1.25 cm (mid height), and 3.0 cm.
4.	Anode Cathode Distance	2.5 cm, 2.0 cm, and 1.5 cm.
5.	Shielding conditions	(i) Cell wall not shielded. (ii) Cell wall shielded by non-conducting strips.

The flow of current, the basic busbar and collector bar connections, the reference axes along with the points where velocities were measured is shown in Fig. 4.1. The measured velocities are presented in pictorial form with the corresponding points marked within the cell. The exposition starts with a “base” case of an undisturbed cell.

**4.1.1 BASE CASE:** The velocity vectors in the base case are depicted in Fig. 4.2. The model is seen from above where the rectangular blocks represent anodes. The vectors show the direction of the velocity and the arrow lengths are proportional to velocity.



Current input = 576 Amps

Current Density =  $1.0 \text{ A/cm}^2$

ACD = 2.5 cm

Depth of measurement = 3.4 cm

0.4 cm/sec

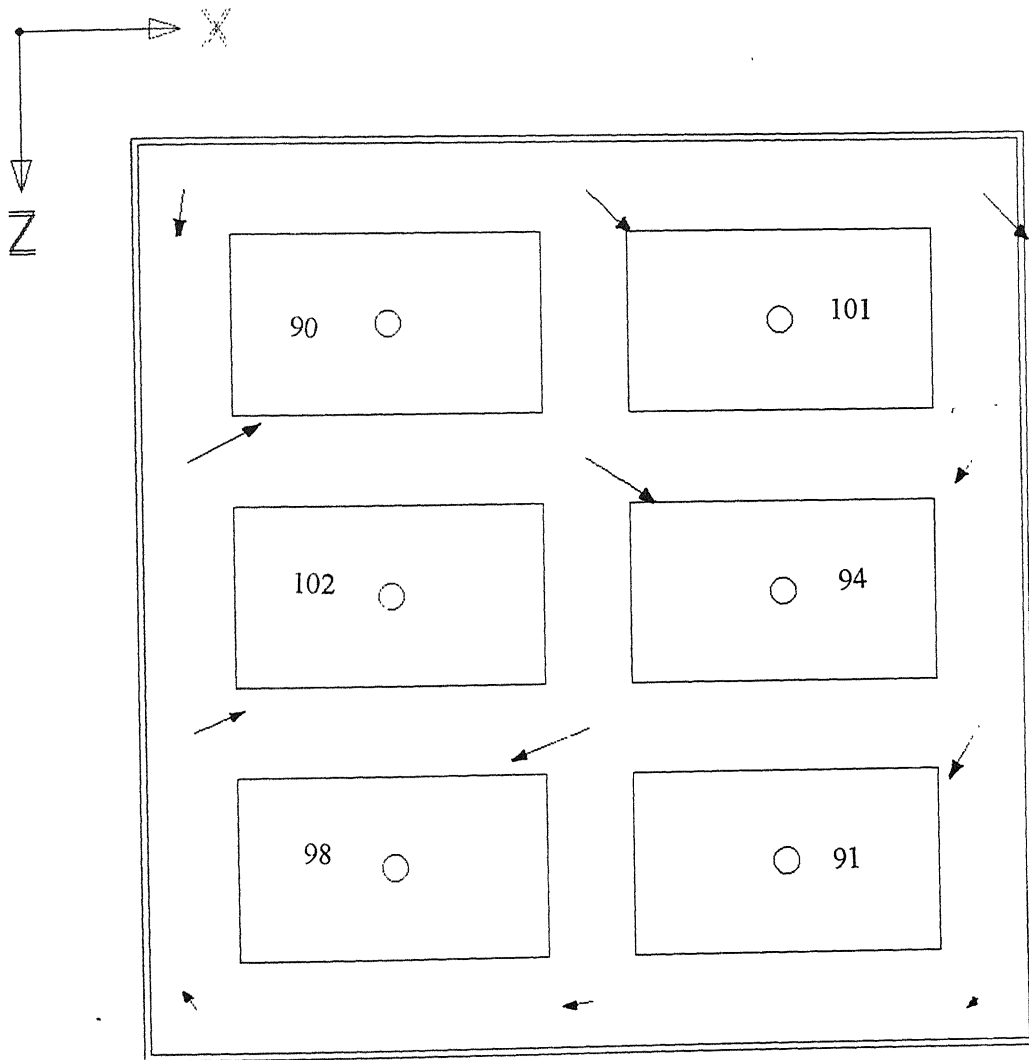
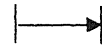


Fig. 4.2 Measured velocity distribution for “base” case in X-Z plane ( $Y=1.6 \text{ cm}$ ).

Current input = 528 A

Current Density =  $0.916 \text{ A/cm}^2$

ACD = 2.5 cm

Depth of measurement = 3.4 cm

→ Resultant horizontal component

→ Vertical component

2 Gauss

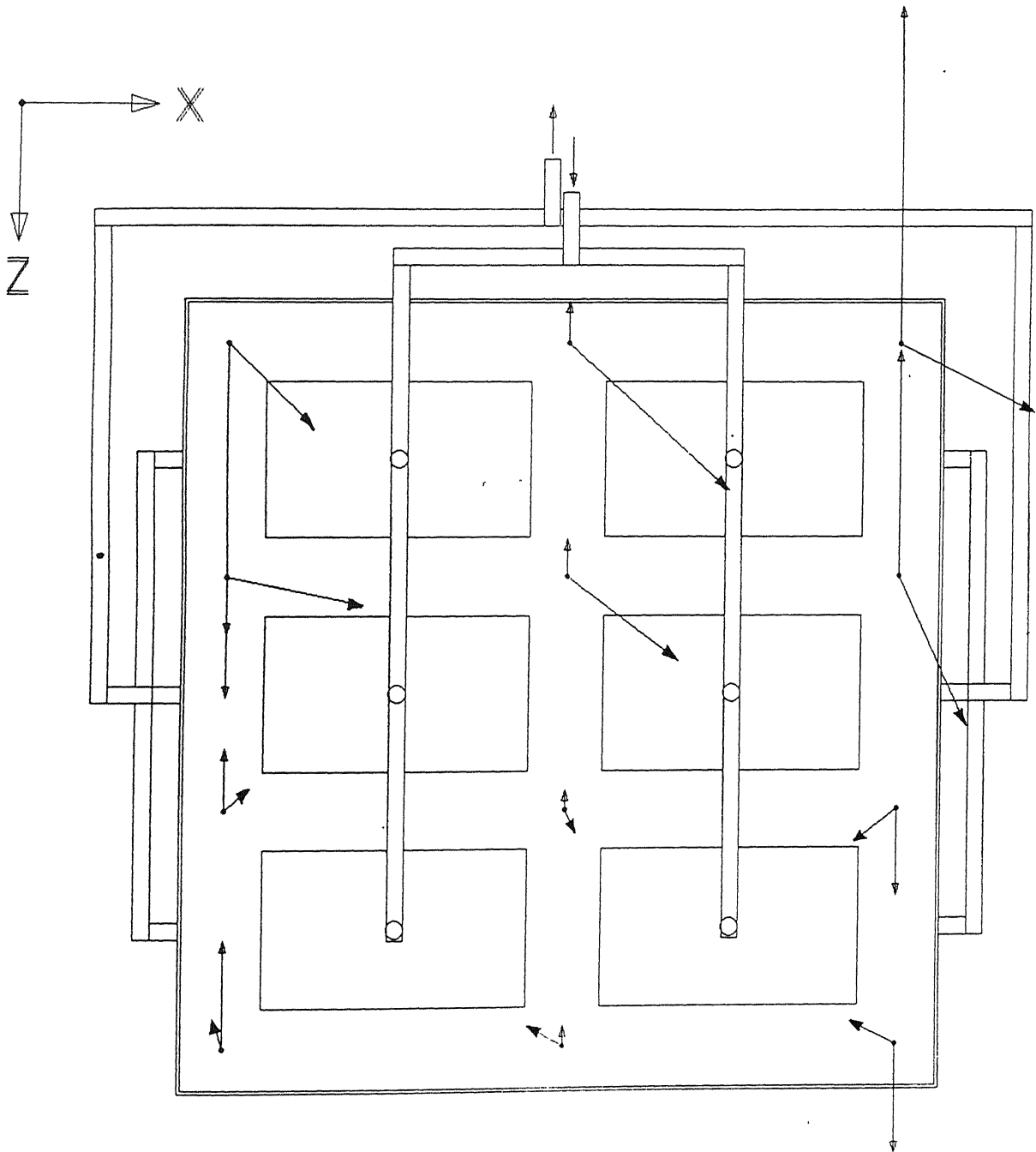


Fig. 4.3 Measured magnetic field distribution when input current is 528 A [7].

The distribution of current through the anodes are given by the numbers written on them. The nature of the velocity profile will be explained with the help of the direction of the electromagnetic force. Beneath each anode, the current flow in the Wood's metal is predominantly downward direction, as it is in the electrolyte of real cells. However, significant amount of current in the model flows through the sidewalls too as evident from the findings stated in chapter 2 (Fig. 2.2.). Both the current components such as horizontal current ( $J_{xz}$ ) and vertical current ( $J_y$ ) interacts with the magnetic field. The forces are the cross product of the current density vector and the magnetic field vector.

$$\vec{F} = \vec{J} \times \vec{B}$$

where  $\vec{F}$  is the electromagnetic body force;

$\vec{J}$  is the current density; and

$\vec{B}$  is the magnetic field.

Consequently on the horizontal plane the electromagnetic force that would be responsible for driving the melt would result from the interaction of the horizontal current ( $J_{xz}$ ) with the vertical magnetic field ( $B_y$ ) and vertical current ( $J_y$ ) with the horizontal magnetic field ( $B_{xz}$ ). The magnetic field at the those points in question measured by Bhunia [7] is shown in Fig. 4.3. The convention followed in Fig. 4.3 is that the open arrow pointing downward is pointing downward into the plane of paper and the arrow pointing upward is coming out of the plane of the paper. Figure 2.2 and 4.3 shows the measured current density and magnetic field distribution [7]. Figure 4.4 shows the direction of the electromagnetic force at different points. Flow direction at each is proportional to its electromagnetic force. The current flows predominantly downward and it interacts with the horizontal magnetic field to generate electromagnetic force. So this predominant clockwise electromagnetic force drives the melt and results a clockwise loop and apart from this there is an anticlockwise loop found to be formed at the upper left corner of the cell. This is attributed to the electromagnetic force at these points, which are predominantly anticlockwise.

$C, c$  – Clockwise     $A, a$  – Anticlockwise  
 $C, A$  – Electromagnetic force due to  $(J_y \times B_{xz})$   
 $c, a$  – Electromagnetic force due to  $(J_{xz} \times B_y)$

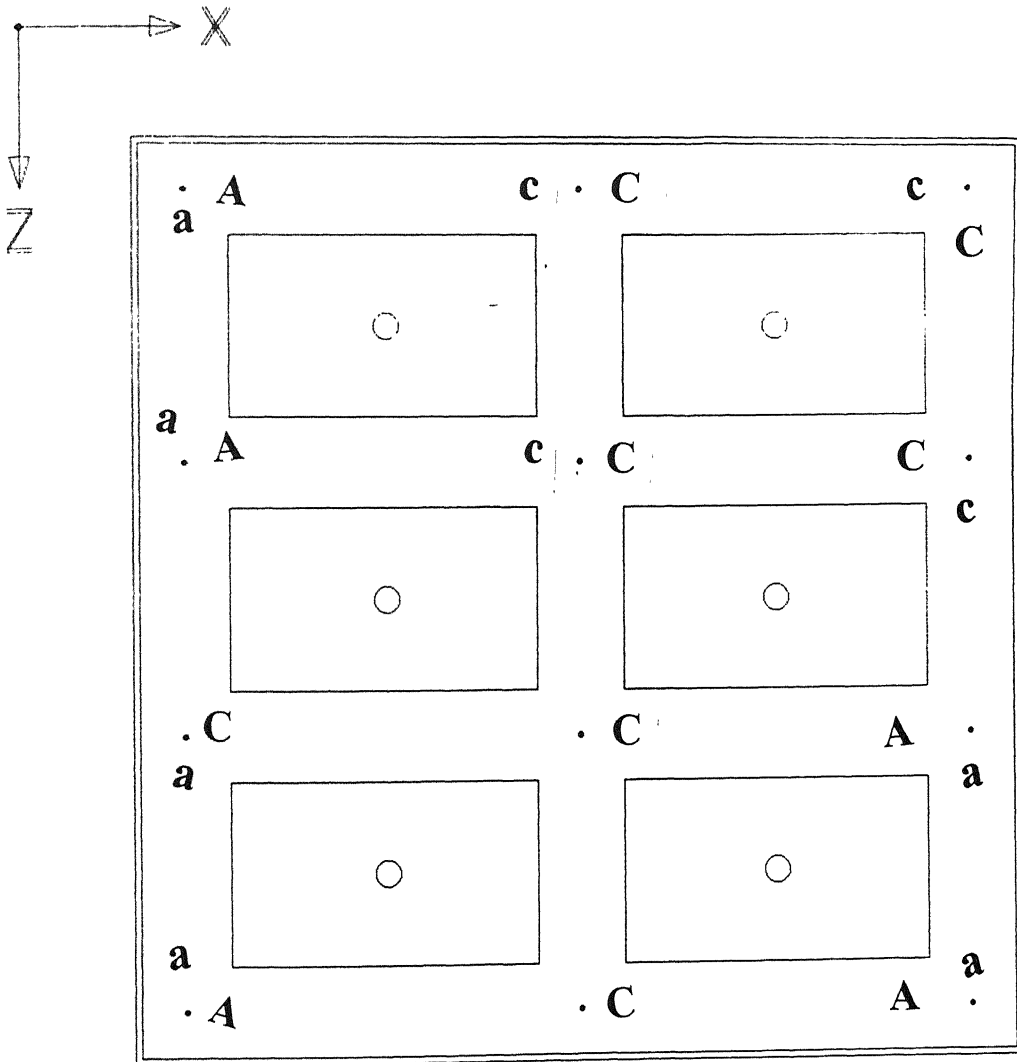


Fig. 4.4 Schematic drawing of the direction of Electromagnetic force at desired points derived from the measured magnetic field distribution and current density distribution.



Current input = 576 Amps

Current Density =  $1.0 \text{ A/cm}^2$

ACD = 2.5 cm

Depth of measurement = 1.5 cm

0.4 cm/sec

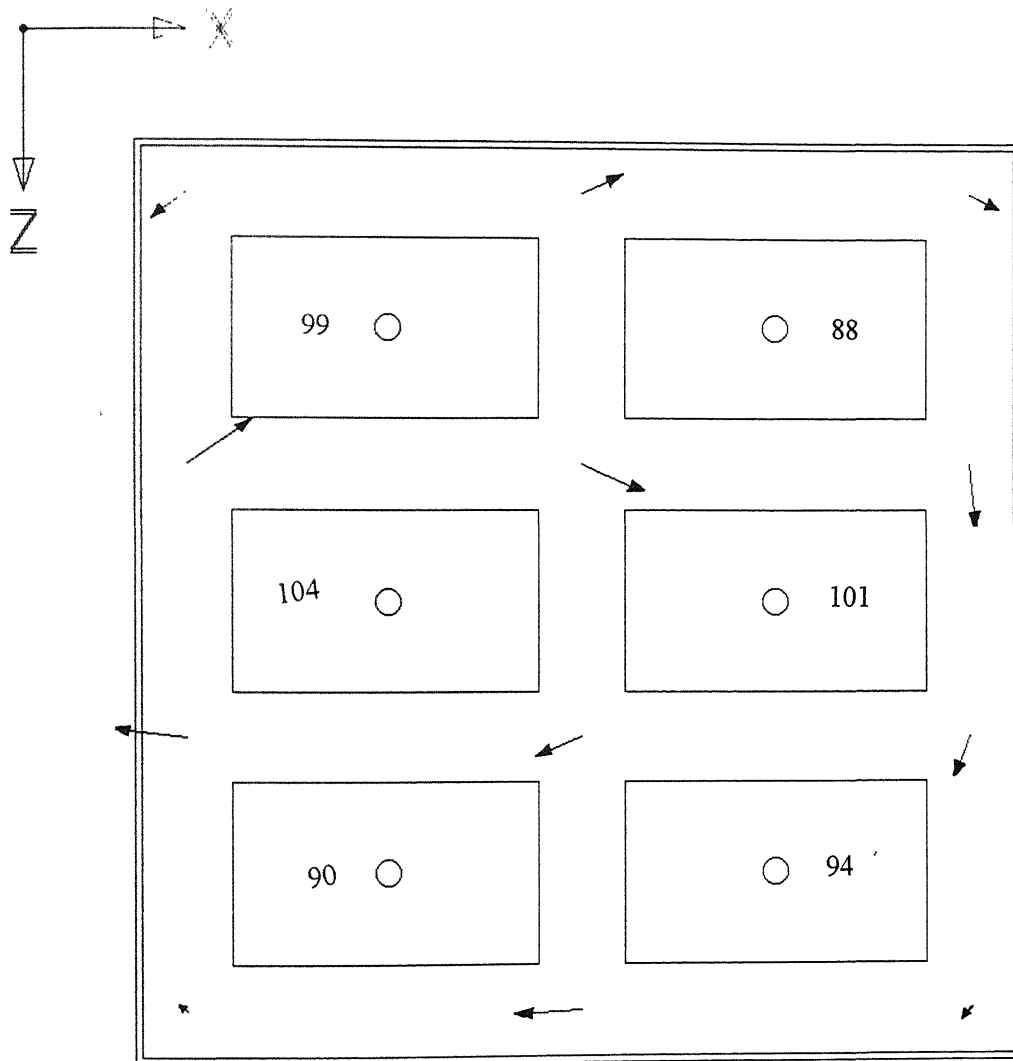


Fig. 4.5 (a) Measured velocity field at a depth of 1.5 cm of Wood's metal. ( $Y = 3.5 \text{ cm}$ ).

Current input = 576 A

Current Density =  $1.0 \text{ A/cm}^2$

ACD = 2.5 cm

Depth of measurement = 2.75 cm

0.4 cm/sec

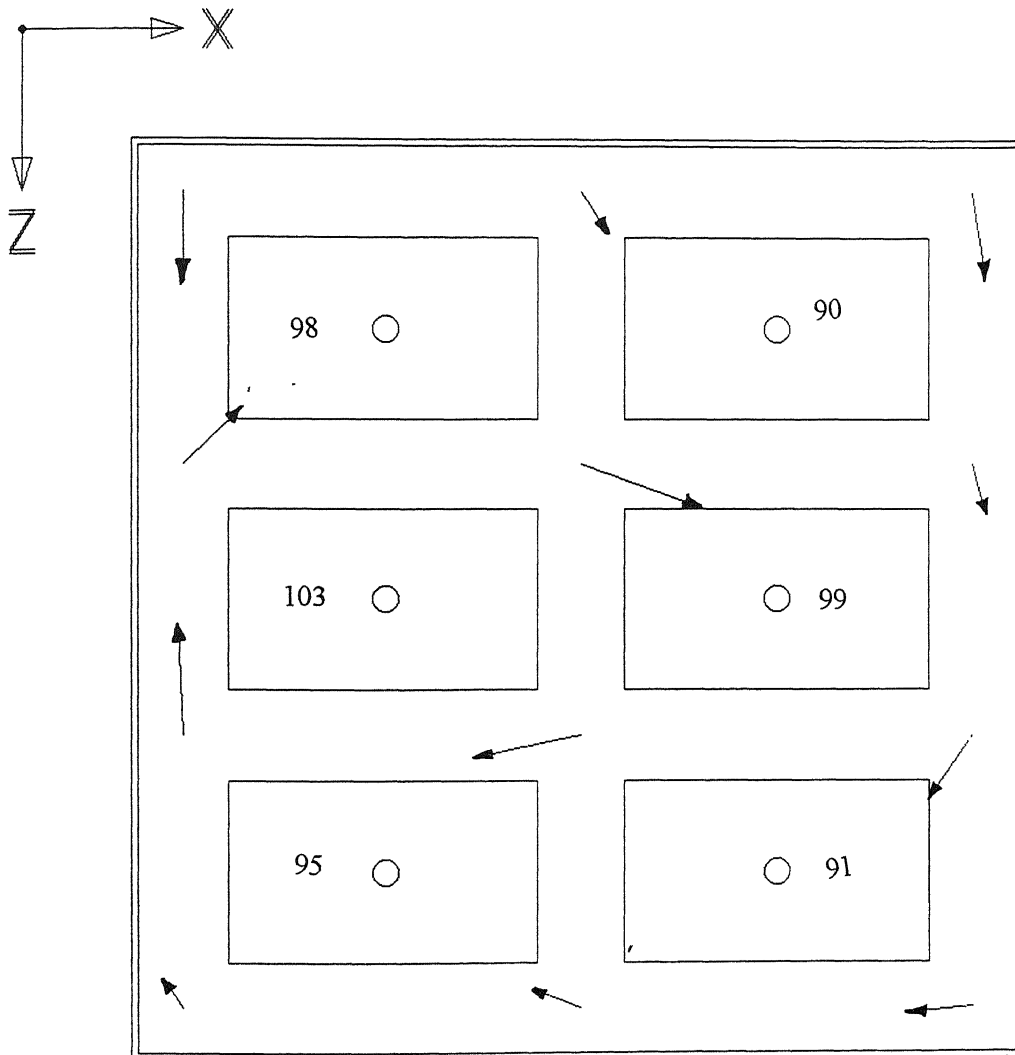


Fig. 4.5 (b) Measured velocity field at a depth of 2.75 cm of Wood's metal ( $Y = 2.25 \text{ cm}$ ).

**4.1.1.1 Effect of depth:** The depth of the probe was varied without disturbing the probe positions and velocity measurements were done. Figure 4.5 (a), 4.5 (b), and 4.2 shows the velocity vectors measured at different depths of 1.5 cm, 2.75 cm, and 3.4 cm from the top surface of the Wood's metal respectively keeping other parameters like ACD and current input constant. It has been observed that the velocity measured at the mid height of anode cathode gap (depth of 2.75 cm) is more as compared to the velocity at the bottom and the top of the molten Wood's metal. However the velocity measured at a depth of 1.5 cm is found to be less than at a depth of 3.4 cm. This is explained on the basis that the velocity of the melt depends on the balance between (i) electromagnetic force, and (ii) drag forces. The drags offered by the bottom of the anode and the cell walls in the case of depth of 1.5 cm is more as compared to the drag offered by the solidified aluminium bottom and hence results lower velocity. The effect of drag at the mid height of melt is lower, so the velocity measured at this plane (Fig. 4.5(b)) is higher than the other two planes. Here it is assumed that the magnetic field is same at different depth of Wood's metal. This approximation is reasonable since the depth of the liquid is small as compared to the cell and busbar dimensions. The velocity pattern remains more or less same for all the cases except few points as the direction of the force remains similar in nature as described in Fig. 4.4.

#### 4.1.2 EFFECT OF TOTAL INPUT CURRENT

Measurements of velocity have been carried out by varying the input current from 0 to 500 A with step size of 100 A. This was done in some of the representative points (1, 2, and 4 as shown in Fig. 4.1). Velocity was plotted against the square of the current input. Fig. 4.6 shows the plot of all the three points follows linear trend i.e. the velocity at each point is directly proportional to the square of the current input. This is due to the fact that the velocity is proportional to the electromagnetic force.

$\vec{F} \propto (\vec{J} \times \vec{B})$  where  $\vec{J}$  is the current density;  $\vec{J} \propto I$  where  $I$  is the total current.

According to Biot Savart's law  $\vec{B} \propto I$ ;

Hence  $\vec{F} \propto I^2$

The melt velocity is proportional to the electromagnetic driving force hence varies linearly with square of the current. Figure 4.6 shows that this is indeed the case.

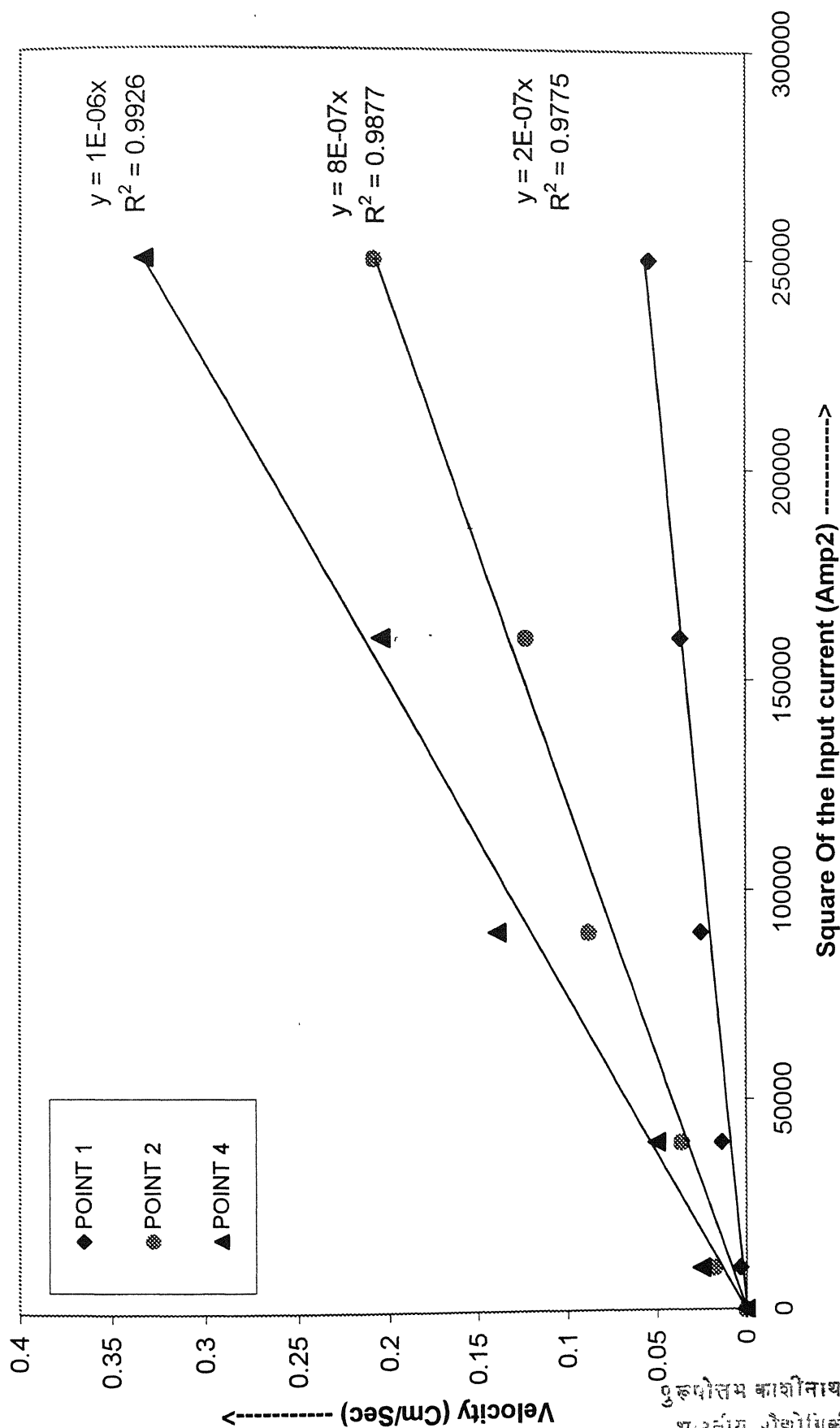


Fig. 4.6 The relationship between velocity and square of current input at various locations.

Current input = 432 A

Current Density =  $0.75 \text{ A/cm}^2$

ACD = 2.5 cm

Depth of measurement = 3.4 cm

0.4 cm/sec

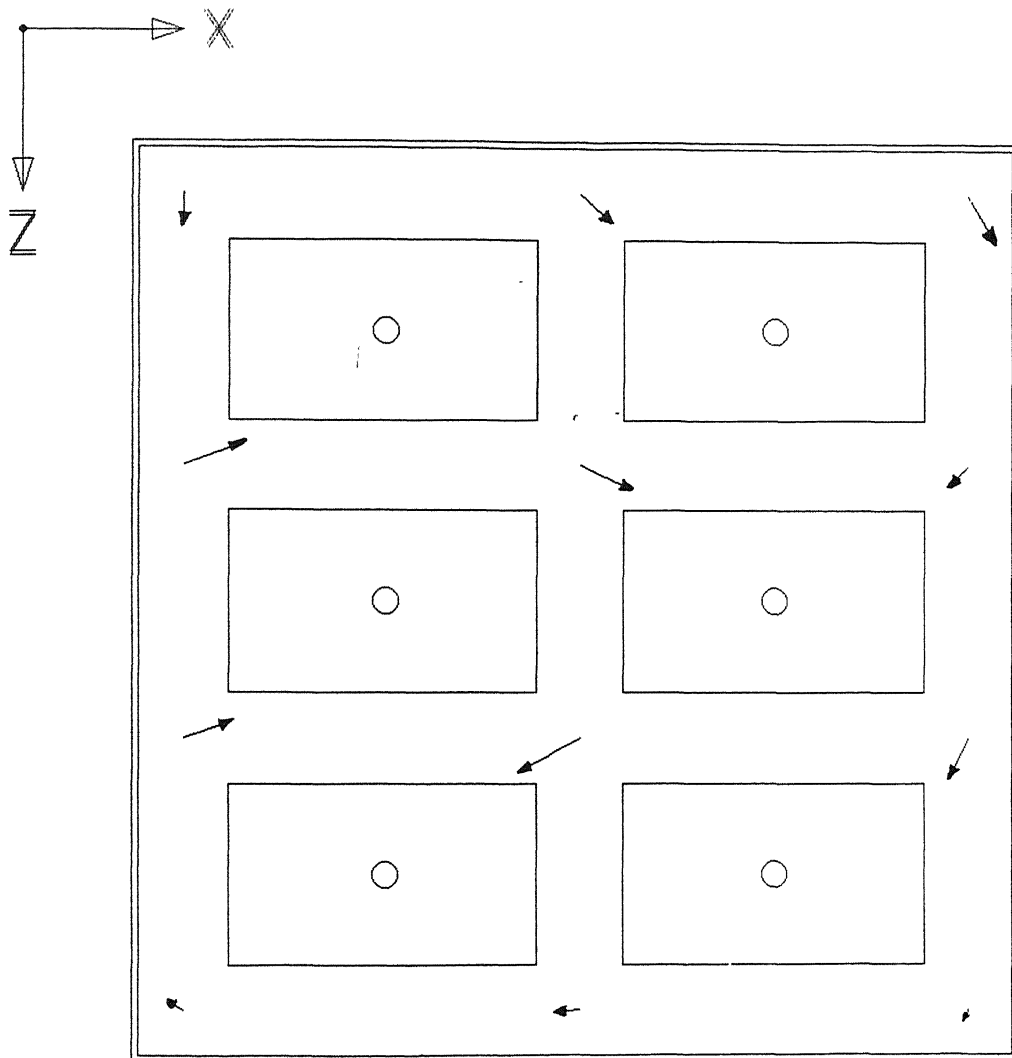


Fig. 4.7 (a) Measured velocity field for current density  $0.75 \text{ A/cm}^2$ .

Current input = 288 A

Current Density =  $0.5 \text{ A/cm}^2$

ACD = 2.5 cm

Depth of measurement = 3.4 cm

0.4 cm/sec

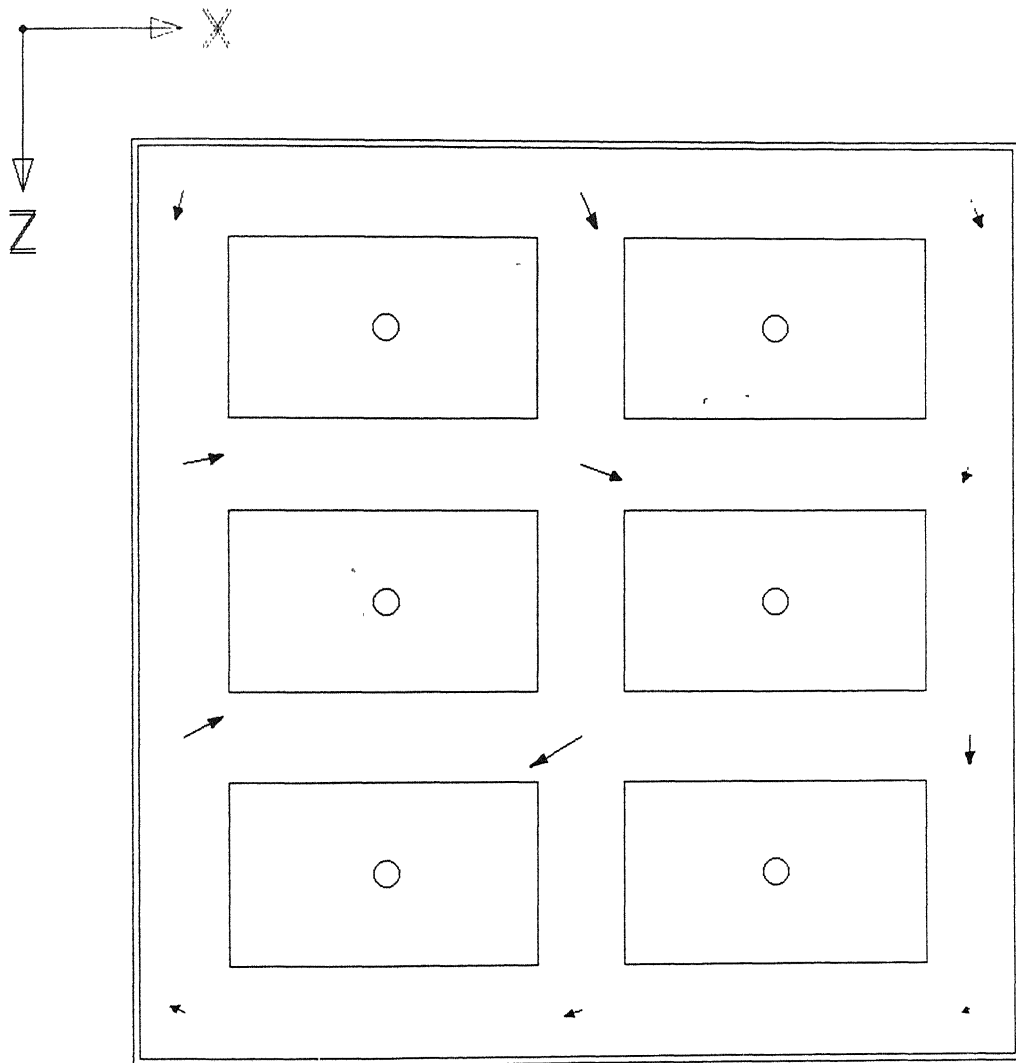


Fig. 4.7 (b) Measured velocity fields for current density  $0.50 \text{ A/cm}^2$ .

Measurements were done at all the locations by varying the current density to have an idea about the flow pattern. Velocity measurements were done for three different current densities i. e. 1.0, 0.75, 0.50 A/cm<sup>2</sup> keeping the other parameters like ACD, depth of the measurement same as that of the base case. Figure 4.2, 4.7 (a), and (b) shows the velocity pattern at current density of 1 A/cm<sup>2</sup>, 0.75 A/cm<sup>2</sup> and 0.50 A/cm<sup>2</sup> respectively. As expected melt velocity increases with current density. The velocity pattern was found to be nearly same, but the magnitude of the velocity is higher at all the points in the case of current density of 1.0 A/cm<sup>2</sup> (base case) as compared to that at lower current densities as described.

#### **4.1.3 EFFECT OF ANODE CATHODE DISTANCE**

The anode cathode distance has a great role in deciding the flow field of the cell. The anodes used in industrial cell are made of carbon, which gets consumed during the reaction. Hence, during the process the bottom surface of anode keeps varying and it changes the anode to cathode distance. So to simulate the effect of changing ACD on velocity field of the melt the cell, it was varied from base case of 2.5 cm to 2.0 cm and 1.5 cm. Comparison of Fig.4.2 and Fig 4.8 (a) and (b) shows that there is a significant decrease of magnitude of velocity when ACD is reduced from 2.5 to 2.0 cm. However there is no such significant change in velocity from ACD 2.0 cm to 1.5 cm. This is consistent with the fact that the effective volume of melt decreases with decreasing ACD. The electromagnetic force per unit volume of the Wood's metal increases with decreasing ACD, for a constant current input. Consequently, it is expected that melt velocity would increase. But lower ACD and higher melt velocity would translate into higher drag force. Hence the velocity is found to have decreased as the ACD is decreased.

#### **4.1.4 EFFECT OF LEDGE**

In real life cells, there is alumina lining next to the steel super cell. Hence there is very less current flow through the side wall. To simulate this condition in our cell an insulating strip hereby called ledge was placed. Previous investigation in the simulated cell shows that a significant amount of current passes through the cell wall [7]. So to study

Current input = 576 A

Current Density =  $1.0 \text{ A/cm}^2$

ACD = 2.0 cm

Depth of measurement = 3.4 cm

0.4 cm/sec

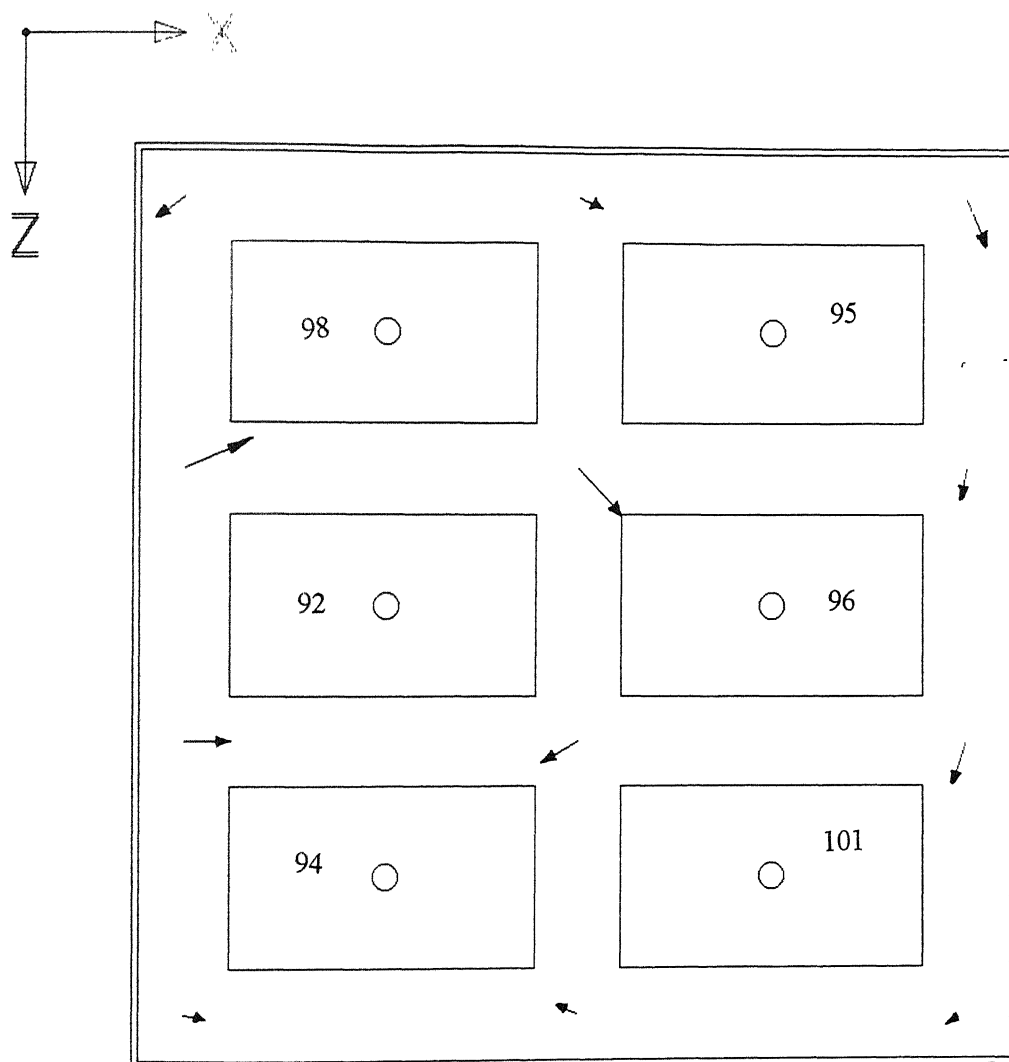


Fig. 4.8 (a) Measured velocity distribution with anode cathode distance of 2.0 cm.



Current input = 576 A

Current Density =  $1.0 \text{ A/cm}^2$

ACD = 1.5 cm

Depth of measurement = 3.4 cm

0.4 cm/sec

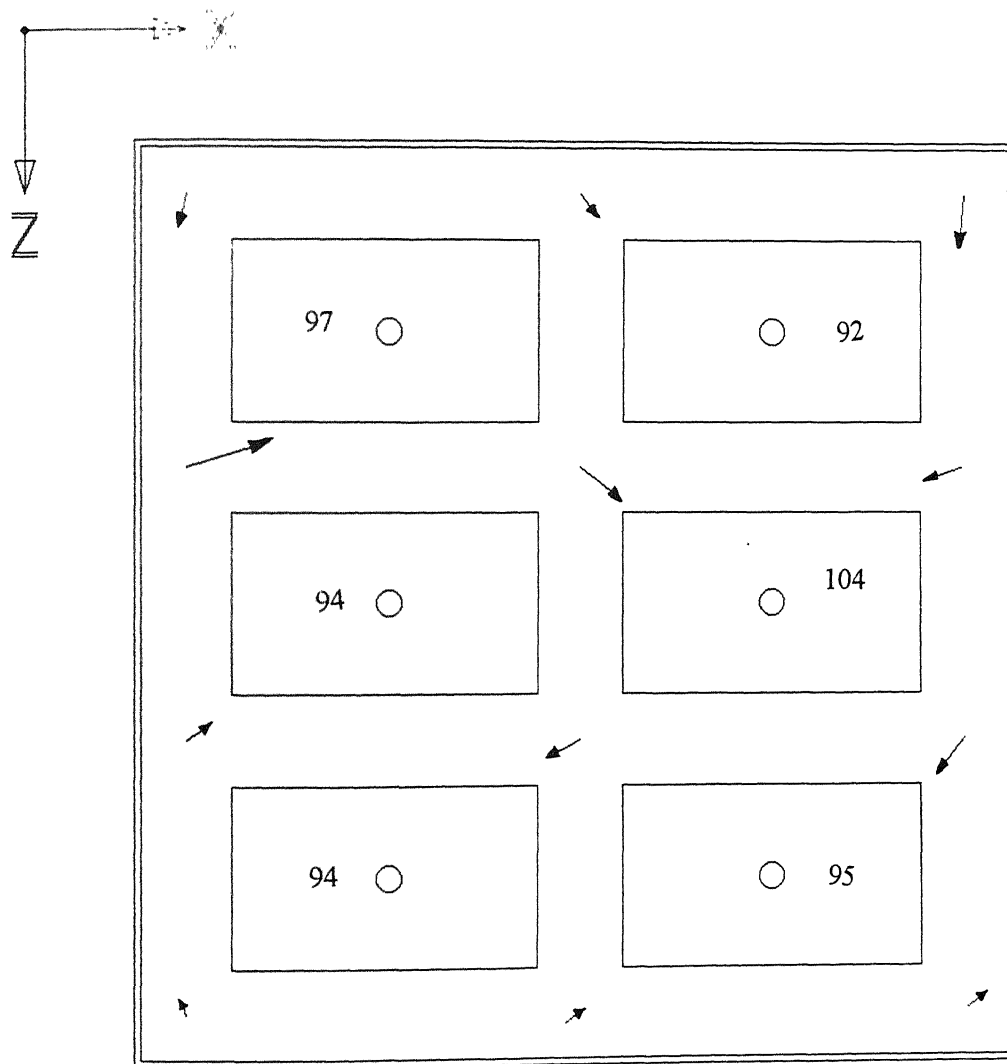


Fig. 4.8 (b) Measured velocity fields with anode cathode distance of 1.5 cm.

Current input = 576 A

Current Density =  $1.0 \text{ A/cm}^2$

ACD = 2.5 cm

Depth of measurement = 3.4 cm

0.4 cm/sec

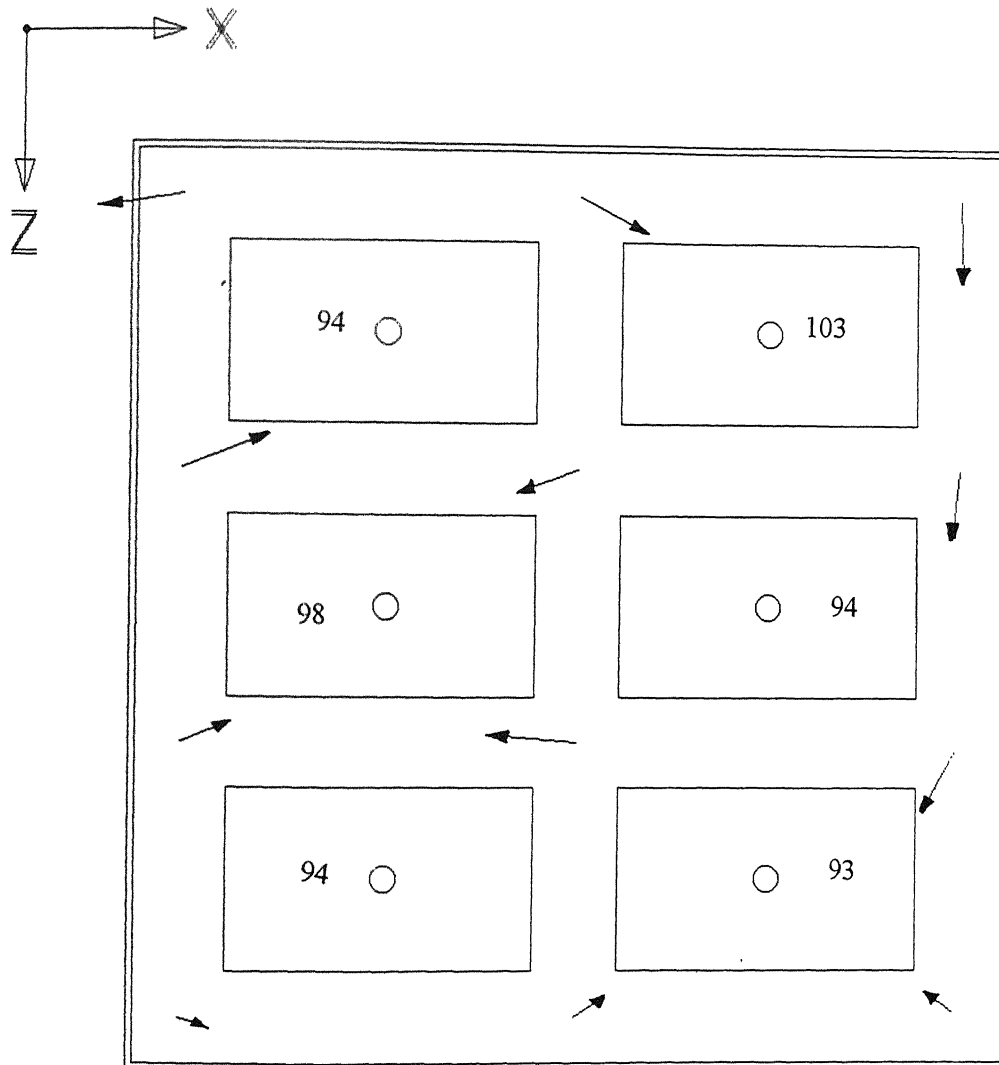


Fig. 4.9 Measured velocity field with non conducting strips at the sidewalls.

the effect of ledge on velocity profile nonconducting strips of constant thickness were put on the side walls of the cell to simulate a real life cell. Measurement of velocity was performed keeping the conditions constant as in the base case. Figure 4.9 shows the velocity field vectors and on comparison with the base case (Fig. 4.2) it is evident that the magnitude of the velocity has been increased and the direction of the melt flow has been altered at some of the points. The clockwise circulation of the melt found to exist along with the weakly anticlockwise circulation.

## **4.2 Sensitivity Experiments:**

During the course of velocity measurement the exact positioning of the probe in all the experiments was not the same although a great care has been taken to place it as precisely as possible. So to get an exact idea of the sensitivity of the probe positions near a given location, the probe was placed 3-6 mm on neighbouring points of the desired position. Figure 4.10 suggest that velocity indeed is sensitive to probe positions.

Current input = 576 A

Current Density =  $1.0 \text{ A/cm}^2$

ACD = 2.5 cm

Depth of measurement = 3.4 cm

0.4 cm/sec

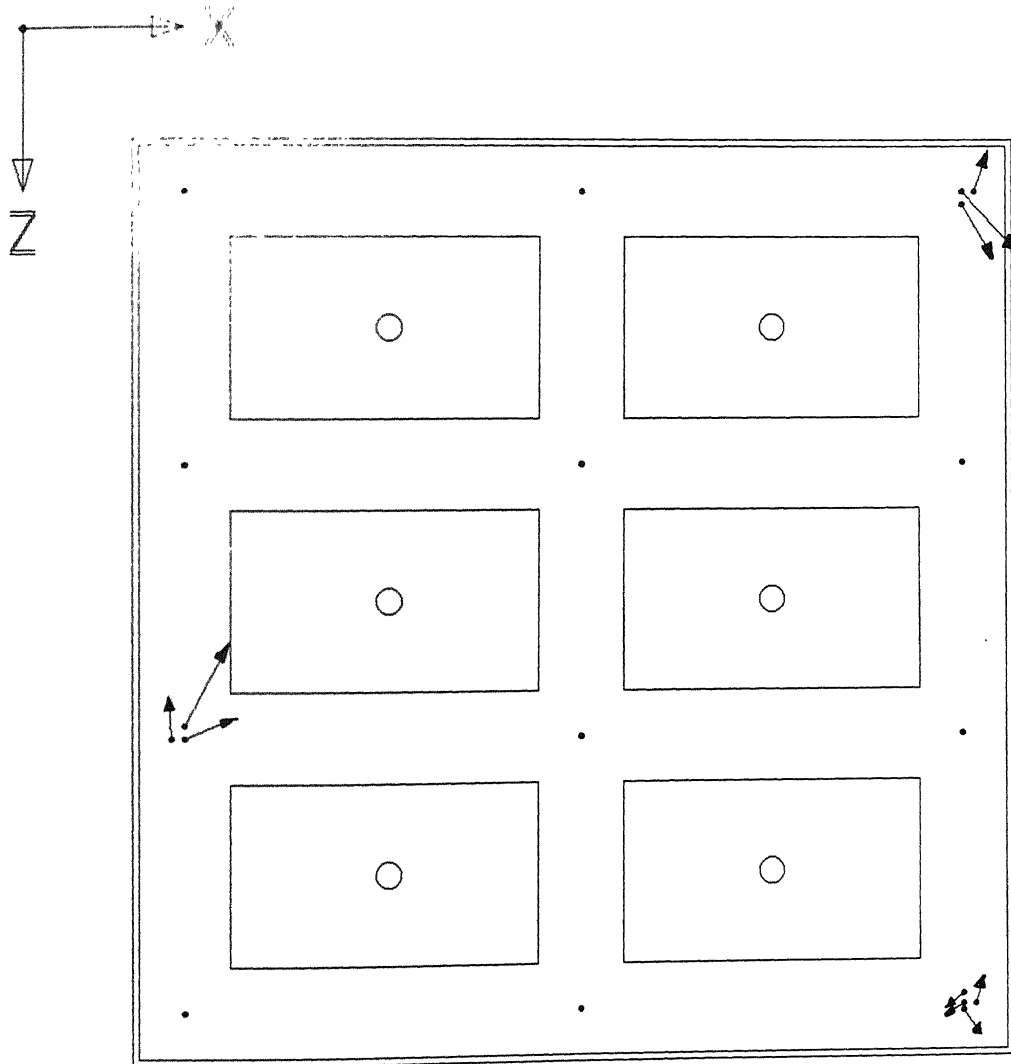


Fig. 4.10 Measured velocity fields near points '3', '4', and '12' as a test of sensitivity of measurements.

## Governing Equations:

The model is based on the Navier-Stokes equation of motion and the equation of continuity. The electromagnetic force is taken as a source term. The time-averaged, depth-averaged velocities are defined as

$$\bar{U} = \frac{1}{h} \int_{h_b}^{h_b+h} U dz, \text{ and } \bar{V} = \frac{1}{h} \int_{h_b}^{h_b+h} V dz$$

where  $h_b$  is the bottom bed level, and  $h$  is the height of the melt.

## Equation of Continuity:

Two dimensional continuity equation for an incompressible flow is

$$\frac{\partial \bar{U}}{\partial X} + \frac{\partial \bar{V}}{\partial Y} = 0 \quad \text{-----} \quad (5.1)$$

## Navier-Stokes' Equation:

Setting up conservation of momentum over the control volume results in

*X- momentum equation:*

$$\bar{U} \frac{\partial \bar{U}}{\partial X} + \bar{V} \frac{\partial \bar{U}}{\partial Y} = -\frac{1}{\rho} \frac{\partial P}{\partial X} + \left( \frac{\mu_{eff}}{\rho} \right) \left( \frac{\partial^2 \bar{U}}{\partial X^2} + \frac{\partial^2 \bar{U}}{\partial Y^2} \right) + (\vec{J} \times \vec{B})_x - \frac{\tau_{bx}}{\rho h} \quad \text{-----} \quad (5.2)$$

*Y- momentum equation:*

$$\bar{U} \frac{\partial \bar{V}}{\partial X} + \bar{V} \frac{\partial \bar{V}}{\partial Y} = -\frac{1}{\rho} \frac{\partial P}{\partial Y} + \left( \frac{\mu_{eff}}{\rho} \right) \left( \frac{\partial^2 \bar{V}}{\partial X^2} + \frac{\partial^2 \bar{V}}{\partial Y^2} \right) + (\vec{J} \times \vec{B})_y - \frac{\tau_{by}}{\rho h} \quad \text{-----} \quad (5.3)$$

Here  $(\vec{J} \times \vec{B})$  represent the electromagnetic force,

$\vec{J}$  is the current density and  $\vec{B}$  is the magnetic field. The details of the current density ( $\vec{J}$ ) distribution model and magnetic field ( $\vec{B}$ ) distribution model and the solution procedures are given in appendix.  $\mu_{eff}$  is the effective viscosity, which is the sum of the laminar and turbulent viscosities i. e.  $\mu_{eff} = \mu_l + \mu_t$

The turbulent contribution to the viscosity was calculated by using the  $k$ - $\varepsilon$  model for turbulence developed by Spalding, Launder and coworkers [18]. The turbulent viscosity is defined as

$$\mu_t = 0.09 \left( \frac{\rho k^2}{\varepsilon} \right) \text{ where } k \text{ is the kinetic energy of turbulence, } \varepsilon \text{ is the dissipation rate of}$$

kinetic energy of turbulence, and  $\rho$  is fluid density.

The values of  $k$  and  $\varepsilon$  are obtained from two additional transport equations as stated in the literature [10].  $\tau_{bx}$ , and  $\tau_{by}$  are the shear stresses in x and y directions respectively which takes care of the shear stress offered due to the bottom of the bed as well as the bottom surface of the anodes. These are derived by applying the quadratic friction law. These bed shear stresses are represented in terms of depth averaged velocity component as below.

$$\tau_{bx} = \frac{C_f \rho \bar{U}}{\cos \phi} (\bar{U}^2 + \bar{V}^2)^{0.5} ; \tau_{by} = \frac{C_f \rho \bar{V}}{\cos \phi} (\bar{U}^2 + \bar{V}^2)^{0.5}$$

It may be noted that  $\tau_{bx}$  and  $\tau_{by}$  are forces per projected horizontal area and  $C_f$  is friction coefficient which depends on the roughness of the bed. The No slip boundary conditions are imposed along the boundaries, i.e.  $\bar{U} = \bar{V} = 0$  at the walls. The momentum, heat and mass transfer software “PHOENICS” is used to solve equations (5.1), (5.2), and (5.3) with the boundary conditions.

THE ALGORITHM:

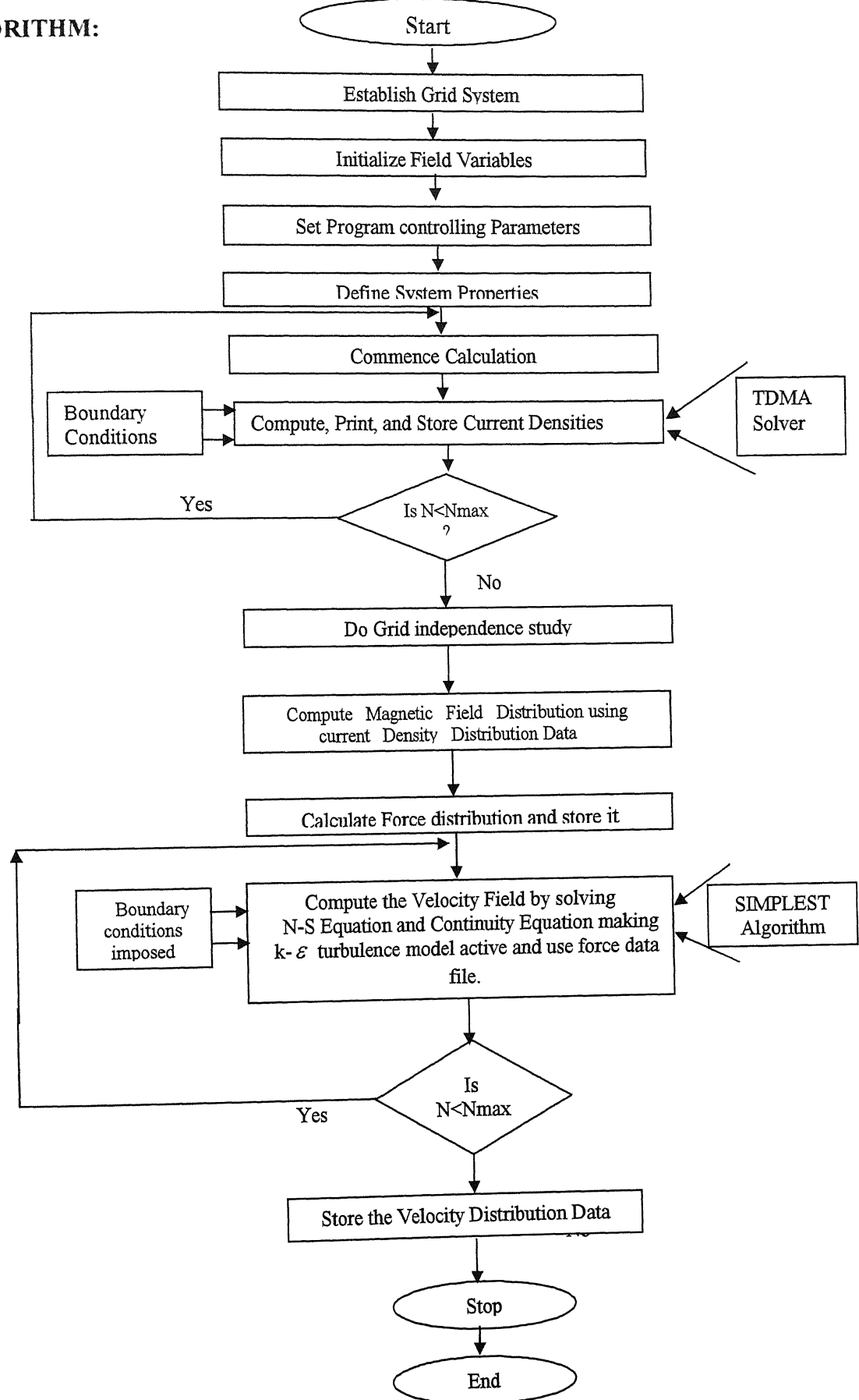


Fig. 5.2 The algorithm for computation of velocity field distribution.

Initially the current density distribution and the magnetic field distribution within the cell were solved by using the model equations along with the boundary conditions. Then the electromagnetic force  $\vec{F} = \vec{J} \times \vec{B}$  was calculated in the computed domain. This force is used as the source term for solving the depth averaged Navier-Stokes equation and the continuity equation along with the k- $\varepsilon$  turbulence model made active. The necessary no slip boundary conditions were imposed.

## **5.3 PREDICTION OF VELOCITY FIELD DISTRIBUTION AND COMPARISON WITH EXPERIMENTAL RESULTS**

The mathematical models along with the boundary conditions have been solved to predict the velocity profiles of the melt. After grid independence study  $120 \times 100$  grids was used for computation of velocity. For each variations of parameter the whole process of calculation starting from current density was repeated step by step. Finally the predicted results are then compared with the experimental results. The velocity field is predicted with equal distribution of the current through the anodes, anode busbars, and collector bars.

### **5.3.1 EFFECT OF TOTAL CURRENT INPUT**

The total current input was varied from 100 to 500 A with a step size of 100 A and the whole set of calculation was done to compute the velocity field. The comparison of the predicted velocity and the experimental result at the specified locations are shown in Fig. 5.3 (a), (b), and (c). The predicted velocities are in good agreement with the experimental results. Similar to the measured velocities at different values of current densities, the velocity field was predicted for current density value of 0.5, 0.75, and 1.0 A/cm<sup>2</sup> and are shown in Fig. 5.4 (a), (b), and (c). As expected the velocity increases with increasing current density. The velocity field distribution is similar for all the cases. Comparison of Figs. 5.4 (a) to 5.4 (c) with Fig 4.7(a), (b), and Fig. 4.2 shows that there is a reasonable agreement between the predicted and experimental results. There are few deviations in direction and are attributed to the mismatch of the location of the point at



which the measurements were made during the experiments and the points those were taken in the models. It has been observed that a slight change in direction also changes the direction of the velocity vectors. This was verified doing sensitivity test in experiments by doing several measurements at neighboring positions so also same thing has been done in case of model predictions (ref section 5.4). The magnetic predicted at these same points are shown in Fig. 5.5. The velocity pattern predicted is consistent with the nature of magnetic field predicted in Fig. 5.5.

### **5.3.2 EFFECT OF ANODE CATHODE DISTANCE**

The Anode to cathode distance was varied keeping the current density at  $1.0 \text{ A/cm}^2$ . Figure 5.4 (c), 5.6 (a), and (b) shows the effect of decreasing the anode to cathode distance of 2.5, 2.0 and 1.5 cm respectively. It is evident that as ACD was decreased the depth averaged velocity decreased. This is due to the same reasons that have been described in section 4.4. This predicted velocity distribution is also similar to the experimental results shown in Figs. 4.3, 4.9 (a) and (b). However, the magnitude and the directions are slightly different for the points close to walls. The reason behind it is that the fixing of the probe is not precisely at same location at which the predictions have been done.

### **5.3.3 EFFECT OF LEDGE**

Velocity distribution calculations are carried out for the simulated cell with an asbestos sheet placed next to cell walls to simulate the ledge in a Hall cell. The predicted velocity distribution is shown in Fig. 5.7 with ACD 2.5 cm and current density  $1.0 \text{ A/cm}^2$  same as that of the base case. On comparison of Fig. 5.7 with Fig. 5.4 (C), it is evident that velocity has increased in magnitude. It appears that the clockwise circulation of the melt has remained prominent with ledge on the side walls. Comparison of Fig. 5.7 with Fig. (4.9) does not show a good agreement in terms of direction, but the magnitude of the velocity is appearing to be showing the same trend with respect to the base cases of the measurements and predictions. The deviation is attributed to the mismatch of the predicted magnetic field (Fig. 5.5) and the measured magnetic field (Fig. 4.3). The sensitivity also may be responsible for such a deviation.

ACD = 2.5 cm

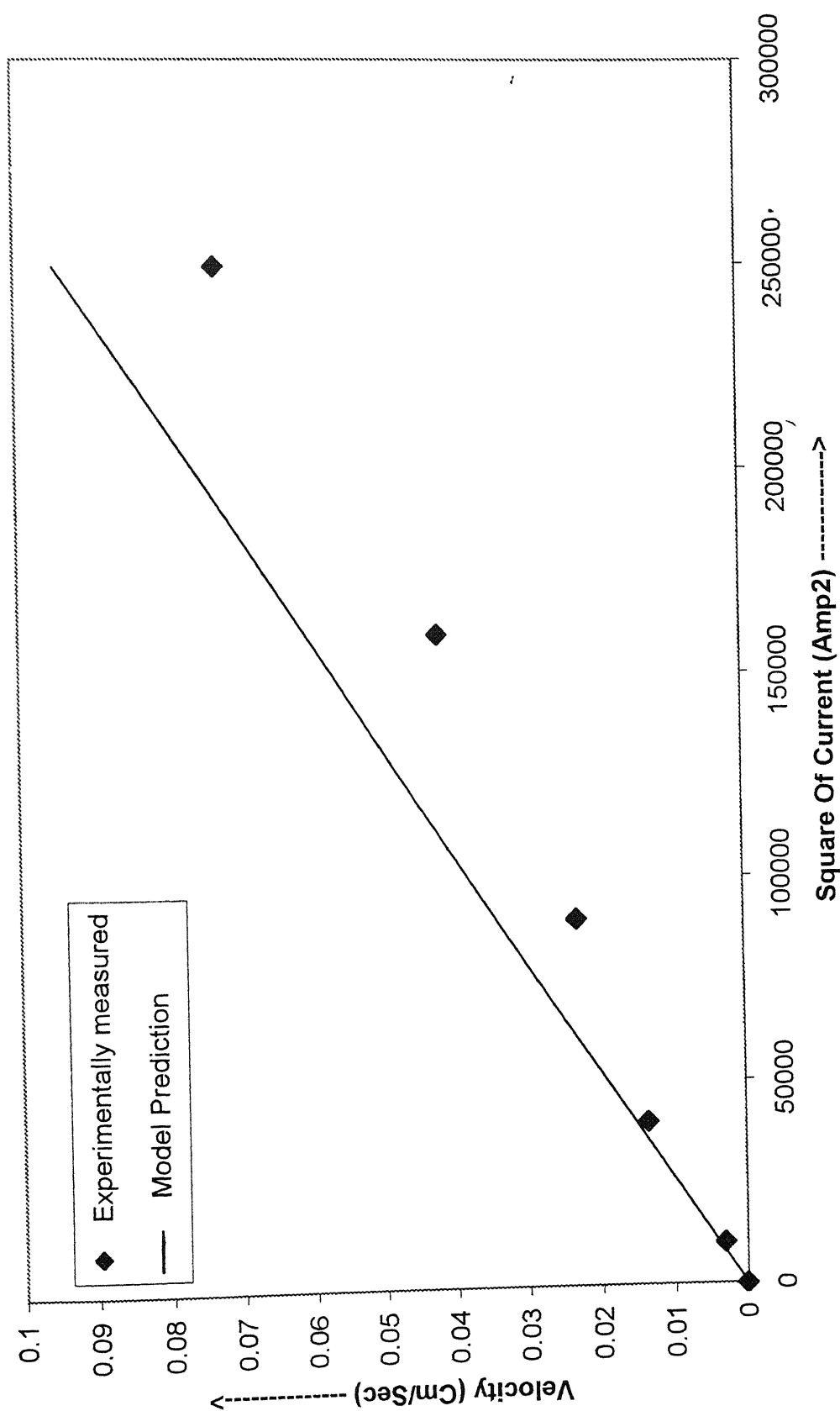


Fig. 5.3 (a) Comparison of predicted velocity and experimentally measured velocity at location 1

ACD = 2.5 cm

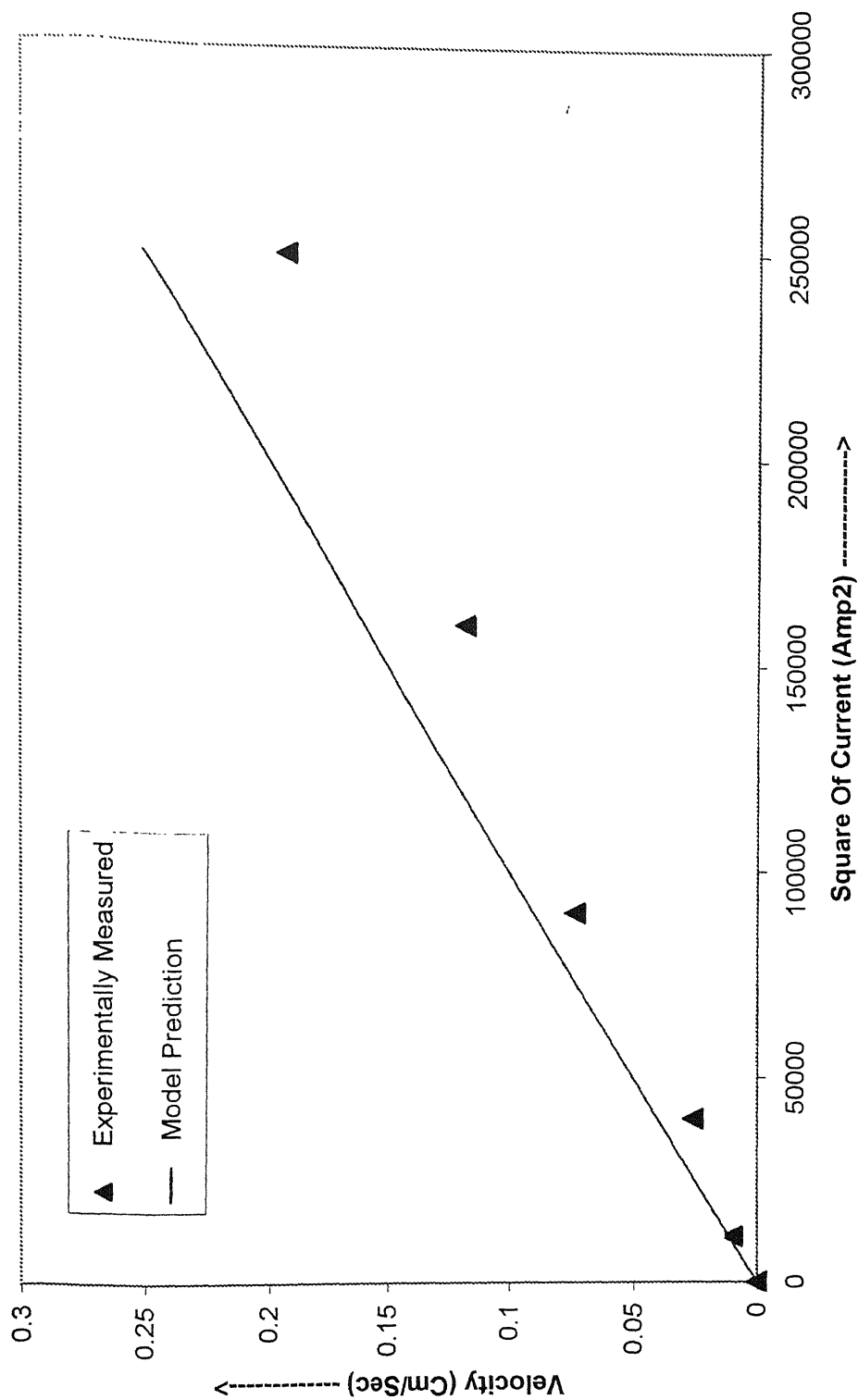


Fig. 5.3 (b) Comparison of predicted velocity and experimentally measured velocity at location 2

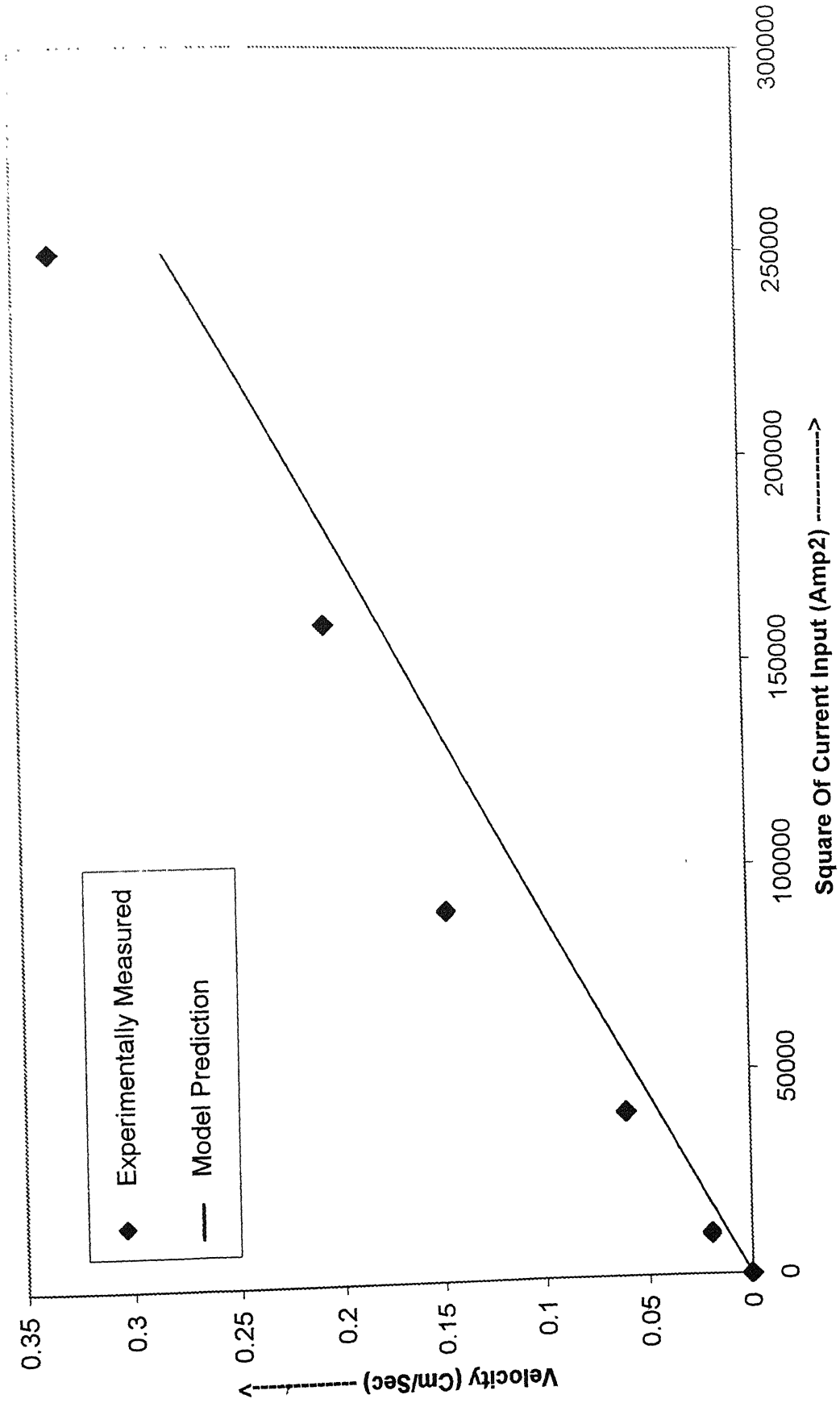


Fig 5 3 (c) Comparison of predicted velocity and experimentally measured velocity at Location 4

Current input = 288 A

Current Density =  $0.50 \text{ A/cm}^2$

ACD = 2.5 cm

0.4 cm/sec

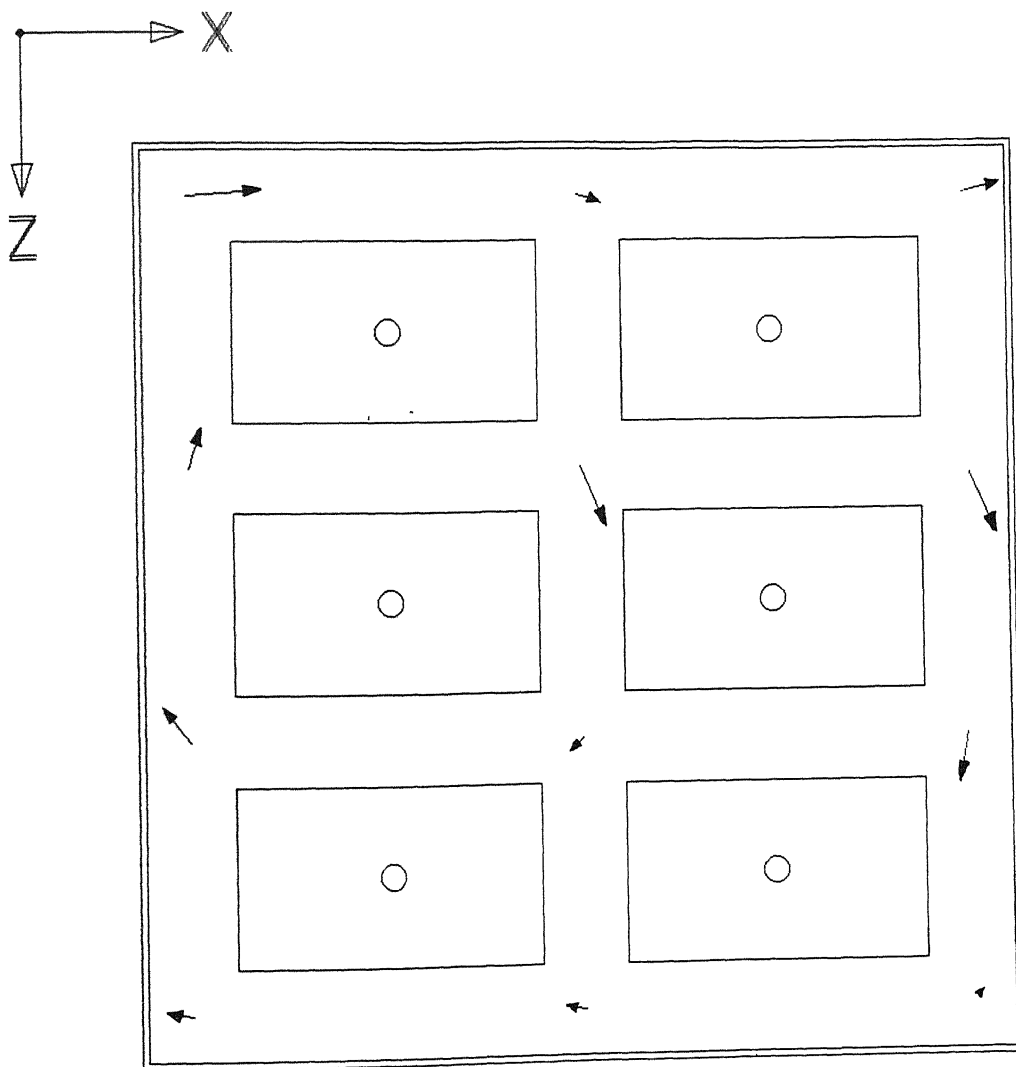
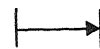


Fig. 5.4 (a) Predicted velocity distribution in the cell with current density  $0.5 \text{ A/cm}^2$ .

Current input = 432 A

Current Density =  $0.75 \text{ A/cm}^2$

ACD = 2.5 cm

0.4 cm/sec

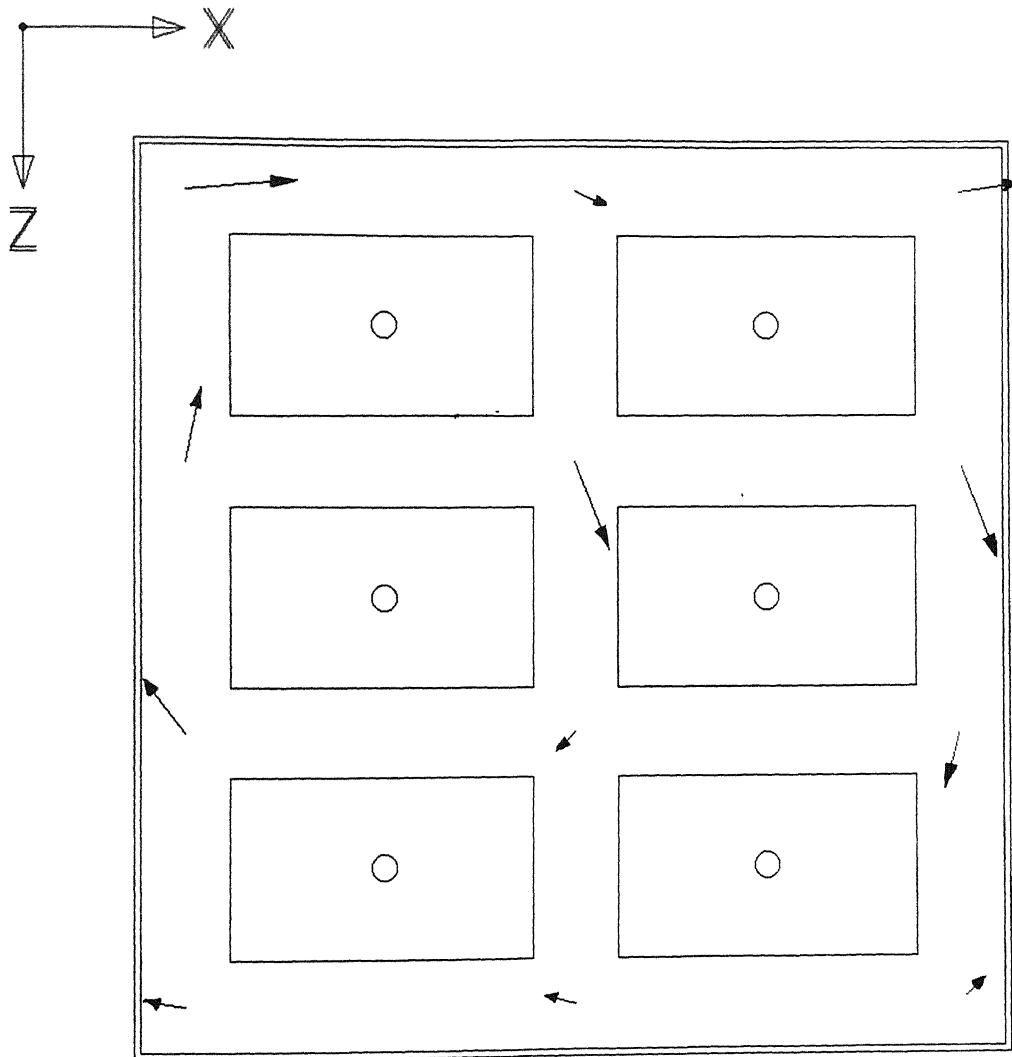
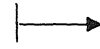


Fig. 5.4 (b) Predicted velocity distribution in the cell with current density  $0.75 \text{ A/cm}^2$ .

Current input = 576 A

Current Density =  $1.0 \text{ A/cm}^2$

ACD = 2.5 cm

0.4 cm/sec

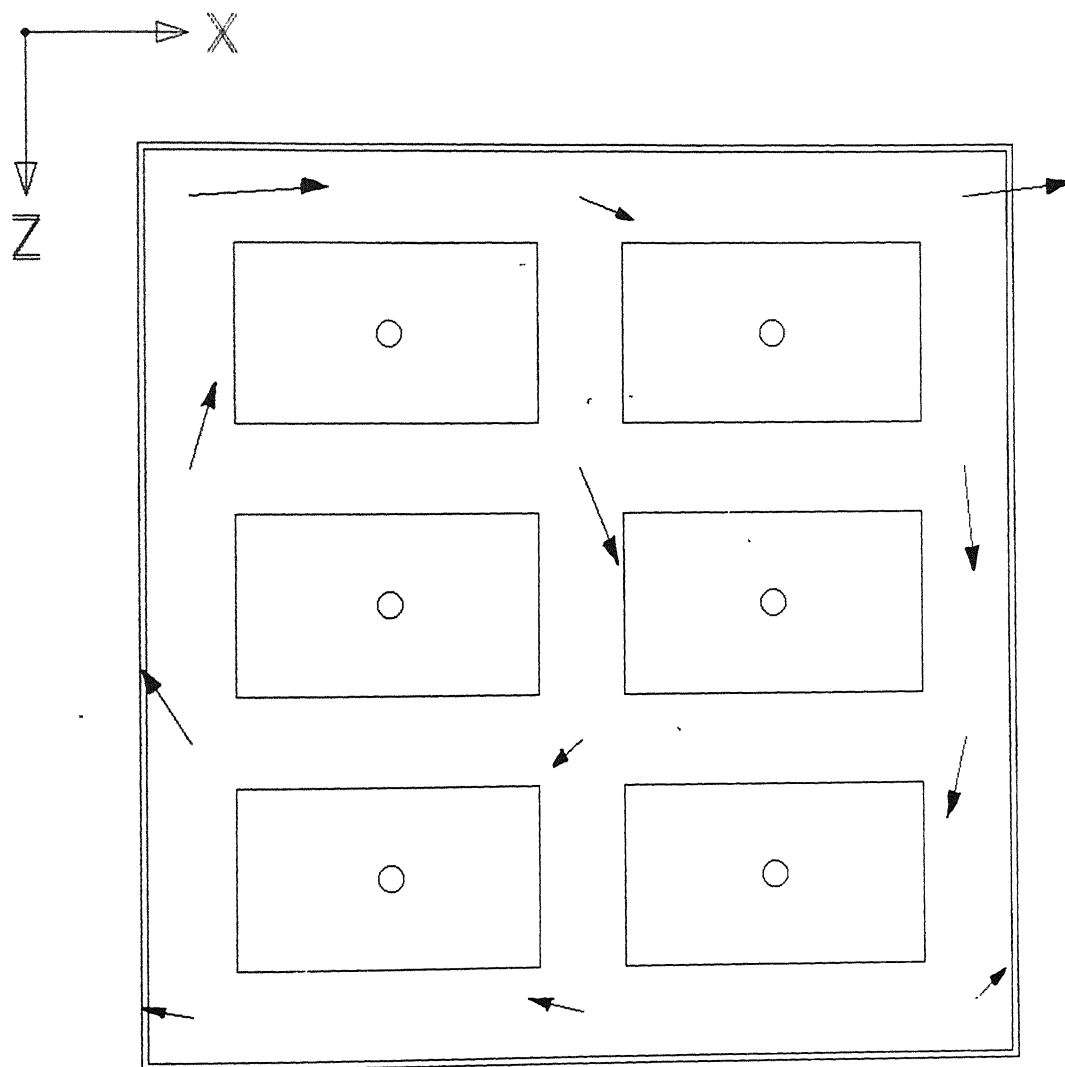


Fig. 5.4 (c) Predicted velocity distribution in the cell with current density  $1.0 \text{ A/cm}^2$ .

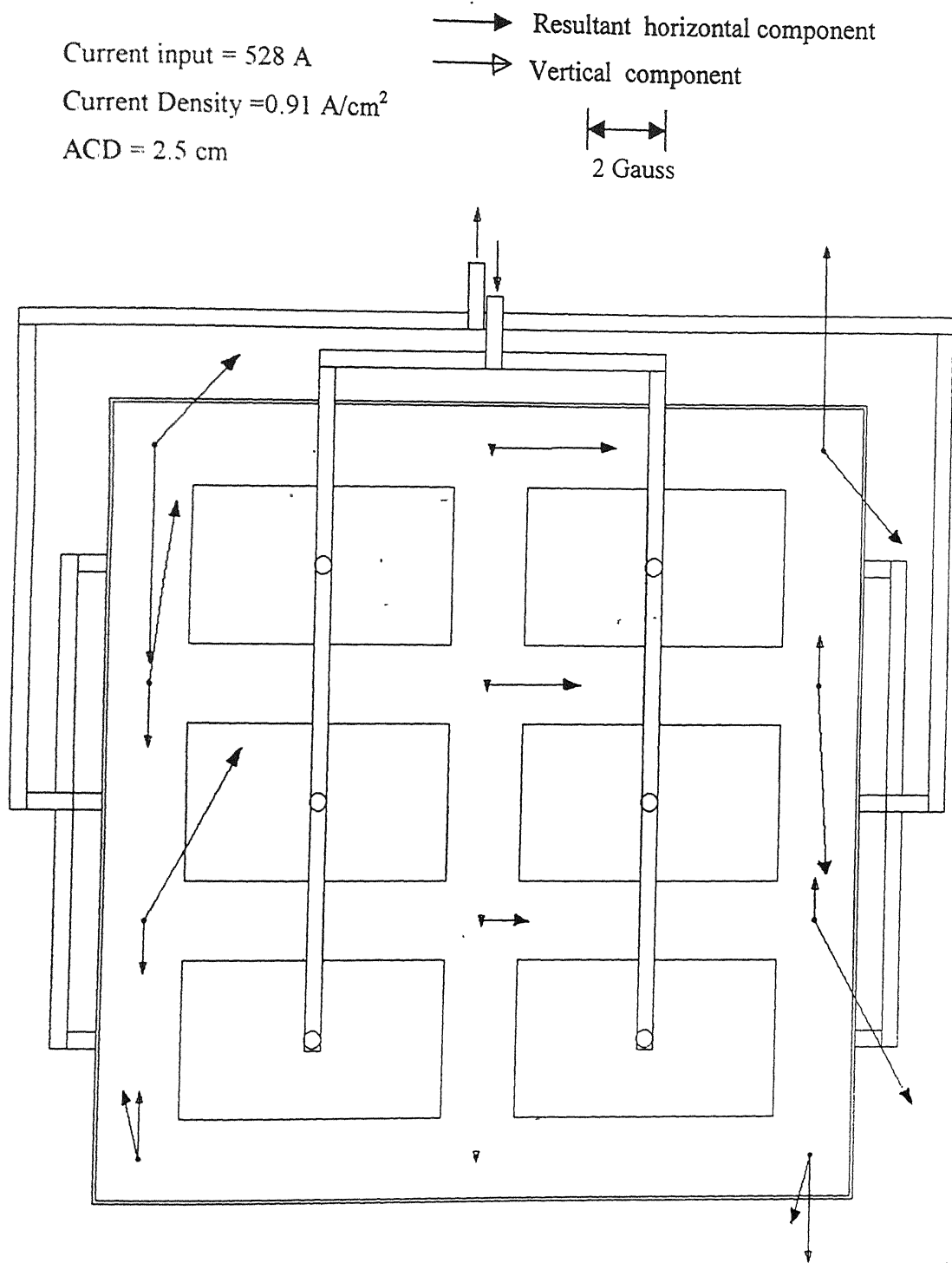


Fig. 5.5 Predicted magnetic field distribution when input current is 528 A [7].



Current input = 576 A

Current Density =  $1.0 \text{ A/cm}^2$

ACD = 2.0 cm

0.4 cm/sec

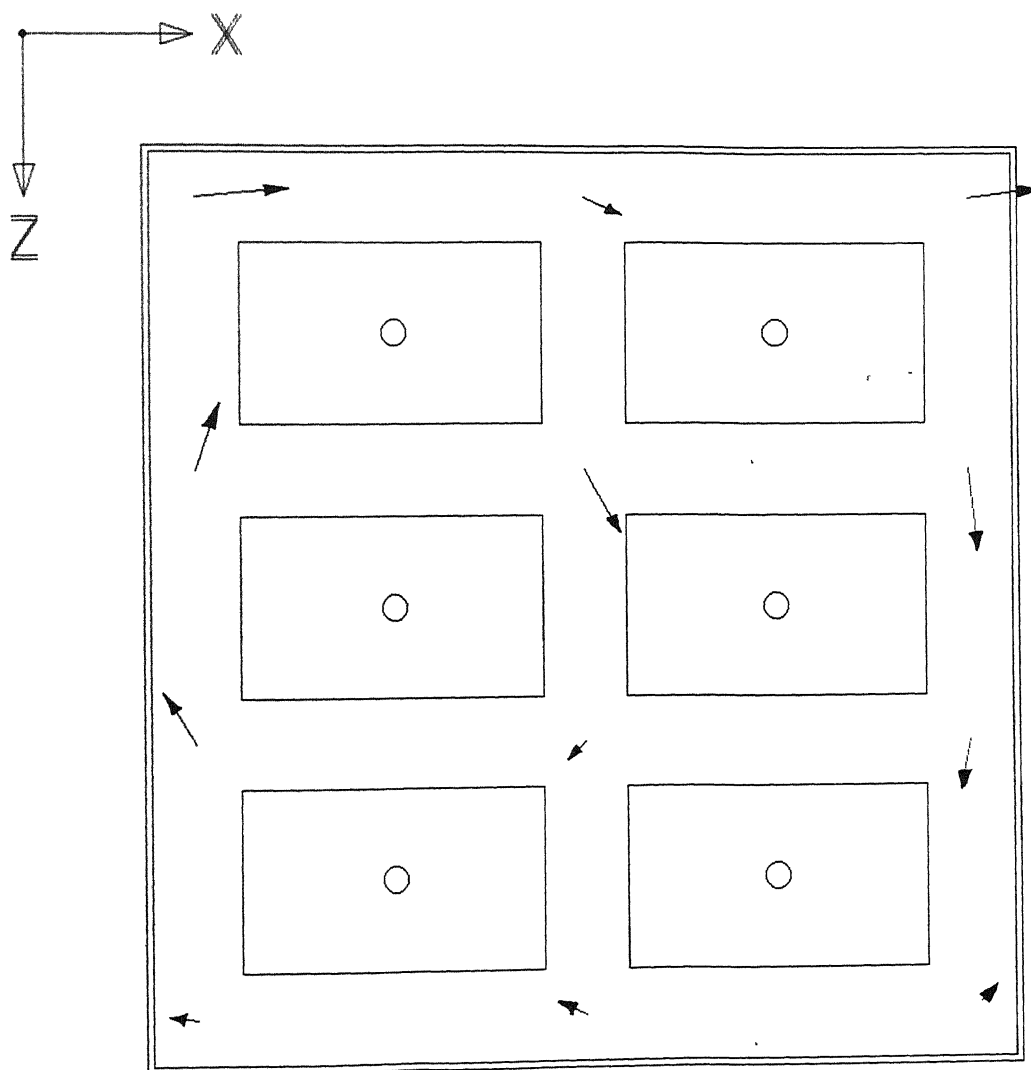
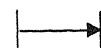


Fig. 5.6 (a) Predicted velocity distribution with ACD 2.0 cm.

Current input = 576 A

Current Density =  $1.0 \text{ A/cm}^2$

ACD = 1.5 cm

0.4 cm/sec

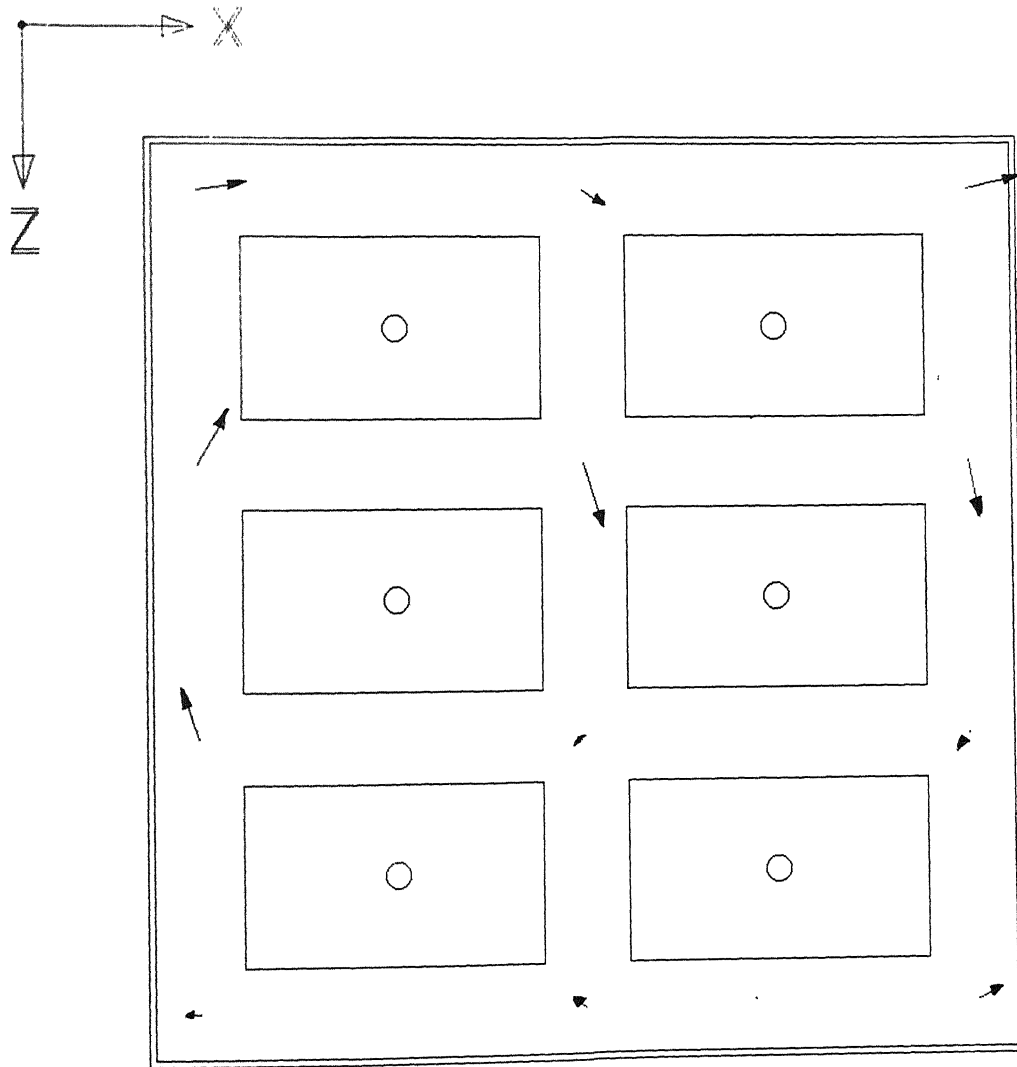


Fig. 5.6 (b) Predicted velocity field distributions with ACD 1.5 cm.

## 5.4 SENSITIVITY STUDY

The sensitivity of the model prediction is studied through measurements in the neighbouring points. It has been observed that the exact point where the model predicts is very crucial in adopting it during carrying out experiments. So some of the velocity shown in the prediction plots is not matching well with the direction of the velocity vector measured in the simulated cell. Figure 5.8 shows the sensitivity of predictions at some of the points. The velocity both varies in magnitude and direction by varying the position of the point where prediction is made.

Current input = 576 A

Current Density =  $1.0 \text{ A/cm}^2$

ACD = 2.5 cm

0.4 cm/sec

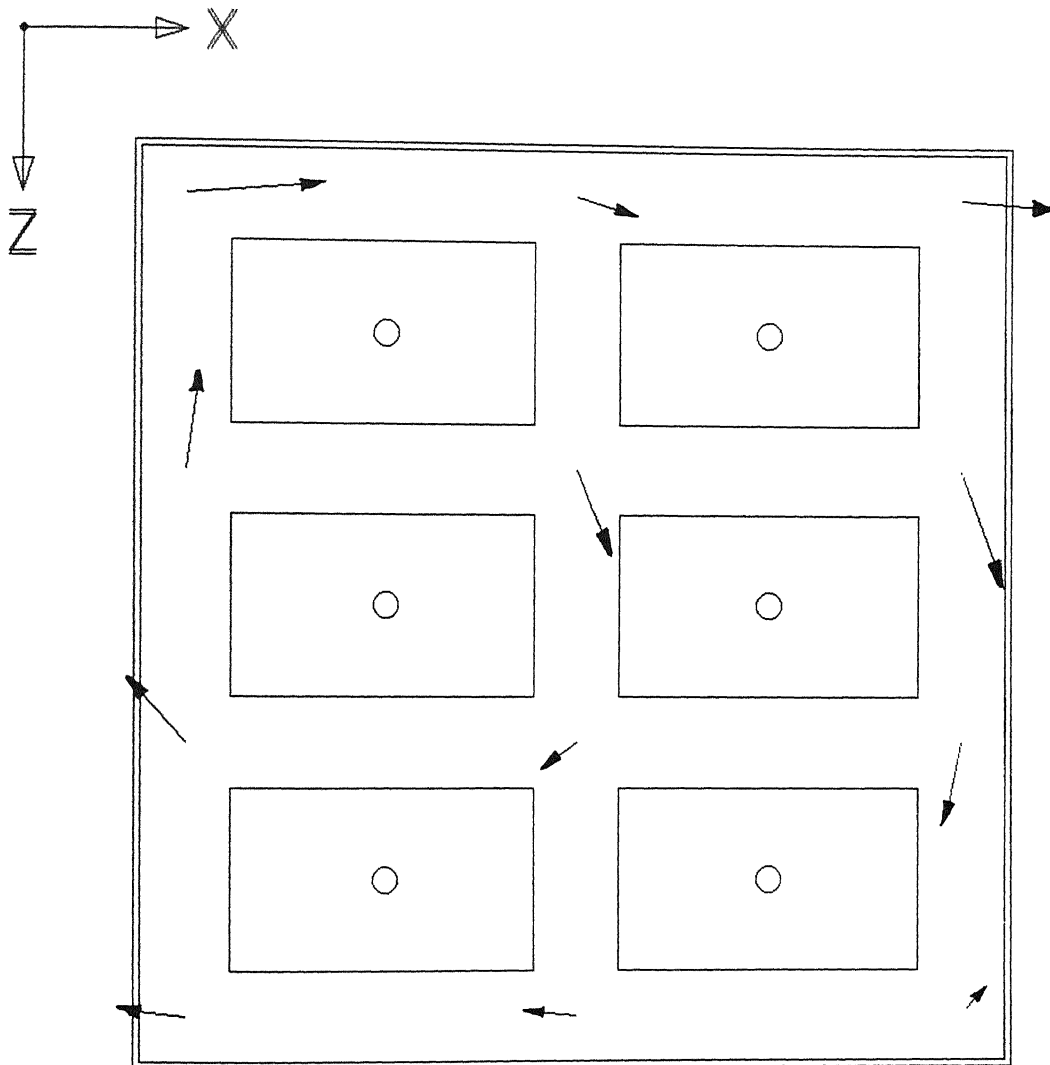


Fig. 5.7 Predicted velocity distribution with nonconducting strips put on the walls.

Current input = 576 A

Current Density =  $1.0 \text{ A/cm}^2$

ACD = 2.5 cm

0.4 cm/sec

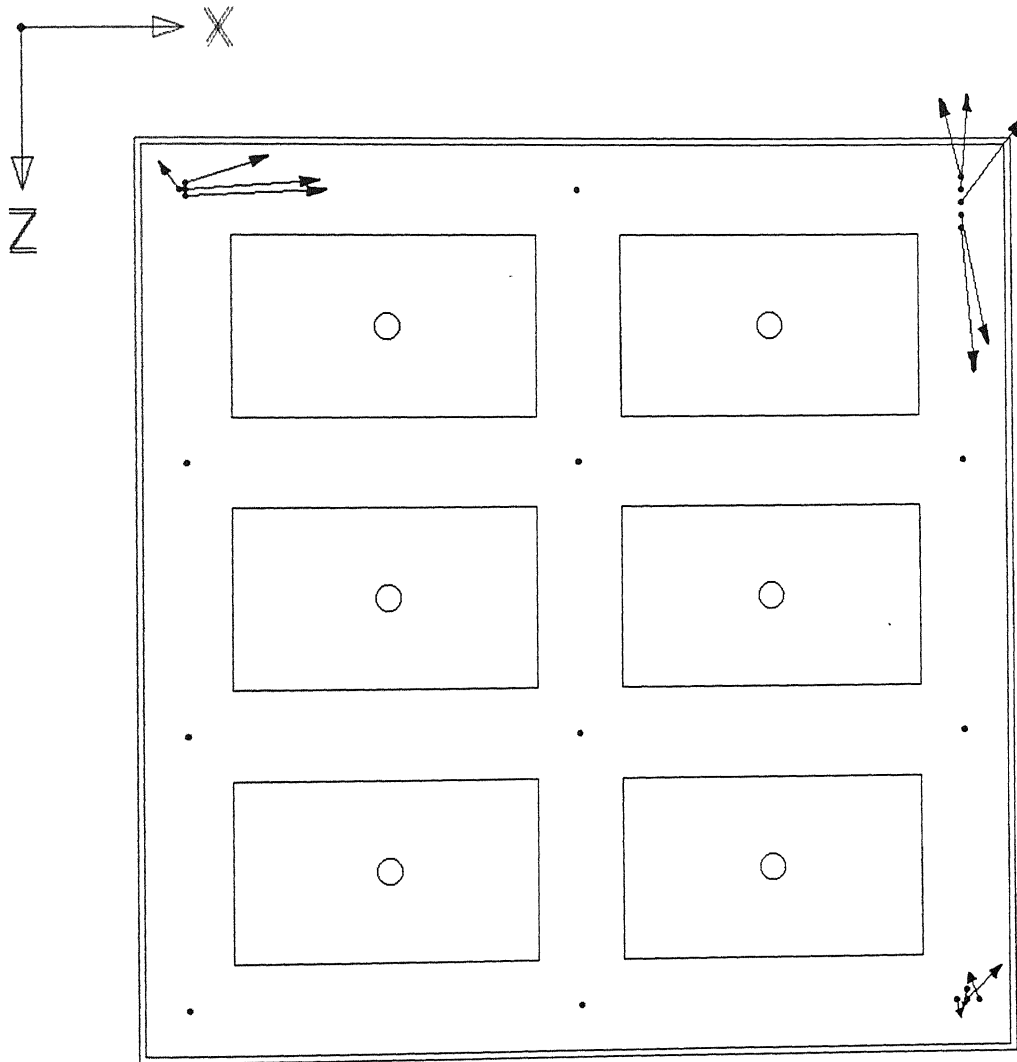


Fig. 5.8 Sensitivity test for model predictions at some points.

## **CHAPTER 6**

### **SUMMARY AND CONCLUDING REMARKS**

The present investigation is carried out with the objective of generating laboratory scale data of velocity field distribution within the simulated low temperature Hall cell for validating the mathematical models. The main aim of these models is to have a better understanding about the magnetohydrodynamics of the Hall cells, which basically controls oscillations at electrolyte metal interface. Due to this oscillating interface, it becomes difficult to operate the cell at optimum ACD. Sometime this results in short circuiting of the cell which leads to a higher energy and refractory consumption.

This investigation was planned to carry out in several stages. In the first stage a two layered (solid aluminium and Wood's metal) low temperature simulated cell was designed and fabricated. In the second stage a velocity measuring probe was designed and fabricated. In the third stage the strategy for calibrating velocity probe was established with a rack and pinion set up and then a rotating pot set up was designed and fabricated. In the fourth stage the calibration of the velocity probe was done and it was used to carry out the velocity measurements in the simulated cell. In the fifth stage the mathematical models for velocity distribution was formulated and solved. Finally the predicted velocity distributions have been compared with the experimental results.

The investigation can be concluded as:

- (i) A velocity probe is successfully designed, fabricated, calibrated, and reliably used for validating the model.
- (ii) The horizontal velocity in the melt at all points is directly proportional to the square of the current input to the cell.
- (iii) There is clockwise circulation of the melt with the end riser design of the busbars.
- (v) Decreasing anode to cathode distance decreases the velocity in magnitude.

- (vi) The motion of the melt is responsive to the variations of the electromagnetic force in the melt.
- (vii) Velocity distribution obtained from experiments on low temperature simulated cell is in good agreement with the model predictions.

## **CHAPTER 7**

### **RECOMMENDATION FOR FUTURE WORK**

The following features can be added in future:

- (i) Velocity measurements carried out in the simulated cell is limited to end riser design. So further measurements can be done on different designs like quarter riser design and novel riser design.
- (ii) Effect of anode dimensions, anode to wall distance, internodes distance, and the removal of anodes can be studied.
- (iii) Development of mathematical models which can predict the shape of the electrolyte-metal interface which is responsible for the magnetohydrodynamic instability in industrial Hall- Heroult cell.



## APPENDIX

Table A.1 The voltage distribution in an industrial Hall cell

Voltage components	Voltage (volts)	% of the total voltage
External conductors	0.16	3.4
Anode	0.32	6.9
Polarizations	0.60	12.9
Electrolyte bath	1.76	38.0
Chemical decomposition	1.20	25.9
Cathode	0.47	10.1
Others	0.13	2.8
Total	4.64	100.00

Table A.2 The physical property of Wood's metal.

1. Composition	Bi = 50.0 %,Pb = 26.7%, Sn = 13.3 % Cd = 10.0 %
2. Melting Point	72 <sup>0</sup> c
3. Density	10.7 gm/cm <sup>3</sup>
4. Viscosity	0.17 gm/cm-s
5. Temperature coefficient of resistance	0.002 (0 – 100 <sup>0</sup> C )
6. Electrical conductivity	9×10 <sup>3</sup> ohm <sup>-1</sup> cm <sup>-1</sup>

Table A.3 Physical properties of aluminium, cryolite and Wood's metal [19,20].

Properties	Units	Aluminium (at 900°C)	Cryolite (at 900°)	Wood's metal (at 100°C)
Density	gm cm <sup>-3</sup>	2.27	2.13	10.7
Viscosity	gm cm <sup>-1</sup> s <sup>-1</sup>	0.0118	0.0251	0.17
Magnetic permeability	Henry m <sup>-1</sup>	1.256×10 <sup>-8</sup>	1.257×10 <sup>-8</sup>	1.26×10 <sup>-8</sup>
Electrical conductivity	Ohm <sup>-1</sup> cm <sup>-1</sup>	3.45×10 <sup>4</sup>	2.22	9.0×10 <sup>3</sup>

Table A.4 Ratios of electrical conductivities [12].

Model	Ratio
Wood's metal/stainless steel.	0.37
Stainless steel/copper collector bar.	0.044
Real cell	
Electrolyte/carbon lining.	0.014
Carbon lining/steel collector bar.	0.056

Table A.5 Scale factor for different lengths of the simulated cell.

Parameters	Industrial Hall cell	Simulated Hall cell	Scale factor
Cell length (cm)	700-1000	62 (full cell)	11.29-16.13
Cell width (cm)	300 – 500	31	9.67 – 16.12
Cell height (cm)	100 – 150	10	10 – 15
Anode length (cm)	125	12	10.41
Anode width (cm)	70	8	8.75
Anode height (cm)	50	4	12.5
Total depth of Liquid (cm)	20 – 40	3 – 4	6.6 – 10.0

Table A.6 Comparison of the kinematic viscosity and the Magnetic Reynolds number for aluminium, cryolite and Woods metal zone [19, 20].

Parameters	Units	Aluminium	Cryolite	Wood's metal
Kinematic viscosity( $\nu$ )	$\text{cm}^2/\text{s}$	$5.2 \times 10^{-3}$	$11.8 \times 10^{-7}$	$15.9 \times 10^{-3}$
Magnetic Reynolds no. $N_{Re,m} = \frac{U_0 L_0 \sigma}{\mu}$	----	$4.2 \times 10^{11}$	$2.6 \times 10^7$	$8.5 \times 10^8$

## 1. MATHEMATICAL MODEL FOR CURRENT DISTRIBUTION

### Governing Equation:

The 3-D potential ( $\phi$ ) and current distribution ( $J$ ) within cell calculated by solving the following equations.

$$\frac{\partial}{\partial x} \left( \sigma \frac{\partial \phi}{\partial x} \right) + \frac{\partial}{\partial y} \left( \sigma \frac{\partial \phi}{\partial y} \right) + \frac{\partial}{\partial z} \left( \sigma \frac{\partial \phi}{\partial z} \right) = 0 \quad \text{----- (A.1)}$$

$$J = -\sigma \nabla \phi \quad \text{----- (A.2)}$$

### Boundary Conditions:

(i)  $x = 0, 0 \leq y \leq 10\text{cm}, 0 \leq z \leq 15.75\text{cm}$

$\phi = 0$  for collector bars Q and R shown in Fig. A 1.

$\frac{\partial \phi}{\partial x} = 0$  at cell wall.

(ii)  $0 \leq x \leq 15.5\text{cm}, 0 \leq y \leq 10\text{cm}, z = 0$

$\frac{\partial \phi}{\partial z} = 0$

(iii) Axis of symmetry N'O ( $x = 15.5\text{cm}, 0 \leq y \leq 10\text{cm}, 0 \leq z \leq 15.75\text{cm}$ )

$\frac{\partial \phi}{\partial x} = 0$



(iv) Axis of symmetry MO ( $0 \leq x \leq 15.5\text{cm}$ ,  $0 \leq y \leq 10\text{cm}$ ,  $z = 15.75\text{cm}$ )

$$\frac{\partial \phi}{\partial z} = 0$$

(v) at top surface ( $0 \leq x \leq 15.5\text{cm}$ ,  $y = 10\text{cm}$ ,  $0 \leq z \leq 15.75\text{cm}$ )

$$-\sigma \frac{\partial \phi}{\partial y} = J_{IN} \quad \text{for the area C and E, shown in Fig A.1}$$

$$\frac{\partial \phi}{\partial y} = 0 \quad \text{for the area other than C and E, shown in Fig A.1}$$

(vi) at cell bottom ( $0 \leq x \leq 15.5\text{cm}$ ,  $y = 0$ ,  $0 \leq z \leq 15.75\text{cm}$ )

$$\frac{\partial \phi}{\partial y} = 0$$

## 2. MATHEMATICAL MODEL FOR MAGNETIC FIELD DISTRIBUTION

### 5.3.1 Governing Equations:

Magnetic field produced by cell current:

The X, Y and Z components of magnetic field strength ( $B_{sx}$ ,  $B_{sy}$  and  $B_{sz}$ ) at any point produced by cell current can be determined by application of the Biot-Savart law.

The components of magnetic field at any point  $P(x_0, y_0, z_0)$  can be given in integral form as:

X component:

$$B_{sx} = \frac{\mu}{4\pi} \iiint \frac{I_y(z_0 - z) - I_z(y_0 - y)}{|(x_0 - x)^2 + (y_0 - y)^2 + (z_0 - z)^2|^{3/2}} dx dy dz \quad \text{----- (A.3)}$$

Y component:

$$B_{sy} = \frac{\mu}{4\pi} \iiint \frac{I_z(x_0 - x) - I_x(z_0 - z)}{|(x_0 - x)^2 + (y_0 - y)^2 + (z_0 - z)^2|^{3/2}} dx dy dz \quad \text{----- (A.4)}$$

Z component:

$$B_{sz} = \frac{\mu}{4\pi} \iiint \frac{I_x(y_0 - y) - I_y(x_0 - x)}{\left| (x_0 - x)^2 + (y_0 - y)^2 + (z_0 - z)^2 \right|^{3/2}} dx dy dz \quad \text{----- (A.5)}$$

where  $P(x_0, y_0, z_0)$  is the point where magnetic field strength is to be determined. This magnetic field is produced by an infinitesimal volume (sides  $dx$ ,  $dy$  and  $dz$ ) located at point  $Q(x, y, z)$  where current density components are  $I_x$ ,  $I_y$  and  $I_z$ . So integration over the whole volume gives the components of magnetic field ( $B_{sx}$ ,  $B_{sy}$ ,  $B_{sz}$ ) at point  $P(x_0, y_0, z_0)$ , produced by cell current.

### Magnetic field produced by external conductors (anode rods, bus bars and collector bar)

The magnetic field strength at any point produced by external current (current flowing through bus bars, anode rods and collector bars) can be calculated by application by Biot-Savart law as described below:

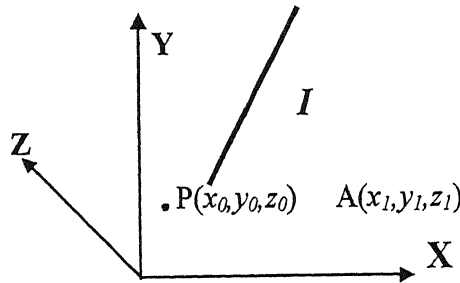


Fig. A.2 Schematic diagram showing axis and coordinate of conductor AB.

Let AB is a straight conductor carrying  $I$  amount of current as shown in Fig. A.2. The equation of line AB is given by:

$$\frac{x - x_1}{x_2 - x_1} = \frac{y - y_1}{y_2 - y_1} = \frac{z - z_1}{z_2 - z_1} \quad \text{----- (A.6)}$$

So the components of magnetic field ( $H_{px}$ ,  $H_{py}$ ,  $H_{pz}$ ) produced by the wire AB at point  $P(x_0, y_0, z_0)$  is given by:

**X component:**

$$B_{px} = \frac{\mu I}{4\pi} \left[ \int_{y_1}^{y_2} \frac{(z_0 - z)}{|(x_0 - x)^2 + (y_0 - y)^2 + (z_0 - z)^2|^{\frac{3}{2}}} dy - \int_{z_1}^{z_2} \frac{(y_0 - y)}{|(x_0 - x)^2 + (y_0 - y)^2 + (z_0 - z)^2|^{\frac{3}{2}}} dz \right] \quad \text{----- (A.7)}$$

**Y component:**

$$B_{py} = \frac{\mu I}{4\pi} \left[ \int_{z_1}^{z_2} \frac{(x_0 - x)}{|(x_0 - x)^2 + (y_0 - y)^2 + (z_0 - z)^2|^{\frac{3}{2}}} dz - \int_{x_1}^{x_2} \frac{(z_0 - z)}{|(x_0 - x)^2 + (y_0 - y)^2 + (z_0 - z)^2|^{\frac{3}{2}}} dx \right] \quad \text{----- (A.8)}$$

**Z component:**

$$B_{pz} = \frac{\mu I}{4\pi} \left[ \int_{x_1}^{x_2} \frac{(y_0 - y)}{|(x_0 - x)^2 + (y_0 - y)^2 + (z_0 - z)^2|^{\frac{3}{2}}} dx - \int_{y_1}^{y_2} \frac{(x_0 - x)}{|(x_0 - x)^2 + (y_0 - y)^2 + (z_0 - z)^2|^{\frac{3}{2}}} dy \right] \quad \text{----- (A.9)}$$

in equations (5.a), (5.b) and (5.c)  $x$ ,  $y$  and  $z$  can be evaluated by using equation (4). The same equation will be used for bus bars, anode rods and collector bars. The resultant components ( $B_x$ ,  $B_y$ ,  $B_z$ ) of magnetic field strength are given by the following equations:

**X component:**

$$B_x = B_{sx} + A_F \left[ \sum_{\text{anode rods}} B_{px} + \sum_{\text{collector bars}} B_{px} + \sum_{\text{bus bars}} B_{px} \right] \quad \text{----- (A.10)}$$

**Y component:**

$$B_y = B_{sy} + A_F \left[ \sum_{\text{anode rods}} B_{py} + \sum_{\text{collector bars}} B_{py} + \sum_{\text{bus bars}} B_{py} \right] \quad \text{----- (A.11)}$$

Z component:

$$B_z = B_{sz} + A_F \left[ \sum_{\text{anode rods}} B_{pz} + \sum_{\text{collector bars}} B_{pz} + \sum_{\text{bus bars}} B_{pz} \right] \text{------(A.12)}$$

where  $A_F$  is the magnetic attenuation factor.

The governing equations along with the boundary conditions were solved by using Heat and Mass transfer software 'PHOENICS'.



## REFERENCES

1. Donald P. Ziegler and Robert L. Kozarek, "Magnetic field measurements and comparison with calculations", *Light Metals* 1991, pp. 381-391.
2. A. J. Calandra, C. M. Ferro and C.E. Castelloano, "Electrochemical Acta", Vol 25, 1980, pp. 201.
3. Tom R. Alcorn, C. J. McMinn and A. T. Tabereaux, "Current Efficiency in aluminium electrolysis by anode gas analysis", *Light Metals*, 1975, pp. 683-694.
4. H. Kvande, J. J. J. Chen and W. E. Haupin, *Light Metals*, 1994, pp. 429.
5. M. Segatz and C. Droste, *Light Metals*, "Analysis of magnetohydrodynamic instabilities in Aluminium reduction cell", 1994, pp. 313-322.
6. H. C. Lee and J. W. Evans, "A physical model for electromagnetically driven flow in Hall cell." *light metals*, 1985, pp. 569-579.
7. D. Bhunia, M. Tech. Thesis, Deptt. of Materials and Metallurgical Engineering, IIT, Kanpur, 2001.
8. S. D. Lympnay and J. W. Evans, "The Hall- Heroult cell: Some Design Alternatives examined by a Mathematical Model", *Met. Trans. Vol. 14B*, Mar 1983, pp. 63-70.
9. M. Segatz and D. Vogelsang, "Effect of steel parts on the magnetic fields in Aluminium reduction cell", *Light Metals* 1991, pp. 393-398.
10. J. W. Evans, Y. Zundeleovich and D. Sharma, "A Mathematical model for prediction of currents, magnetic fields, melt velocities, melt topography and current efficiency in the Hall-Heroult cell", *Metallurgical Transactions*, vol 12B, June 1981, pp. 353-360.
11. Z. A. Siddiqui, M. Tech. Thesis, Dept. of Materials and Metallurgical Eng., IIT, Kanpur, 2000.
12. S. K. Banerjee and J. W. Evans, "Measurements of magnetic fields and electromagnetically driven melt in a physical model of a Hall-Heroult cell", *Metallurgical Transactions B*, vol. 21 B, Feb 1990, pp. 59-69.
13. Johnson A.R., *Light metals*, 1978.
14. A. Furmam, *Light Metals*, 1978, pp. 87.

15. R. Shekhar and J. W. Evans, "Physical modeling studies of electrolyte flow due to gas evolution and some aspects of bubble behaviour in advanced Hall cells: Part II. Flow and Interpolar resistance in cells with grooved anodes", *Met. Trans*, Vol. 25B, June 1994, pp. 341-349.
16. S. Fortien, M. Gerhadt and A. J. Gesing, *Light Metals*, 1984, pp. 323.
17. B.F Bradley, E. W. Dewing, J. N. Rogers, *Light Metals*, 1981, pp. 541.
18. B. E. Launder and D. B. Spalding, *Computer methods in applied mechanics and Engineering*, Vol. 3, 1974, pp. 269-89.
19. K. Ai Daniel, "The Hydrodynamics of the Hall- Heroult cell", *Light metals*, 1985, pp. 593-607.
20. W. E. Haupin, *Journal of Minerals, Metals, Materials*, July 1971.
21. J. Szekely, J. W. Evans, K. Blazek and N. El- Kaddah, "Magnetohydrodynamics in Process Metallurgy", *The Minerals, Metals and Materials Society*, 1991.

A 141905

